CHARACTERIZATION OF THE STRUCTURE AND REACTIVITY OF A NICKEL(II)-TRIPEPTIDE MIMIC OF NICKEL SUPEROXIDE DISMUTASE

BY

Amanda Michelle Glass

Submitted to the graduate degree program in Chemistry and the Graduate Faculty of the University of Kansas in partial fulfillment of the requirements for the degree of Doctor of Philosophy.

_____

Chairperson Timothy A. Jackson

_____

Mikhail V. Barybin

_____

David R. Benson

_____

Jennifer S. Laurence

_____

Emily E. Scott

Date Defended: June 7, 2012

The Dissertation Committee for Amanda Michelle Glass
Certifies that this is the approved version of the following dissertation:

CHARACTERIZATION OF THE STRUCTURE AND REACTIVITY OF A NICKEL(II)-
TRIPEPTIDE MIMIC OF NICKEL SUPEROXIDE DISMUTASE

_____
Chairperson Timothy A. Jackson

Date approved: June 12, 2012

Abstract

The tripeptide asparagine-cysteine-cysteine (NCC) was found by the J. Laurence lab to bind nickel very tightly. In fact, NCC was serendipitously discovered as a metal-abstraction peptide tag (MAP-tag) because it was stripping nickel from a standard immobilized metal affinity chromatography (IMAC) resin while the Laurence lab was making a protein previously unknown to bind metals. Given the ability of NCC to bind nickel, the MAP tag has the potential to be a useful biotechnological metal-delivery agent. However, prior to this work, the structure and chemical reactivity of the nickel-peptide complex were undefined. The work presented herein involves structural and reactivity investigations of the MAP-tag bound with Ni^{II} in the dianionic complex $[Ni\text{-}NCC]^{2-}$. A series of spectroscopic tools, including electronic absorption, circular dichroism (CD), magnetic CD (MCD), variable-temperature variable field (VTVH) MCD, and X-ray absorption (XAS), as well as density functional theory (DFT) and time-dependent (TD) DFT methods were used to provide insight into the structure of the complex. A summary of the significant findings in this work is provided below.

Spectroscopic and computational data collected of Ni-NCC conclude that Ni^{II} ion is bound in a 2N:2S square plane with coordination by the N-terminal amine nitrogen, the deprotonated backbone amide nitrogen of Cys2, and two cysteinate sulfur atoms from Cys2 and Cys3. This ligand environment is very similar to that of the nickel ion bound in the protein nickel superoxide dismutase (Ni-SOD), and comparison of the electronic absorption and CD spectra confirms that Ni-NCC and Ni-SOD have the same nickel primary coordination sphere. In addition, Ni-NCC is able to consume superoxide. Therefore, Ni-NCC is both a structural and

functional mimic of Ni-SOD and detailed analysis of the electronic and geometric structures of Ni-NCC can provide insight into the minimal unit necessary to afford activity in the enzyme.

Over time, the complex LLL-Ni^{II}-NCC undergoes site-specific chiral inversion to convert to DLD-Ni^{II}-NCC, as determined by spectroscopic analysis of authentic D-containing Ni-NCC peptide complexes and supported by DFT single point energy computations on geometry optimized models of the complex. This structural rearrangement enhances the superoxide scavenging ability of Ni-NCC. Intriguingly, this chiral inversion is not observed in either Ni-SOD or any small molecule mimics of the enzyme, and is therefore unique in this mimic. Upon evaluating the DFT-computed models, this rearrangement of LLL-Ni^{II}-NCC to DLD-Ni^{II}-NCC exposes one face of the nickel ion in the complex. This may allow for better interaction with exogenous molecules, like CN$^-$ and O$_2^-$. Thus, rearrangement within the complex increases superoxide consumption. Although other metal-peptide complexes are known to undergo metal-facilitated, base-catalyzed chiral inversion or racemization, the chiral inversion reaction of Ni-NCC does not demonstrate first-order dependence on hydroxide ion concentration. Therefore, the pathway to chiral inversion in Ni-NCC is distinct from other metal-peptide complexes.

Although the chiral inversion reaction of LLL-Ni^{II}-NCC to DLD-Ni^{II}-NCC is minimally affected by solution pH, the reaction is absolutely dependent on the presence of O$_2$. We propose that O$_2$ is required to oxidize the metal center to generate Ni^{III}-NCC, which is then able to undergo the inversion reaction. Generation of superoxide, as well as Ni^{III}, during the aging of LLL-Ni^{II}-NCC supports this hypothesis. Thiolate coordination in Ni^{II}-NCC reduces the effective nuclear charge of the nickel ion, necessitating oxidation to LLL-Ni^{III}-NCC before the chiral inversion reaction can be initiated. Additionally, DLD-Ni^{II}-NCC also undergoes a small extent of

O$_2$-dependent reactivity. However, spectroscopic characterization confirms that DLD-Ni^{II}-NCC reaches the same final state as LLL-Ni^{II}-NCC.

In order to characterize the structure of authentic, O$_2$-free, LLL-Ni^{II}-NCC and DLD-Ni^{II}-NCC, as well as the O$_2$-exposed forms of the peptides, Ni K-edge XAS was employed. This characterization of authentic, O$_2$-free LLL-Ni^{II}-NCC and DLD-Ni^{II}-NCC confirmed the proposed 2N:2S square planar coordination in Ni^{II}-NCC. Similarities of the pre-edge feature(s), edge energy, and radial distances determined for Ni^{II}-NCC with Ni^{II}-SOD and other Ni^{II}-SOD peptide mimics further supports that Ni-NCC is a structural mimic of the enzyme. In addition, XAS characterization of O$_2$-exposed LLL-Ni^{II}-NCC and DLD-Ni^{II}-NCC shows that, even during the chiral inversion reaction of Ni-NCC, the immediate structure about the nickel center does not significantly change.

Acknowledgements

Tim, your enthusiasm for science and teaching are contagious. Thank you for mentoring me and teaching me how to be a scientist. Also, thank you for supporting and encouraging my pursuit of both research and teaching endeavors. You are one of the best teachers I have ever had, and I am incredibly thankful and proud to have had the opportunity to be one of your first students. I look forward to hearing about your continued success.

To Jen and Mary, thank you for a wonderful collaboration. Our meetings were full of energy and enthusiasm, as well as fun. I cannot imagine a better melding of interests and expertise than the Jackson and Laurence labs and I am glad to have witnessed the beginning of what I suspect will be a long, productive collaboration. Mary, I tried to acknowledge in this text where you made significant contribution, not only to define who did what, but also to give you the substantial credit that you deserve.

In addition, thank you to my other committee members, Drs. David Benson, Misha Barybin and Emily Scott.

To the Jackson lab, I wish you all the best in your future endeavors, both in science and in life. It has been a blast to work side-by-side with you, and I truly consider you all friends. James, best of luck to you in law school and beyond. Thank you for being a great sounding board and study buddy. Domenick, enjoy being senior student in the lab and never lose your awesome laugh. Thank you for your patience in teaching me XAS data analysis very quickly. Gayan, continue educating (and confusing) the lab with your British English and never lose your enthusiasm for science. You'll be an awesome teacher. Hannah, thank you for being such a great friend. You are so strong and bright and fun, never lose that. You're going to make a rocking professor one day. Also, try

maintaining the legacy of the Jackson Lab Woman by confusing the boys and making yummy baked goods.

Jill, thank you for being there since the beginning and being my greatest teaching champion at KU. I'm very thankful that what started out as a great mentoring relationship has grown into a wonderful friendship. You are a phenomenal teacher, and I learned a lot just getting to be in your classroom and helping you with your class. Also, thank you Roderick and all of the KU professors who encouraged me as a teacher both in the classroom and in the laboratory.

To my dear friends, thank you for always being there to lend an ear or scientific insight. Cass, we've been friends for a long time and nobody gets me like you do. Mary, I look forward to collaborations and scientific conversations for years to come. Hannah, you've been such a breath of fresh air and I'm certain I've made a life-long friend in you. Megs, thanks for everything: the breakfasts, the laughs, the tears, and the time. Thank you for teaching me what a true friend is and always being real, beautiful you. My friendship with you is one of the things I will cherish most about my time at KU.

To my wonderful family, thank you all for your patience and never-ending love. Although you did not always understand what I was doing (or why it was taking so long!), you were willing to listen and encourage. Bradley, thank you for always being proud of me. Mama, thank you for being my first and best teacher. To my late father, thank you for always pushing me and never just giving me the answers. It's because of you and mama that I'm where I am, and I dedicate this work to your memory.

And to my husband Andy, thank you for being by my side and supporting, pushing, encouraging and loving me. Thank you for all of the manuscript edits, presentation practices, and late-night Malott Hall runs. You put your life on hold to support my dreams, and I will forever be grateful. I'm looking forward to what our future holds, and I know that it will be awesome with you by my side.

Table of Contents

List of Schemes and Figures

List of Tables

Chapter 1: The biological inorganic chemistry of nickel

There are eleven elements considered necessary for all kingdoms of biology: hydrogen, carbon, nitrogen, oxygen, sodium, magnesium, phosphorous, sulfur, chlorine, potassium and calcium.[3] Biological roles for molecules comprised of these elements are diverse and range from gas exchange to metabolism to genetic information storage. In addition to the eleven elements listed above, all organisms require some transition metal(s) for normal functioning. Transition metals offer diverse structural and reactivity properties that can be controlled and tuned by their local environment. These metals include the first-row transition metals vanadium, chromium, manganese, iron, cobalt, nickel, copper and zinc, as well as the heavier transition metals molybdenum and tungsten.[3] In addition to maintaining proper biological function, transition

Figure 1.1: The periodic table of the elements with biological roles highlighted. Elements necessary to all of biology (green), elements necessary in some forms of life (blue), elements used for therapeutic or imaging applications (red), and known bio-toxins (grey) are highlighted.[3-5]

metal elements can be employed as therapeutics and imaging agents. These various functions are summarized in Figure 1.1. In addition, Table 1.1 offers a summary of the primary function of several of the inorganic elements necessary for most classes of organisms.

Table 1.1. Classification of the biological function of several inorganic elements and compounds.[5]

Cellular Function	Inorganic Element/Ion/Molecule
Biomineralization	Ca^{2+}, Mg^{2+}, Fe^{3+}, Si, Sr^{2+}, $Cu^{\dagger}$, P
Brønsted acid-base buffering	PO_4^{3-}, Si, CO_3^{2-}
Charge balance	Na^+, K^+, Cl^-
Electron transfer	$Fe^{\dagger}$, $Cu^{\dagger}$, $Mo^{\dagger}$
Energy storage	H^+, PO_4^{3-}, S, Na^+, K^+, $Fe^{\dagger}$
Group (O, H, CH_3, etc.) transfer	$V^{\dagger}$, $Fe^{\dagger}$, $Co^{\dagger}$, $Ni^{\dagger}$, $Cu^{\dagger}$, $Mo^{\dagger}$, $W^{\dagger}$
Lewis acid-base catalysts	Zn^{2+}, Fe,† $Ni^{\dagger}$, $Mn^{\dagger}$
Redox catalysts	$V^{\dagger}$, $Mn^{\dagger}$, $Fe^{\dagger}$, $Co^{\dagger}$, $Ni^{\dagger}$, $Cu^{\dagger}$, $W^{\dagger}$, S^{2-}, Se^{2+}
Signaling	Ca^{2+}, B, NO
Structure/templating	Ca^{2+}, Zn^{2+}, Si, $S^{\dagger}$

† Elements that have different oxidation states, depending on the biological function.

1.1. Metals in proteins.

Although Figure 1.1 and Table 1.1 provide insights into the role of metal ions and inorganic molecules in biology, scientists have really just skimmed the surface in understanding how Nature does chemistry. Millions of years of evolution have allowed for very controlled reactivity in sometimes harsh (*i.e.* hydrothermal vents, acidic gastrointestinal tract, etc.) but often mild (near-neutral pH, atmospheric pressure, body temperature, etc.) conditions. We do know, however, that over one-third of the proteins characterized in the protein data bank (PDB) require a metal ion cofactor for either stability or reactivity.[14] Because Nature is able to affect specific reactions using Earth abundant and environmentally-friendly metals without producing toxic byproducts, the biochemical processes afforded at metal centers are very interesting to industrial and environmental chemists.

1.1.2. Electronic and geometric structure. Although the reactions performed at metal centers in biology can offer inspiration for the design of new molecules, the chemistry that the metals perform must be well understood. In addition to knowing the substrate(s) for the reactions, as well as the net reaction, intermediates en route to the final product must be well characterized. In order to understand the reactivity, the electronic and geometric structures at the metal centers for the duration of the chemical reaction(s) must be well characterized. Gaps in knowledge hinder rational catalyst and mimic design.

Many spectroscopic and computational methods exist for assessing ground and excited state electronic and geometric structures. An advantage over traditional X-ray diffraction (XRD) is that many of these techniques are solution phase and do not require the long-range order required of diffraction-quality crystals necessary for analysis by XRD. Spectroscopic techniques include electron paramagnetic resonance (EPR), electronic absorption (commonly called 'UV-Vis' or ultraviolet-visible), X-ray absorption (XAS), resonance Raman (rR), circular dichroism (CD), magnetic CD (MCD), and variable-temperature, variable-field MCD (VTVH-MCD) spectroscopies. In addition, density functional theory (DFT) computations, including time-dependent DFT (TD-DFT) methods can be employed to understand the ground and excited state structures. Computations have the distinct advantage of allowing a researcher to be hypothetical and speculative while approaching a question or problem. When combined with spectroscopic data, computations can be used to validate proposed models on the basis of collected spectroscopic data.

1.2 The biological inorganic chemistry of nickel

1.2.1 General properties of nickel. Nickel is a *d*-block metal with the electronic configuration $[Ar]4s^23d^8$. It is atomic number 28 in the periodic table and has an atomic mass of

58.69 amu. A. F. Cronstedt discovered nickel in 1751 and its name is derived from the Swedish word *kopparnickel* meaning "false copper" because it was initially mistaken for the other metal and created much frustration in ore extraction.[15] Five stable isotopes of nickel have been isolated with the designated natural abundances: ^{58}Ni (68.08%), ^{60}Ni (26.22%), ^{61}Ni (1.14%), ^{62}Ni (3.63%), and ^{64}Ni (0.93%). In addition, 18 radioisotopes of Ni have been documented with the two most stable being ^{59}Ni ($t_{1/2}$ = 76,000 years) and ^{63}Ni ($t_{1/2}$ = 100 years). The common oxidation states for nickel are Ni^0 and Ni^{2+}, although Ni^{-1}, Ni^{1+}, Ni^{3+}, and Ni^{4+} are accessible in certain conditions. Metallic nickel is a "silvery white" solid with a melting point of 1452 ^{o}C and density of 8.9 g/mL. However, the majority of nickel on earth is present in ores and alloys in combination with other elements including Fe, S, As, and Sb.

1.2.2 Coordination chemistry of nickel in proteins and peptides. There are two distinct geometries that d^8 Ni^{II} assumes in proteins, tetra-coordinate square planar Ni^{II}, and hexacoordinate octahedral. These geometries are also distinct from one another in their magnetic properties, as square planar Ni^{II} is diamagnetic whereas octahedral Ni^{II} is paramagnetic. Ni^{II} is a "borderline" Lewis acid according to Pearson's hard-soft acid-base (HSAB) theory and therefore forms stable complexes with intermediate Lewis bases, including imidazole, as well as some hard and soft bases including amines and thiolates, respectively.

Pseudooctahedral Ni^{II} is most commonly found in its high-spin configuration in proteins and peptides and therefore has a triplet ground state. Perusal of a Tanabe-Sugano energy level diagram predicts three spin-allowed bands in the electronic absorption spectrum, assigned as $^3A_{2g} \longrightarrow ^3T_{2g}$, $^3A_{2g} \longrightarrow ^3T_{1g}(F)$, and $^3A_{2g} \longrightarrow ^3T_{1g}(P)$. Due to the Laporte-forbidden nature of *d-d* transitions in an octahedral ligand field, these transitions will only carry weak intensity, and have extinction coefficients that range from $10 - 1000$ $M^{-1}cm^{-1}$.

Four-coordinate Ni^{II} complexes, and d^8 complexes in general, are typically planar, because the square plane ligand field causes one of the d orbitals, usually $d_{x^2-y^2}$, to be uniquely high in energy and allows the eight electrons to fill the other four d orbitals completely, leaving the destabilized antibonding orbital unfilled, yielding a singlet ground state. In pure D_{4h} symmetry, three spin-allowed transitions are observed in an electronic absorption spectrum: $^1A_{1g}$ $\longrightarrow$ $^1B_{2g}$, $^1A_{1g}$ $\longrightarrow$ ^1E_g, and $^1A_{1g}$ $\longrightarrow$ $^1B_{1g}$.

Higher oxidation states of Ni are supported in some systems, but only with ligands that are electron-rich or that have an anionic charge, to allow for better charge delocalization/covalency. In addition, the ligands must be strong σ donors to stabilize Ni^{III}. Given that the electronic configuration of Ni^{III} is $3d^7$ with an electronic spin state $S = \frac{1}{2}$, it is typically observable by EPR methods.

1.2.3 Nickel in biology. Nickel is required by algae, archaea, plants, fungi, and eubacteria to facilitate a variety of processes, including carbon monoxide and carbon dioxide metabolism, hydrogen uptake and production, generation of ammonia from urea, and consumption of superoxide.[13, 16, 17] Each of these nickel-catalyzed reactions allows organisms to thrive in extreme environments, including anaerobic and highly acidic surroundings. Bacteria that require nickel include some that populate the human gastrointestinal tract, making nickel an essential micronutrient.[18]

1.2.4 Nickel metalloenzymes. Given the variety of chemical reactions facilitated by nickel enzymes, it is not surprising that the metal-binding sites in these enzymes are diverse. Some enzymes feature a mononuclear nickel ion, whereas others are dinuclear and also employ iron. In addition, prosthetic groups including iron-sulfur clusters and the tetrapyrrole-derived cofactor F-430 are utilized in some nickel enzyme active sites. The geometry about the nickel

center(s) can be either octahedral or square planar and nickel oxidation states ranging from 0 to +3 are proposed in the catalytic cycles of these enzymes.[13] Figure 1.2 shows the diversity of nickel binding sites in metalloenzymes.
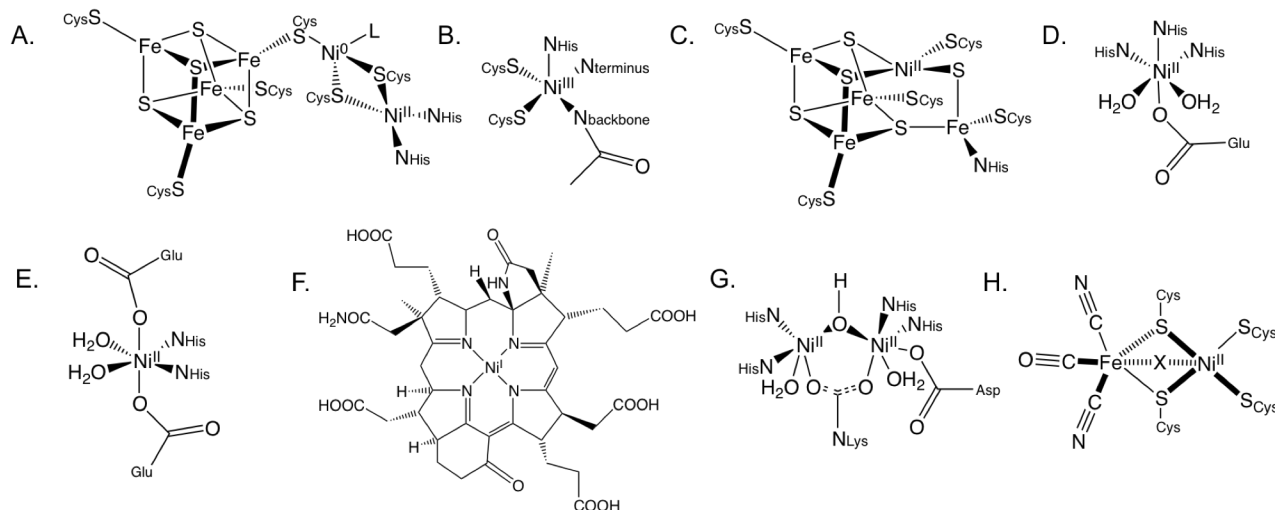
Figure 1.2. Active sites in nickel-containing enzymes. **A.** Acetyl-coenzyme A synthase, **B.** Nickel superoxide dismutase, **C.** CO dehydrogenase, **D.** Acireductone dioxygenase, **E.** *E. coli* glyoxylase I, **F.** Methyl-coenzyme M reductase, **G.** Urease, and **H.** Ni-Fe hydrogenase.

1.2.4.1. Nickel enzymes with octahedral, non-redox active, Ni^{II}. Six-coordinate Ni^{II} is employed in catalysis of three nickel metalloenzymes: glyoxylase I (GlxI), urease, and acireductone dioxygenase (ARD). In all three enzymes, Ni^{II} acts as a Lewis acid catalyst. The reactions catalyzed by these nickel-dependent enzymes are shown in Figure 1.3.

GlxI. Glyoxylase enzymes catalyze the detoxification reaction of methylglyoxal (MG) and other α-ketoaldehydes to their innocuous D-sugar, including D-lactate in the case of MG.[19, 20] Although its mechanism of toxicity is not known, the toxic effects of MG include lipid modification, increased apoptosis, and oxidative damage.[10] Glx enzymes have been characterized in most classes of life, spanning both prokaryotes and eukaryotes.[21] Most Glx enzymes require a Zn^{II} ion for activity, but it was discovered that *Escherichia coli* GlxI is inactive with Zn^{II} and, in
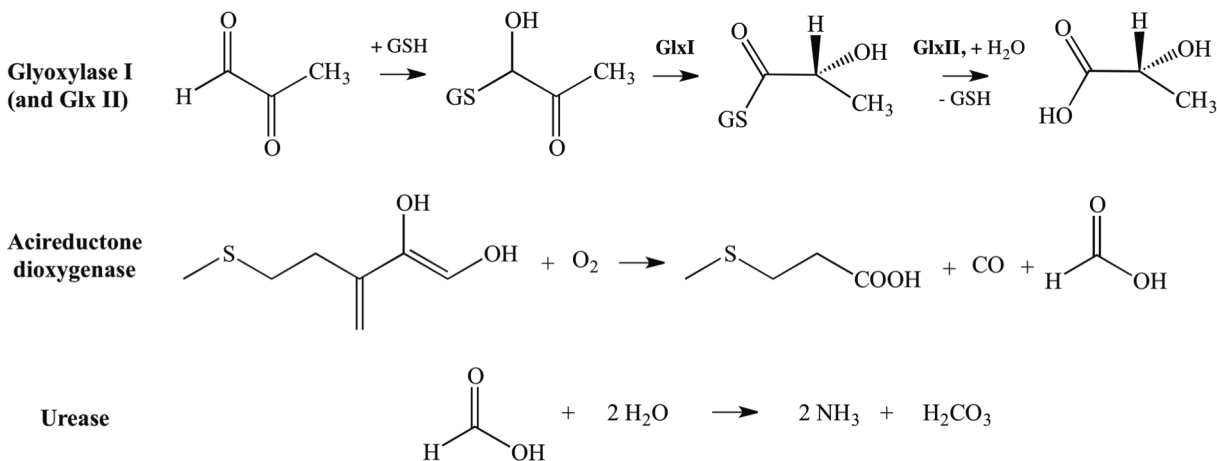
Figure 1.3. Metalloenzymes with reactions catalyzed by octahedral Ni^{II}, including Glyoxylase (top), acireductone dioxygenase (middle) and urease (bottom). "GS and GSH" represent the deprotonated and protonated forms of glutathione, respectively.

fact, has highest activity when bound to Ni^{II}.[22] In addition, at least three more classes of bacteria have GlxI enzymes that are most active when bound to Ni versus Zn.[23] However, this non-zinc binding class of GlxI enzymes are also capable of activity with other divalent metal ions including Co^{II}, so some refer to it as the "non-Zn GlxI" rather than nickel-dependent GlxI.[24] The flexibility of some protein active sites to various metal ions is curious and may be possible in these enzymes because of the simple Lewis acid properties of the metal ion. The active site and
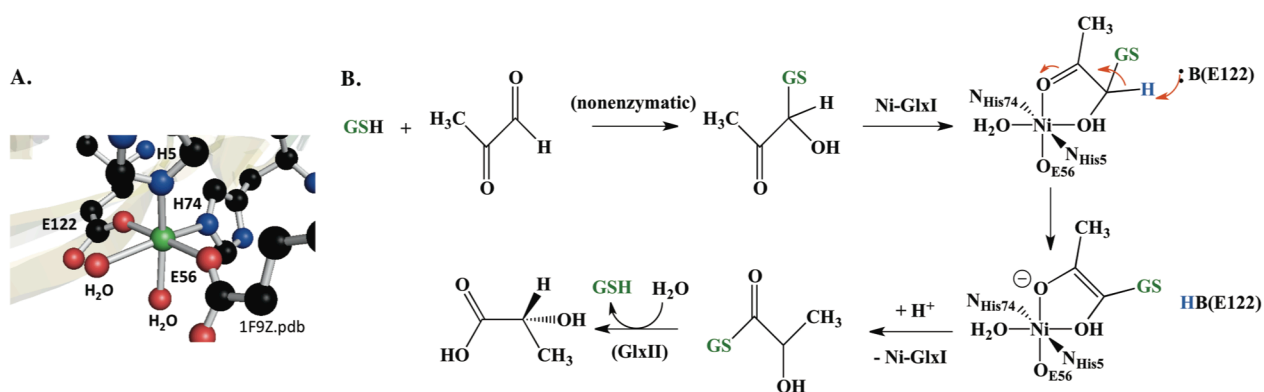
Figure 1.4. Active site (A.) and mechanism (B.) of GlxI from *E.coli*. [10] Substrate (methylglyoxyl) binds GSH to form a hemithioacetal adduct, which then binds the GlxI active site. An active site carboxylic acid (E122) acts as a general base and removes a proton. The enediolate intermediate then undergoes reprotonation to form GSH. GlxII catalyzes a hydrolysis reaction that forms product, D-lactate.

7

catalytic mechanism of Glx1 from *E. coli* are shown in Figure 1.4.

ARD. Acireductone dioxygenase catalyzes the second-to-last step in the ubiquitous methionine salvage pathway.[25] Methionine is an essential amino acid employed in the biosynthetic pathways of radical *S*-adenosylmethionine (SAM) enzymes that has to be rescued/salvaged for other uses in the body.[11] Although no mammalian nickel-dependent enzyme has been discovered to date, the realization that bacterial ARD requires nickel for activity led some to speculate that a mammalian form of the enzyme exits, but researchers have yet to discover it.[11] However, additional analysis determined that two ARD isoforms were isolated from *Klebsiella oxytoca*, ARD and ARD′, and they differ in both their metal ion binding as well as product distribution. ARD binds Ni^{II} and converts substrate into formate, CO, and methylthiopropionic acid. Alternatively, the on-pathway ARD′ binds Fe^{II} and converts acireductone into 2-keto-4-(methylthio)butyrate and formate, the former of which can be converted to methionine by transaminase to complete the methionine salvage pathway.

ARD activity depends purely on the metal ion added in vitro, as product distribution can be shifted by removing one metal and re-constitution of the enzyme with the other metal.[26] However, the structures of the two isoforms are distinct, as they can be separated chromatographically and NMR data are consistent with very different structures when comparing Ni ARD versus Fe ARD′.[11]

In addition, although ARD is the only nickel-dependent dioxygenase, the metal itself does not bind the O_2 substrate. It remains to be seen whether the chemistry of ARD is biologically relevant. Production of CO is particularly curious, in the context of the possibility of ARD in higher organisms, as CO is known to be a signaling molecule in mammals.[11] The active site structure and mechanism of ARD are shown in Figure 1.5.
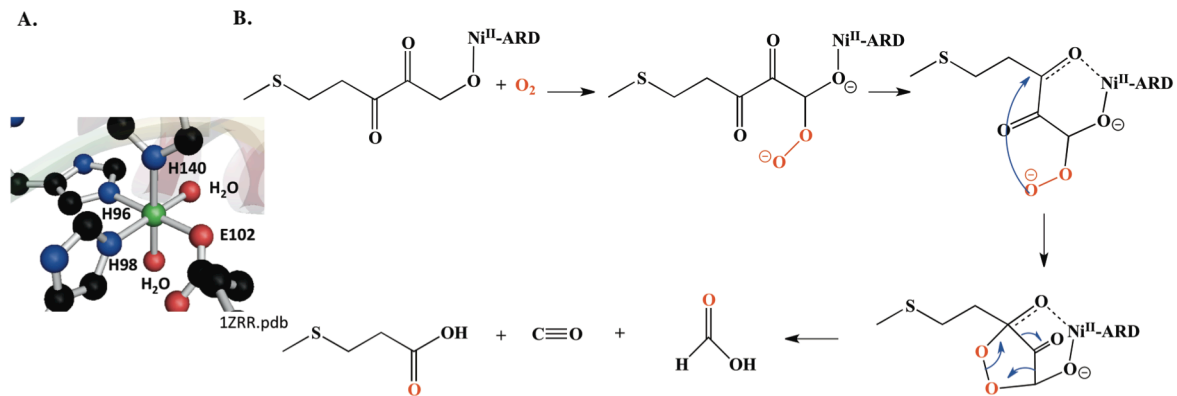
Figure 1.5. Active site (A.) and proposed mechanism (B.) of ARD.[11] First, an electron is transferred from doubly-deprotonated acireductone to O_2, to form a superoxo that subsequently attacks substrate carbon and forms a peroxo adduct. Metal-stabilized nucleophilic attack of the bound peroxo on the carbon follows and forms a five-membered ring intermediate that undergoes rearrangement to form product. The product distribution is shown. ARD', which binds iron, follows an alternative mechanism and produces the on-pathway products that can complete the methionine salvage pathway. As was mentioned in the text, the importance of the nickel-bound form and production of CO has yet to be determined.

Urease. Urease was the first protein ever crystallized and the first nickel-dependent metalloenzyme discovered.[27, 28] The crystallization of urease proved that catalysts could be made of pure proteins, and the discovery of the nickel centers in urease proved nickel an essential nutrient in biology.[24] Like ARD and GlxI, nickel in urease is redox-inactive and stays Ni^{II} for the duration of enzymatic turnover. However, urease is distinct in that it features a binuclear nickel active site, which can be seen in Figure 1.6A.

As its name implies, urease catabolizes urea into ammonia and carbonic acid. Because of its production of basic ammonia, the enzyme is used by pathogens as a virulence factor to allow them to inhabit regions of low pH, including the gastrointestinal tract of humans and other animals.[29] In addition, although not produced by mammals, urease plays a key role in the global nitrogen cycle because it fixes urea, which is produced by higher organisms as a waste product.[13] Urease also has a key agricultural role, because both microbes in the soil and some plants break down the urea into ammonia, which can be used for the plants as fertilizer.[30] Four additional
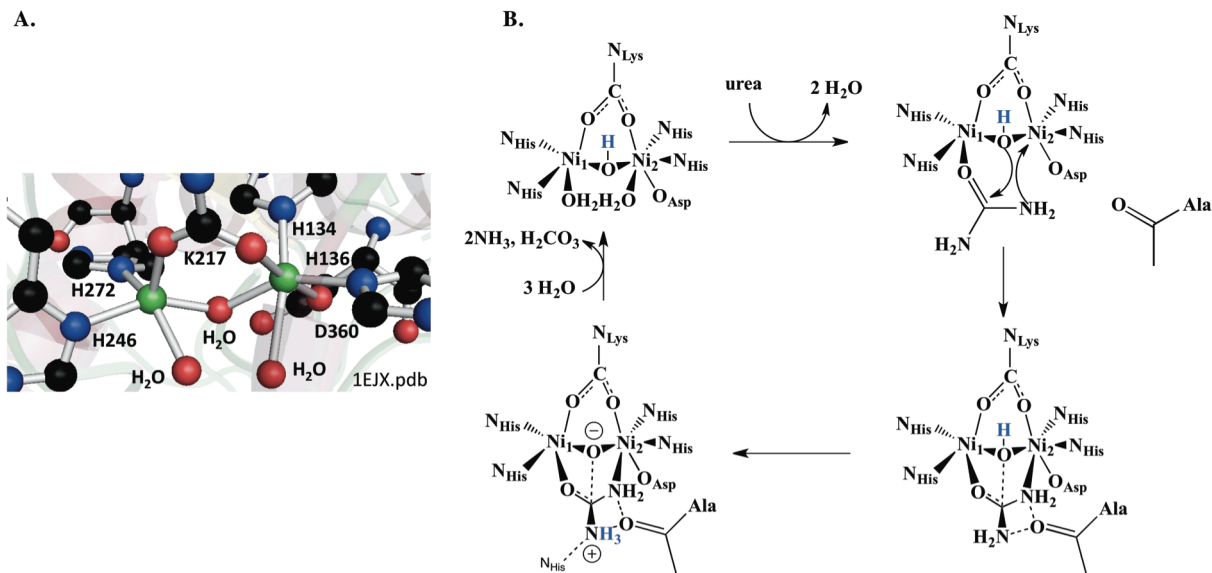
Figure 1.6. Active site (A.) and mechanism (B) of urease. A. The active-site structure highlights the dinuclear nickel centers. The geometry of the two centers is distinct, with one 5C square pyramidal Ni and one 6C pseudo-octahedron. A unique carbamylated lysine residue bridges the two metal centers. B. Mechanism of action for urease.[8] Substrate binds the 5C Ni_1 center, then following flap closure and protein rearrangement, substrate bridges the two metal centers to allow for proton transfer to produce product.

proteins; UreD, UreE, UreF, and UreG; are required for metal cofactor assembly and carbamylation of the active site Lys residue in *E. coli* urease.[31] The requirement of the accessory proteins for full activity varies depending on the organism; therefore individual roles will not be discussed here. However, UreE has been implicated as a nickel metallochaperone and may therefore serve to deliver nickel from the cellular milieu to the active site of urease.[32-34] The mechanism of urease is shown in Figure 1.6B.

1.2.4.2 Nickel enzymes in the global carbon cycle. As listed previously, carbon is one of the eleven elements necessary for life. The global carbon cycle involves the oxidation of organic substrates to CO_2 and the reduction of CO_2 back to organic carbon. Oxidation of organic substrates in organisms is how cells get the energy they need to live. In addition, reduction of CO_2 requires the input of energy but is coupled to carbon fixation to generate the biomolecules necessary for life. There are three nickel-dependent metalloenzymes that employ carbon-

Carbon monoxide dehydrogenase (CODH) $2\,e^- + 2\,H^+ + CO_2 \rightleftharpoons CO + H_2O$

Acetyl conenzyme-A synthase (ACS) $CH_3\text{-CFeSP} + CO + \text{CoA-SH} \rightleftharpoons CH_3\text{-CO-SCoA} + CFeSP + H^+$

Methyl coenzyme-M reductase (MCR) $CH_3\text{-S-CoM} + \text{CoB-SH} \longrightarrow CH_4 + \text{CoM-S-S-CoB}$
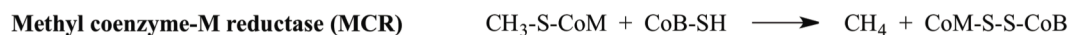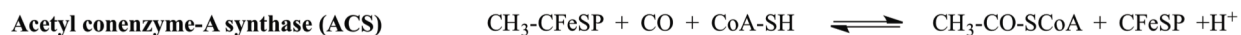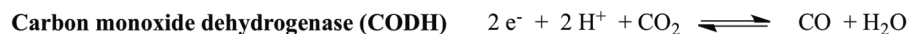
Figure 1.7. Chemical reactions catalyzed by CODH, ACS, and MCR. All of these enzymes employ nickel coordination in their active site and are part of the global carbon cycle.

containing gases as either substrate or product, carbon monoxide dehydrogenase (CODH), acetyl coenzyme-A synthase (ACS), and methyl coenzyme-M reductase (MCR). The reactions that these proteins catalyze are shown in Figure 1.7. ACS and CODH are ancient enzymes, believed to be responsible for early organism survival in the CO_2-rich atmosphere present at the origin of life.[35] In addition, MCR is the sole enzyme responsible for all biogenic methane production. CH_4 and CO_2 are both greenhouse gases and CO is an environmental pollutant and bio-toxin. Together these enzymes play a major role in the global carbon cycle in both the formation and removal of these gases. Because the majority of the substrates for these enzymes contain carbon, all three of these enzymes employ organometallic, or direct carbon-metal bonds, chemistry which is rare in biology.

CODH. Carbon monoxide dehydrogenases catalyze the reversible oxidation of CO to CO_2 and allow organisms to live with CO or CO_2 as their only carbon and energy source.[31] Two distinct types of CODHs have been characterized, different in their O_2-dependence and metal ion distribution. CODHs found in aerobic microbes, including *Oligotropha carboxidovorans*, employ copper and molybdenum centers, whereas CODHs from archaea and anaerobic microorganisms, such as *Carboxydothermus hydrogenoformans*, use nickel and iron at their active site. The focus of this discussion will be on the anaerobic, nickel-dependent CODHs. CODH has been isolated as both a monofunctional enzyme and in complex with ACS as a bifunctional CODH/ACS enzyme. Total metal content in these two classes of CODH vary,

although both employ iron and nickel. The active site that is responsible for binding and oxidizing CO in CODH is the C-cluster, which contains four iron atoms and one nickel. Figure 1.8 shows one of the proposed structures for the C-cluster. Crystal structures solved from different organisms vary in coordination environment around the nickel center.[1, 2, 36-38] However, all feature a [3Fe-Ni-4S] cluster bound to a mononuclear iron site. It has been proposed that the fully-active form is the tetra-sulfur coordinated square planar nickel site, with a bridging sulfido to the mononuclear Fe, and the other structures represent degradation products.[37] Both the mechanism and active site C cluster are shown in Figure 1.8.
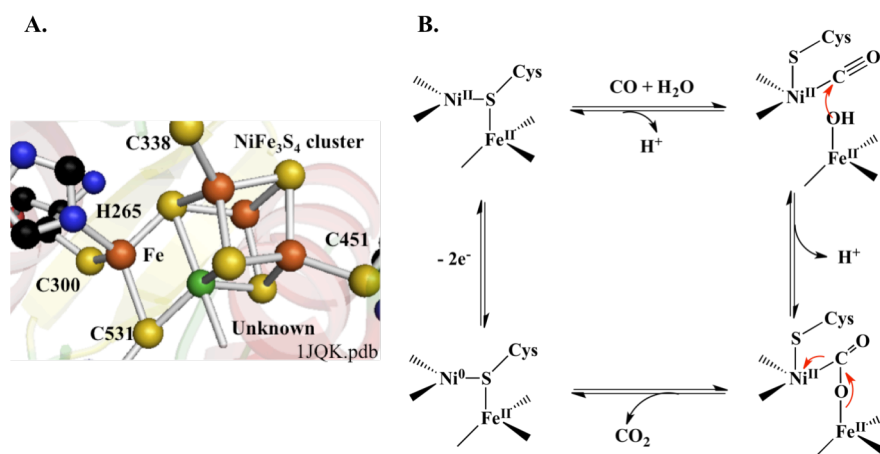
Figure 1.8. Active site (A.) and proposed mechanism (B.) of CODH.[12] For simplicity, not all ligands are shown in the mechanism. Electron transfer events are designated with red arrows. First, CO binds the Ni^{II} center and hydroxide binds the mononuclear Fe^{II}. The OH group attacks the metal-bound CO to form a bridged carboxylate. Internal electron transfer produces CO_2 and reduces Ni^{II} to Ni^0. Ni is oxidized back to Ni^{II} with a biological oxidant, proposed to be ferredoxin.

ACS. As its name implies, acetyl coenzyme-A synthase catalyzes the reversible acetylation of CoA using a methyl group transferred from the corrinoid-iron-sulfur protein (CFeSP) and CO.[39] The high-energy thioester bond of acetyl-CoA is used in generation of the cellular energy molecule adenosine triphosphate, ATP.[35] In Nature, ACS does not exist alone, but as the bifunctional CODH/ACS complex.[40] This allows for direct transfer of CO from the C-
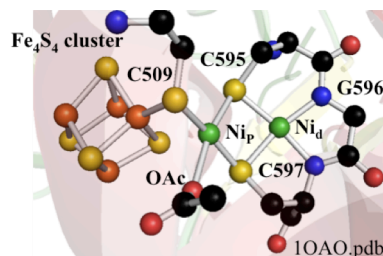
Figure 1.9. Active site A-cluster of ACS showing the [4Fe-4S] cubane and the two distinct nickel-binding sites, Ni_p and Ni_d.

cluster of CODH to the active site A-cluster of ACS. Not surprisingly, a 66 Å amino acid channel connects the CODH C-cluster to the ACS A-cluster, to facilitate CO delivery.[41]

The ACS A-cluster features a [4Fe-4S] cluster as well as two other mononuclear nickel binding sites, named proximal nickel (Ni_p) and distal nickel (Ni_d). Although XRD structures were solved with Cu, Zn and Ni modeled in the proximal binding site, only the nickel-bound form has activity.[1, 2, 42-44] Figure 1.9 shows the A-cluster of ACS, with nickel in the proximal binding-site. Although the identity of the proximal metal has been identified, several questions regarding the mechanism of turnover remain and are the focus of current research.[43]

The mechanism of ACS has not yet been fully elucidated, although researchers have made significant progress.[1, 2] The two main proposed mechanisms are shown below in Scheme 1.1. The main questions that remain revolve around the Ni_p and Ni_d oxidation states at each of the steps. Because of this, as well as the unique organometallic nature of many of the intermediates, small molecule mononuclear complexes have been the focus of reactivity and spectroscopic analysis, although the protein has been significantly characterized as well.[45-50]

Scheme 1.1. The two main proposed mechanisms for catalysis in ACS, developed by Ragsdale (2.1.A) and Lindahl (2.1.B.).[1, 2] The oxidation states of Ni_p and Ni_d throughout turnover differ between the two mechanisms, especially with regards to state upon CO and CH_3, binding. Other proteins are shown in ellipses. For the sake of clarity, only Ni_p is shown in the cycles, but the whole active site is shown below the two mechanisms. Regardless of the mechanisms, the general steps are carbonylation, followed by transmethylation from CFeSP, C-C bond formation, and finally acetylation of CoA.
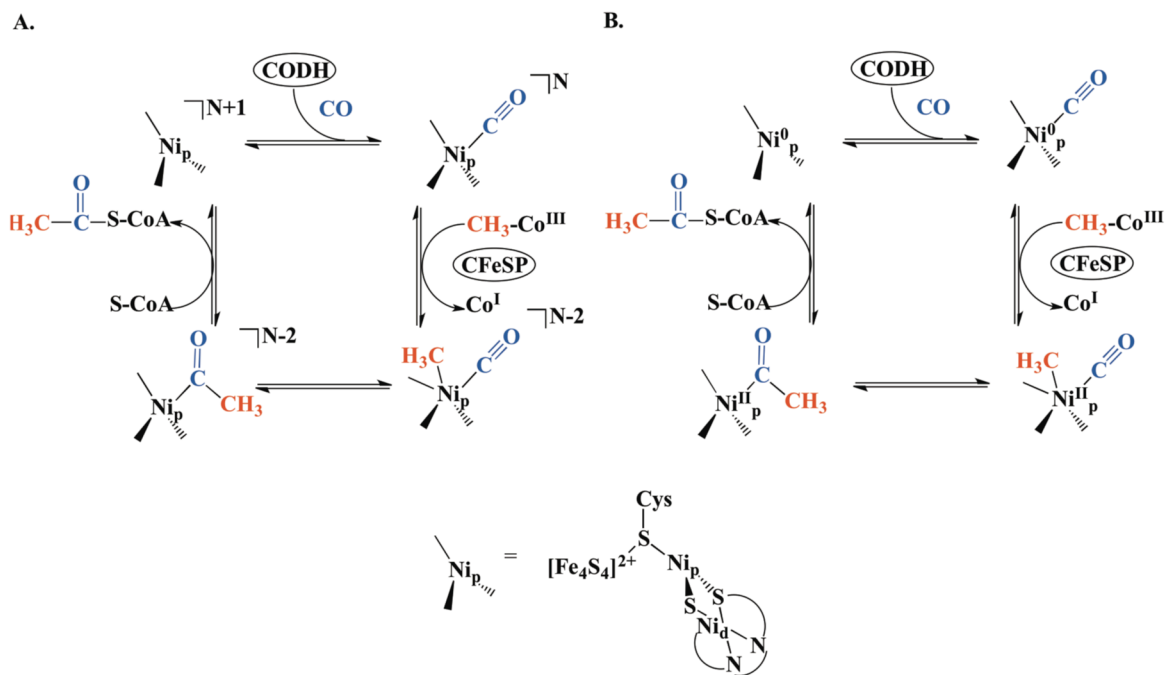
MCR. Methyl coenzyme-M reductase catalyzes disulfide bond formation between
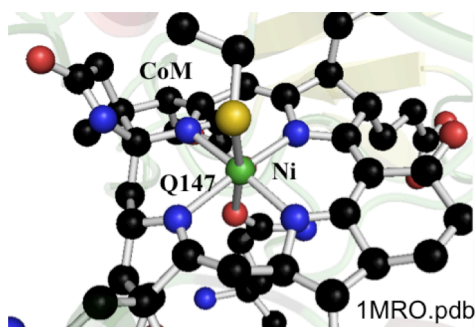
Figure 1.10. Active site F-430 cofactor of MCR, bound with coenzyme-M, one of the substrates of the enzyme.

coenzyme-M and coenzyme-B with concomitant formation of methane.[51] The greenhouse gas is just a byproduct of the reaction, as the disulfide bond CoM-S-S-CoB is the physiologically relevant product of the MCR reaction. Reduction of the disulfide bond formed between the two coenzymes is highly exergonic, and is coupled with ATP synthesis in the organisms.[52] Although the exact pathway from carbon substrate to CH_4 varies, MCR is the terminal enzyme responsible for all methane production in biology.[52] Methanogenic bacteria produce approximately one billion tons of the gas per year, with one-third being released into the environment as a greenhouse gas.[52] The active site of MCR employs the unique F-430 cofactor, a tetrahydrocorphin so named because of the four pyrrole rings that form its corphin core.[53] Indeed, F-430 is the most reduced tetrapyrrole in nature, with only five double bonds, and

Scheme 1.2. Mechanisms of reactivity in MCR, proposed by Thauer[9] (1.3.A) and Ragsdale[13] (1.3.B). In mechanism A, the reaction is initiated by nucleophilic attack by Ni^I on CH_3-CoM to generate the Ni^{III}- CH_3 organometallic intermediate and CoM. This is followed by electron transfer to generate a CoM radical, which then reacts with CoB to form a disulfide radical anion with concomitant H^+ transfer to the nickel-bound methyl substituent. This releases CH_4 and reduces the metal to Ni^{II}. The enzyme is returned to its resting state by reduction to Ni^I by electron transfer from the radical anion. In mechanism B, NiI initiates cleavage of the S-C bond in CH_3-CoM to form a Ni(II)-bound CoM and a methyl radical. This radical then abstracts an H atom from CoB to generate a thiyl radical-CoB. At this point, the mechanisms converge. Briefly, formation of the disulfide radical anion followed by regeneration of the resting state of MCR and the CoM-S-S-CoB product.
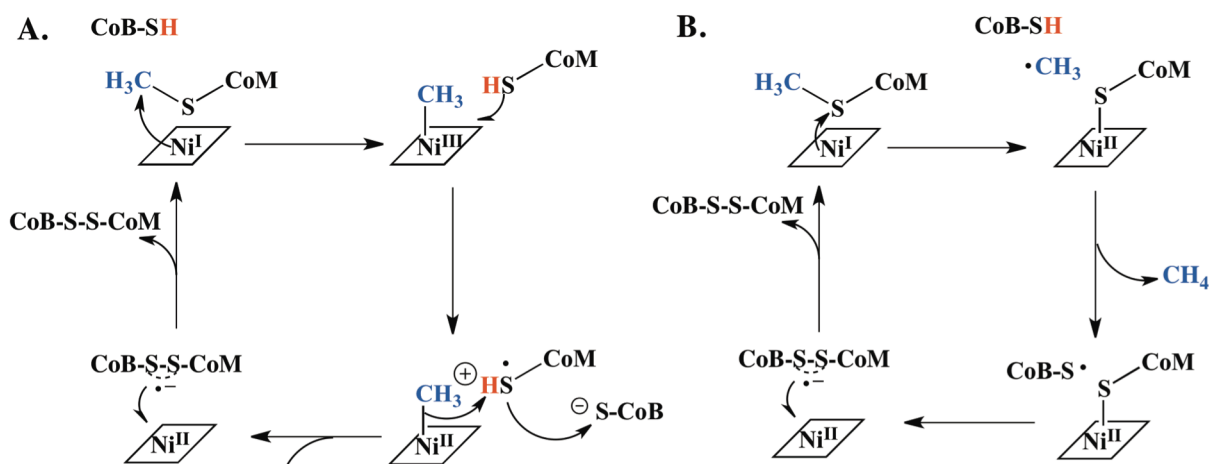
therefore has a puckered structure. The structure of F-430 is shown in Figures 1.2.F and 1.10 and the macrocycle itself can adopt at +1, +2, or +3 charge, depending on protonation state.

There are two proposed mechanisms for methanogenesis and disulfide bond formation in MCR, shown in Scheme 1.2. These two mechanisms differ in the proposed transfer of electrons, and specifically whether an organometallic Ni-CH$_3$ or •CH$_3$ radical intermediate is formed.[9, 13] Although both have some support, either experimentally or computationally, they both have disadvantages as well and it has been proposed by Ermler that an additional mechanism is necessary.[52]

1.2.4.3. Two additional redox-active nickel enzymes. In addition to the three enzymes associated with the global carbon cycle, there are two other redox-active nickel-dependent metalloenzymes, nickel superoxide dismutase (Ni-SOD) and nickel-iron hydrogenase ([NiFe]-hydrogenase). Both Ni-SOD and [Ni-Fe]-hydrogenase are members of larger classes of enzymes, SODs and hydrogenases respectively, which bind different metals depending on the organism. The reactions catalyzed by these two enzymes are shown in Figure 1.11.

[NiFe]-hydrogenase. Hydrogenase enzymes catalyze the reversible two-electron reduction of two protons to form H$_2$.[54] There are three main classes of hydrogenase enzymes, mononuclear [Fe]-hydrogenase, homodinuclear [FeFe]-hydrogenase, and heterodinuclear [NiFe]-hydrogenase.[55] In addition to these broad classes, hydrogenase enzymes can either be soluble or membrane-associated.[56] The oxidation of H$_2$ is coupled to reduction of biologically-important

Ni-superoxide dismutase $\quad 2\,H^+ + 2O_2^{\cdot-} \rightleftharpoons O_2 + H_2O_2$

Ni-Fe hydrogenase $\quad 2H^+ + 2e^- \longrightarrow H_2$
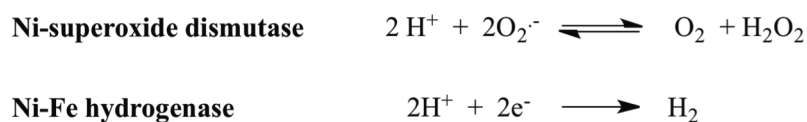
Figure 1.11. Chemical reactions catalyzed by Ni-SOD and [NiFe]-hydrogenase.

electron acceptors in anaerobic microorganisms, and therefore serves as a source of energy for the microbes.[24]

The active site of [NiFe]-hydrogenase features both a nickel ion as well as a low-spin (LS) Fe^{II} center coordinated by the unusual strong-field CN^- and CO ligands.[57, 58] The heterodinuclear metal centers are bridged by two cysteinate ligands. In addition, two deprotonated cysteine thiolates complete the coordination sphere of the nickel. The [NiFe]-hydrogenase active site is shown in Figure 1.12. These ligands likely are present in order to keep the Fe^{II} in its LS electronic state during the redox turnover of the enzyme.[13] Because the active site of the enzyme is buried deep within the protein, several channels exist to shuttle protons, electrons, and H_2 to the active site and away to the cellular milieu. Electron transfer happens via a series of iron-sulfur clusters that form a so-called wire to couple the hydrogenase active site to the external electron donor/acceptor.[59]

Although the reaction that [NiFe]-hydrogenase catalyzes is simple, the mechanism of
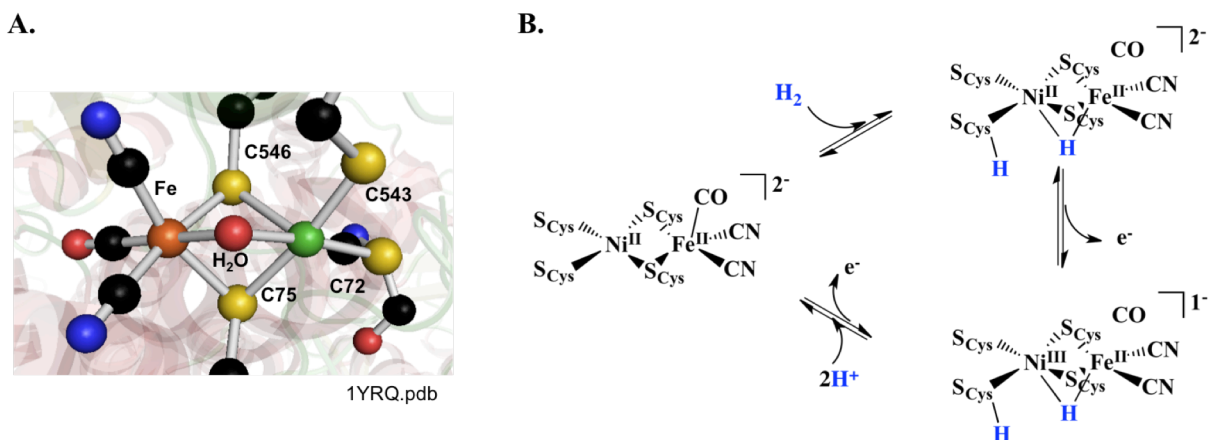
Figure 1.12. Active site (A.) and proposed mechanism (B.) for [NiFe]-hydrogenase. The crystal structure features a bridging water ligand, in addition to the cysteine residues, and may serve as the site of bridging H^- during turnover. The mechanism shows that upon H_2 addition, one of the nickel-bound cysteine residues accepts an H and a bridging hydride binds both metals. Oxidation of nickel to Ni^{III} allows for removal of one electron. Addition of two H^+ and removal of an additional electron returns the enzyme to its resting state.[6, 7]

action is still unclear. The site of H_2 binding, source of H^+, and nickel oxidation state at various points in the turnover is still unclear. However, DFT and spectroscopic analysis agree that H_2 first binds to a $Ni^{II}Fe^{II}$ active site and that the Fe^{II} electronic state does not change during turnover.[60] The simplest mechanism of [NiFe]-hydrogenase is shown in Figure 1.12.

Ni-SOD. Superoxide dismutase enzymes catalyze the breakdown of the toxic byproduct of oxidative metabolism superoxide, to hydrogen peroxide and dioxygen. There are four classes of SODs, distinct in their metal ion center(s), Mn-, Fe-, Cu/Zn- and Ni-SOD.[61] Of the four SODs, Ni-SOD is the most recently-characterized, and perhaps the most surprising, as the nickel coordination in Ni-SOD employs sulfur ligands, which are prone to oxidation by O_2 and its reduced derivatives.[62, 63]
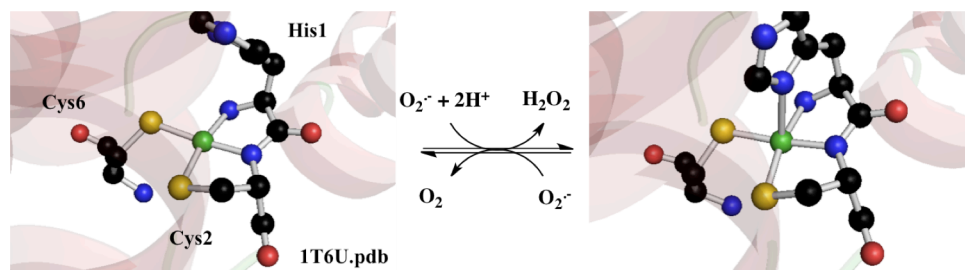
Figure 1.13. Reduced (left) and oxidized (right) Ni-SOD, along with the chemical reactions it catalyzes.

The active site of Ni-SOD is shown in Figure 1.13. X-ray crystal structures of the Ni^{II} and Ni^{III} forms of Ni-SOD show a change in coordination depending on the nickel oxidation state.[62] In the Ni^{II} state, the metal center is bound in a square planar geometry by two cysteinate ligands, the N-terminal amine, and a deprotonated peptide backbone amide. Because the metal-binding domain is within the first six amino acid residues of the protein sequence, these residues are named the nickel-binding "hook". In the Ni^{III} oxidation state a five-coordinate metal center is observed, with an imidazole nitrogen from His1 being added as the fifth ligand. Ni-SOD is the

only mononuclear SOD that undergoes a change in coordination number at the active-site metal during catalytic turnover, further distinguishing it from the other SODs. Very recent work has shown that the control of the $Ni^{II/III}$ redox couple in Ni-SOD is due both to the specific ligand environment, as well as the ability of the enzyme to shift between the square planar and square pyramidal geometries.[64] Although crystal structures of both the oxidized and reduced forms of the protein have been documented, many questions still exist regarding the mechanism of action of Ni-SOD. It is unclear whether substrate binds directly to the metal center to facilitate an inner-sphere electron transfer, or whether it is an outer-sphere interaction. Recent crystal structures of Ni-SOD mutants bound to halide ions in a putative anion-binding site show a distance of 3.5 Å between the metal center and anion, supporting an outer sphere mechanism.[65] In addition, it is unknown when the fifth ligand, the His imidazole, is in the "off" and "on" position with respect to the metal center during turnover. Figure 1.13 shows a schematic of the Ni-SOD reaction.

In addition to characterization of the whole protein, much that is known about Ni-SOD has been determined with the study of small-molecule mimics of the enzyme.[66-72] Three distinct classes of mimics have been employed: peptide maquettes derived from the sequence of the protein, other peptides not from the Ni-SOD sequence, and synthetic small molecules. The synthetic small molecules typically only function as structural models of the enzyme, as they are unable to switch nickel ion oxidation state and are therefore unable to consume superoxide.[66] However, characterization of these structural mimics can provide insights into potential intermediates in the reactions of Ni-SOD. The maquettes are unique in that they contain all of the metal-binding residues found in the native enzyme, given that the metal-binding hook in Ni-SOD is only the first six residues.[67, 70, 71] Indeed, the maquettes are able to consume superoxide, albeit not to the extent that Ni-SOD does. A suite of complexes using a tridentate small peptide not

derived from the enzyme sequence along with exogenous thiolates has also been employed in order to provide insight into the active-site environment in Ni-SOD.[73]

1.3 Motivation for this work

Although this review is in no way exhaustive, it serves to explain what is generally understood about the structures, reactivities and mechanisms of the eight nickel-dependent enzymes characterized to date. Much of what has been learned has been assisted by the use of small molecule mimics of the proteins, as well as by site-directed mutagens that were developed to probe the role(s) of specific amino acid residue(s). Spectroscopic tools, as well as computations and structural analysis via NMR and XRD techniques, have helped to develop the breadth of knowledge we currently have regarding this diverse family of enzymes. However, there are still challenges in understanding the chemistry orchestrated at the nickel centers in each of these enzymes.

Of the eight nickel-containing enzymes that have been characterized to date, those that facilitate redox processes at the metal center all feature active site nickel ions with sulfur coordination by cysteinate ligands.[66] These redox-active enzymes include nickel iron hydrogenase, carbon monoxide dehydrogenase, acetyl-coenzyme A synthase, methyl-coenzyme M reductase, and nickel superoxide dismutase (Ni-SOD). Acireductone dioxygenase seems to serve as an exception, because it catalyzes an oxidation reaction and utilizes a Ni^{II} center coordinated in a three nitrogen, three oxygen (3N:3O) octahedral environment.[67] However, for this enzyme, oxidation is proposed to occur directly at substrate without change in the nickel oxidation state.[25, 67] Because only those enzymes with direct sulfur-nickel bonding employ a

redox-active nickel center, it has been proposed that sulfur coordination is responsible for tuning the $Ni^{II/III}$ reduction potential to a biologically-accessible range.[66]

This sulfur-mediated redox tuning is exemplified in the protein Ni-SOD. Aquated Ni^{II} has a reduction potential of 2.29 V, (versus normal hydrogen electrode, N.H.E.) making the Ni^{III} state inaccessible in water.[68] However, the metal center in Ni-SOD is able to catalyze both the oxidation and reduction of superoxide, to O_2 and H_2O_2 respectively, reactions which have standard reduction potentials of 160 mV and 870 mV correspondingly.[62, 69] Although there are three other classes of SODs, distinguished by their different active site metal centers, Ni-SOD is the only SOD to employ sulfur ligation. Complexes with transition metal thiolates are known to be sensitive to oxidation by dioxygen and its reduced derivatives and the complexes frequently dimerize upon exposure to O_2.[70-76] Therefore it is curious that Nature has evolved a nickel-dependent SOD with thiolate coordination that undergoes nickel-centered rather than ligand-based oxidation. Additionally, where and how substrate interacts with the active site in Ni-SOD is still unknown, and it is unclear whether superoxide interacts with nickel via an inner sphere or outer sphere mechanism.

The tripeptide asparagine-cysteine-cysteine is able to bind nickel tightly to form the complex Ni-NCC. The spectroscopic and computational analyses presented in this thesis have allowed for assignment of Ni-NCC as both a structural and functional a mimic of Ni-SOD. Therefore, characterization of Ni-NCC can provide insights into the structure and reactivity of Ni-SOD.

1.4. References

1.   Darnault, C.; Volbeda, A.; Kim, E. J.; Legrand, P.; Vernede, X.; Lindahl, P. A.; Fontecilla-Camps, J. C., *Nat. Struct. Biol.* **2003,** *10* (4), 271-279.

2.   Doukov, T. I.; Iverson, T. M.; Seravalli, J.; Ragsdale, S. W.; Drennan, C. L., *Science* **2002,** *298* (5593), 567-572.

3.   Frausto da Silva, J. J. R.; Williams, R. J. P., The chemical elements in biology. In *The biological chemistry of the elements: The inorganic chemistry of life*, 2 ed.; Oxford University Press: Oxford, 2001; pp 7 -28.

4.   Sadler, P. J., Metals in Medicine. In *Biological Inorganic Chemistry: Structure and Reactivity*, Bertini, I.; Gray, H. B.; Stiefel, E. I.; Valentine, J. S., Eds. University Science Books: Sausalito, California, 2007; pp 95 -135.

5.   Ivano Bertini, H. B. G., Edward I. Stiefel, Joan Selverstone Valentine, Introduction and Text Overview. In *Biological Inorganic Chemistry: Structure and Reactivity*, Ivano Bertini, H. B. G., Edward I. Stiefel, Joan Selverstone Valentine, Ed. University Science Books: Sausalito, California, 2007; pp 1 - 3.

6.   De Gioia, L.; Fantucci, P.; Guigliarelli, B.; Bertrand, P., *Inorg. Chem.* **1999,** *38* (11), 2658-2662.

7.   De Gioia, L.; Fantucci, P.; Guigliarelli, B.; Bertrand, P., *Int. J. Quantum Chem.* **1999,** *73* (2), 187-195.

8.   Ciurli, S., Urease: Recent Insights on the Role of Nickel. In *Nickel and Its Surprising Role in Nature*, SIgel, A.; SIgel, H.; Sigel, R. K. O., Eds. John Wiley and Sons, Ltd.: West Sussex, England, 2007; Vol. 2, pp 241 - 278.

9. Juan, B.; Thauer, R. K., Methyl Coenzyme-M Reductase and its Nickel Corpin Coenzyme F430 in Methanogenic Archaea. In *Nickel and its Surprising Impact in Nature*, Sigel, A.; Sigel, H.; Sigel, R. K. O., Eds. John Wiley & Sons, Ltd.: West Sussex, United Kingdom, 2007; Vol. 2.

10. Sukdeo, N.; Daub, E.; Honek, J. F., Biochemistry of the Nickel-Dependent Glyoxalase I Enzymes. In *Nickel and Its Surprising Impact in Nature*, Sigel, A.; Sigel, H.; Sigel, R. K. O., Eds. John Wiley and Sons, Ltd.: West Sussex, Englad, 2007; Vol. 2, pp 445 - 472.

11. Pochapsky, T. C.; Ju, T.; Dang, M.; Beaulieu, R.; Pagani, G. M.; OuYang, B., Nickel in Acireductone Dioxygenase. In *Nickel and Its Surprising Role in Nature*, Sigel, A.; Sigel, H.; Sigel, R. K. O., Eds. John Wiley and Sons, Ltd.: West Sussex, England, 2007; Vol. 2, pp 473 - 500.

12. Ragsdale, S. W., Enzymology of the Wood-Ljungdahl pathway of acetogenesis. In *Incredible Anaerobes: From Physiology to Genomics to Fuels*, Wiegel, J.; Maier, R. J.; Adams, M. W. W., Eds. 2008; Vol. 1125, pp 129-136.

13. Ragsdale, S. W., *J. Biol. Chem.* **2009,** *284* (28), 18571-18575.

14. Lieberman, R. L.; Rosenzweig, A. C., Metal Ion Homeostasis. In *Coordination Chemistry II*, 2003; Vol. 8, pp 195-211.

15. Dinga, G. P., *Chemistry* **1968,** *41* (2), 20 - 22.

16. Kaluarachchi, H.; Chung, K. C. C.; Zamble, D. B., *Nat. Prod. Rep.* **2010,** *27* (5), 681-694.

17. Maroney, M. J., *Curr. Opin. Chem. Biol.* **1999,** *3* (2), 188-199.

18. Nieboer, E.; Tom, R. E.; Sanford, W. E., Nickel metabolism in man and animals. In *Metal Ions in Biological Systems*, Sigel, H.; Sigel, A., Eds. Marcel Dekker, Inc.: New York, 1988; Vol. 22.

19. Neuberg, C., *Biochem. Z.* **1913,** *49*, 502-506.

20. Racker, E., *J. Biol. Chem.* **1951,** *190* (2), 685-696.

21. Thornalley, P. J., *Biochem. Soc. Trans* **2003,** *31*, 1343-1348.

22. Clugston, S. L.; Barnard, J. F. J.; Kinach, R.; Miedema, D.; Ruman, R.; Daub, E.; Honek, J. F., *Biochemistry* **1998,** *37* (24), 8754-8763.

23. Sukdeo, N.; Clugston, S. L.; Daub, E.; Honek, J. F., *Biochem. J.* **2004,** *384*, 111-117.

24. Li, Y. J.; Zamble, D. B., *Chem. Rev.* **2009,** *109* (10), 4617-4643.

25. Ju, T. T.; Goldsmith, R. B.; Chai, S. C.; Maroney, M. J.; Pochapsky, S. S.; Pochapsky, T. C., *J. Mol. Biol.* **2006,** *363* (4), 523-534.

26. Dai, Y.; Wensink, P. C.; Abeles, R. H., *J. Biol. Chem.* **1999,** *274* (3), 1193-1195.

27. Dixon, N. E.; Gazzola, C.; Blakeley, R. L.; Zerner, B., *J. Am. Chem. Soc.* **1975,** *97* (14), 4131-4133.

28. Sumner, J. B., *J. Biol. Chem.* **1926,** *69* (2), 435-441.

29. Mobley, H. L. T.; Island, M. D.; Hausinger, R. P., *Microbiol. Rev.* **1995,** *59* (3), 451-480.

30. Follmer, C., *Phytochemistry* **2008,** *69* (1), 18-28.

31. Mulrooney, S. B.; Hausinger, R. P., *FEMS Microbiol. Rev.* **2003,** *27* (2-3), 239-261.

32. Brayman, T. G.; Hausinger, R. P., *J. Bacteriol.* **1996,** *178* (18), 5410-5416.

33. Colpas, G. J.; Brayman, T. G.; McCracken, J.; Pressler, M. A.; Babcock, G. T.; Ming, L. J.; Colangelo, C. M.; Scott, R. A.; Hausinger, R. P., *J. Biol. Inorg. Chem.* **1998,** *3* (2), 150-160.

34.   Colpas, G. J.; Brayman, T. G.; Ming, L. J.; Hausinger, R. P., *Biochemistry* **1999,** *38* (13), 4078-4088.

35.   Drennan, C. L.; Doukov, T. I.; Ragsdale, S. W., *J. Biol. Inorg. Chem.* **2004,** *9* (5), 511-515.

36.   Dobbek, H.; Svetlitchnyi, V.; Gremer, L.; Huber, R.; Meyer, O., *Science* **2001,** *293* (5533), 1281-1285.

37.   Dobbek, H.; Svetlitchnyi, V.; Liss, J.; Meyer, O., *J. Am. Chem. Soc.* **2004,** *126* (17), 5382-5387.

38.   Drennan, C. L.; Heo, J. Y.; Sintchak, M. D.; Schreiter, E.; Ludden, P. W., *Proc. Natl. Acad. Sci. U. S. A.* **2001,** *98* (21), 11973-11978.

39.   Ragsdale, S. W.; Kumar, M., *Chem. Rev.* **1996,** *96* (7), 2515-2539.

40.   Ragsdale, S. W.; Riordan, C. G., *J. Biol. Inorg. Chem.* **1996,** *1* (6), 489-493.

41.   Doukov, T. I.; Blasiak, L. C.; Seravalli, J.; Ragsdale, S. W.; Drennan, C. L., *Biochemistry* **2008,** *47* (11), 3474-3483.

42.   Bramlett, M. R.; Tan, X.; Lindahl, P. A., *J. Am. Chem. Soc.* **2003,** *125* (31), 9316-9317.

43.   Riordan, C. G., *J. Biol. Inorg. Chem.* **2004,** *9* (5), 542-549.

44.   Seravalli, J.; Xiao, Y.; Gu, W.; Cramer, S. P.; Antholine, W. E.; Krymov, V.; Gerfen, G. J.; Ragsdale, S. W., *Biochemistry* **2004,** *43* (13), 3944-3955.

45.   De Gioia, L.; Fantucci, P., *Inorg. Chim. Acta* **1998,** *273* (1-2), 379-387.

46.   Gu, W. W.; Gencic, S.; Cramer, S. P.; Grahame, D. A., *J. Am. Chem. Soc.* **2003,** *125* (50), 15343-15351.

47.   Helvenston, M. C.; Castro, C. E., *J. Am. Chem. Soc.* **1992,** *114* (22), 8490-8496.

48. Lahiri, G. K.; Schussel, L. J.; Stolzenberg, A. M., *Inorg. Chem.* **1992,** *31* (24), 4991-5000.

49. Ram, M. S.; Riordan, C. G., *J. Am. Chem. Soc.* **1995,** *117* (8), 2365-2366.

50. Ram, M. S.; Riordan, C. G.; Yap, G. P. A.; LiableSands, L.; Rheingold, A. L.; Marchaj, A.; Norton, J. R., *J. Am. Chem. Soc.* **1997,** *119* (7), 1648-1655.

51. Thauer, R. K., *Microbiol.-U. K.* **1998,** *144*, 2377-2406.

52. Ermler, U., *Dalton Trans.* **2005,** (21), 3451-3458.

53. Eschenmoser, A., *Ann. N. Y. Acad. Sci.* **1986,** *471*, 108-129.

54. Stephenson, M.; Stickland, L. H., *Biochem. J.* **1931,** *25* (1), 205-214.

55. Graf, E. G.; Thauer, R. K., *FEBS Lett.* **1981,** *136* (1), 165-169.

56. Lubitz, W.; Gastel, M. v.; Gärtner, W., Nickel Iron Hydrogenases. In *Nickel and Its Surprising Impact in Nature*, Sigel, A.; Sigel, H.; Sigel, R. K. O., Eds. John Wiley and Sons, Ltd.: West Sussex, England, 2007; Vol. 2, pp 279 - 322.

57. Volbeda, A.; Charon, M. H.; Piras, C.; Hatchikian, E. C.; Frey, M.; Fontecillacamps, J. C., *Nature* **1995,** *373* (6515), 580-587.

58. Happe, R. P.; Roseboom, W.; Pierik, A. J.; Albracht, S. P. J.; Bagley, K. A., *Nature* **1997,** *385* (6612), 126-126.

59. Cammack, R.; Frey, M.; Robson, R., *Hydrogen as a Fuel: Learning from Nature*. Taylor & Francis Ltd.: 2001; p 267 pp.

60. Bruschi, M.; Zampella, G.; Fantucci, P.; De Gioia, L., *Coord. Chem. Rev.* **2005,** *249* (15-16), 1620-1640.

61. Bryngelson, P. A.; Arobo, S. E.; Pinkham, J. L.; Cabelli, D. E.; Maroney, M. J., *J. Am. Chem. Soc.* **2003,** *126* (2), 460-461.

62. Barondeau, D. P.; Kassmann, C. J.; Bruns, C. K.; Tainer, J. A.; Getzoff, E. D., *Biochemistry* **2004,** *43* (25), 8038-8047.

63. Szilagyi, R. K.; Bryngelson, P. A.; Maroney, M. J.; Hedman, B.; Hodgson, K. O.; Solomon, E. I., *J. Am. Chem. Soc.* **2004,** *126* (10), 3018-3019.

64. Gale, E. M.; Simmonett, A. C.; Telser, J.; Schaefer, H. F.; Harrop, T. C., *Inorg. Chem.* **2011,** *50* (19), 9216-9218.

65. Herbst, R. W.; Guce, A.; Bryngelson, P. A.; Higgins, K. A.; Ryan, K. C.; Cabelli, D. E.; Garman, S. C.; Maroney, M. J., *Biochemistry* **2009,** *48* (15), 3354-3369.

66. Ma, H.; Chattopadhyay, S.; Petersen, J. L.; Jensen, M. P., *Inorg. Chem.* **2008,** *47* (18), 7966-7968.

67. Neupane, K. P.; Gearty, K.; Francis, A.; Shearer, J., *J. Am. Chem. Soc.* **2007,** *129* (47), 14605-14618.

68. Neupane, K. P.; Shearer, J., *Inorg. Chem.* **2006,** *45* (26), 10552-10566.

69. Schmidt, M.; Zahn, S.; Carella, M.; Ohlenschläger, O.; Görlach, M.; Kothe, E.; Weston, J., *ChemBioChem* **2008,** *9* (13), 2135-2146.

70. Shearer, J.; Long, L. M., *Inorg. Chem.* **2006,** *45* (6), 2358-2360.

71. Shearer, J.; Neupane, K. P.; Callan, P. E., *Inorg. Chem.* **2009,** *48* (22), 10560-10571.

72. Tietze, D.; Breitzke, H.; Imhof, D.; Kothe, E.; Weston, J.; Buntkowsky, G., *Chem.-Eur. J.* **2009,** *15* (2), 517-523.

73. Gale, E. M.; Cowart, D. M.; Scott, R. A.; Harrop, T. C., *Inorg. Chem.* **2011,** *50* (20), 10460-10471.

74. Johnson, O. E.; Ryan, K. C.; Maroney, M. J.; Brunold, T. C., *J. Biol. Inorg. Chem.* **2010,** *15* (5), 777-793.

75.   Pochapsky, T. C.; Pochapsky, S. S.; Ju, T. T.; Hoefler, C.; Liang, J., *J. Biomol. N. M. R.* **2006,** *34* (2), 117-127.

76.   Uudsemaa, M.; Tamm, T., *J. Phys. Chem. A* **2003,** *107* (46), 9997-10003.

77.   Bryngelson, P. A.; Maroney, M. J., Nickel Superoxide Dismutase. In *Nickel and Its Surprising Impact in Nature*, Sigel, A.; Sigel, H.; Sigel, R. K. O., Eds. John Wiley & Sons Ltd.: Chichester West Sussex, England, 2007; Vol. 2, pp 417 - 444.

78.   Chohan, B. S.; Maroney, M. J., *Inorg. Chem.* **2006,** *45* (5), 1906-1908.

79.   Farmer, P. J.; Solouki, T.; Mills, D. K.; Soma, T.; Russell, D. H.; Reibenspies, J. H.; Darensbourg, M. Y., *J. Am. Chem. Soc.* **1992,** *114* (12), 4601-4605.

80.   Kumar, M.; Colpas, G. J.; Day, R. O.; Maroney, M. J., *J. Am. Chem. Soc.* **1989,** *111* (21), 8323-8325.

81.   Kumar, M.; Day, R. O.; Colpas, G. J.; Maroney, M. J., *J. Am. Chem. Soc.* **1989,** *111* (15), 5974-5976.

82.   Maroney, M. J.; Choudhury, S. B.; Bryngelson, P. A.; Mirza, S. A.; Sherrod, M. J., *Inorg. Chem.* **1996,** *35* (4), 1073-1076.

83.   Mirza, S. A.; Pressler, M. A.; Kumar, M.; Day, R. O.; Maroney, M. J., *Inorg. Chem.* **1993,** *32* (6), 977-987.

84.   Grapperhaus, C. A.; Darensbourg, M. Y., *Acc. Chem. Res.* **1998,** *31* (8), 451-459.

Chapter 2: Computational and spectroscopic analysis of a nickel superoxide dismutase mimic

2.1 Acknowledgement

2.2 Introduction

Superoxide, $O_2^{.-}$, is a toxic radical byproduct of aerobic (O_2) metabolism that is produced from leakage out of the mitochondrial membrane.[4] The toxicity of superoxide is due largely to its ability to reduce biologically important metals including Fe^{III} and Cu^{II} and inactivate iron-sulfur clusters in proteins.[6] It also disrupts NO-mediated signaling, generating peroxynitrite, a very reactive species.[6] Because of this harmfulness, Nature has evolved superoxide dismutases, which are ubiquitous enzymes that catalyze the disproportionation of superoxide to H_2O_2 and O_2

(Equation 1). All known SODs require a redox-active metal ion center for reactivity, and four distinct classes of SODs have been characterized, including manganese (Mn-SOD), iron (Fe-SOD), copper/zinc (Cu/Zn-SOD), and nickel (Ni-SOD).

$$O_2^{-} + 2H^{+} \rightarrow O_2 + H_2O_2 \qquad (1)$$

Although the net reaction catalyzed is the same for all SOD enzymes, Ni-SOD does not share any sequence or structural homology with the other three classes of enzymes.[9] While Fe-, Mn- and Cu/Zn-SODs all employ O and N donors as ligands, derived from either amino acid side chains or solvent, Ni-SOD features thiolate ligands as well as backbone-derived deprotonated amide and N-terminal amine N ligands.[8, 10-12] Sulfur coordination in Ni-SOD is unique, given that thiolate ligands in metal complexes are known to be prone to oxidation by O_2 and its reduced derivatives.[13, 14] Figure 2.1 shows the active-site structures for the four classes of SOD enzymes.
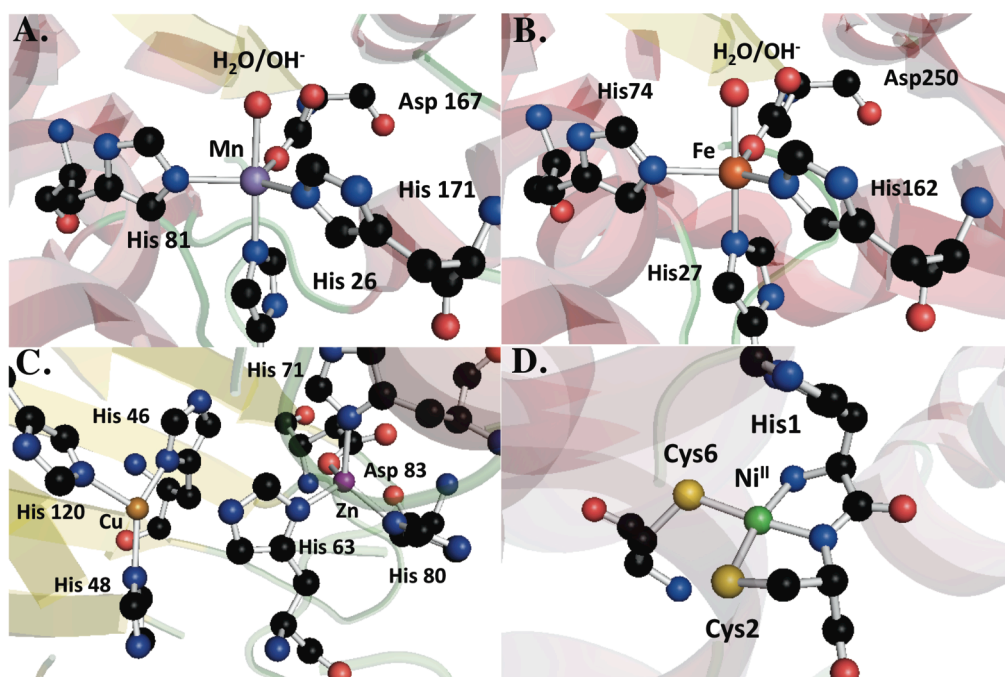
Figure 2.1 Active sites of Mn-SOD[1] (A), Fe-SOD[5] (B), Cu/Zn-SOD[7] (C) and Ni-SOD[8] (D).

During turnover, the geometry of the active-site metal in Ni-SOD switches from four-coordinate square planar 2N:2S to five-coordinate square pyramidal 3N:2S (See Figure 1.13). In the reduced form, the Ni^{II} ion is coordinated by the N-terminal amine of His1, the backbone amidate of Cys2, and the cysteinate sulfur atoms of Cys2 and Cys6.[3, 8, 15] Upon oxidation, the side chain of His1 swings down and binds as the fifth ligand to the Ni^{III} ion. Whether substrate binds directly to the metal center during turnover, via an inner sphere mechanism, or if outer sphere interactions allow for superoxide dismutation, is one of the key questions regarding the mechanism of Ni-SOD. Recent reports support direct interactions between substrate and nickel.[16, 17] In the past few years, studies have revealed more about the role of the secondary coordination sphere, although the mechanism of Ni-SOD has yet to be fully elucidated.[18-20] Because all of the metal-binding atoms are located within the first six residues of Ni-SOD, small peptide "maquettes" derived from the sequence of the enzyme have been employed to characterize the minimal functional unit necessary to facilitate chemistry.[16, 17, 21-23] Although these models are able to consume superoxide, none approach the near diffusion-limited activity of the enzyme, which is not surprising given the minimal structure and lack of surrounding protein in the mimics. [24] In addition, some synthetic 2N:2S models have been developed, but the Ni^{III} state is inaccessible and therefore renders the molecules inactive as functional mimics of the protein.[25-27]

The nickel complex of the metal-binding tripeptide asparagine-cysteine-cysteine, ([Ni-NCC]$^{2-}$; Ni-NCC) is both a structural and functional mimic of Ni-SOD. (Jennifer Ann Stowell Laurence, Anthony Andrew Vartia, Mary Elizabeth Krause. METAL ABSTRACTION PEPTIDE (MAP) TAG AND ASSOCIATED METHODS. Provisional Patent Application USPTO 61/052,918. Filed May 13, 2008. International Patent Application PCT/US2009/43821.

Filed May 13, 2009. Published September 10, 2010.) Ni-NCC is distinct from other peptide mimics of Ni-SOD in that it is not derived from the sequence of the parent enzyme. In the metal-binding sequence of Ni-SOD, there is no asparagine residue and the two Cys amino acids are not adjacent. Prior to this work, it was unknown how the peptide binds to the Ni^{II} center in Ni-NCC. Therefore, a combined spectroscopic and computational approach was applied to determine the structure of the complex.

2.3 Experimental

2.3.1. Generation of Ni-NCC complex. The NCC peptide was purchased from Genscript Corporation (Piscatway, NJ, USA). The Ni-NCC complex was generated by incubating the peptide for approximately 30 minutes with immobilized metal affinity chromatography (IMAC) resin (GE Healthcare) charged with nickel in aqueous solution at neutral to basic pH. This reaction yields a reddish-brown complex.

2.3.2. Electrospray ionization mass spectrometry (ESI-MS). Mass spectrometric analysis was performed by M. Krause. Samples were diluted 100x in methanol and analyzed on an LCT Premier (Waters Corporation) operating in negative ion mode. In order to verify that no changes were made to the peptide upon release of the metal, samples were acidified to approximately pH 5 by addition of 1 M hydrochloric acid (HCl) and analyzed using the same technique.

2.3.3. CD and electronic absorption spectroscopy. A 1.5 mM solution of Ni-NCC was prepared in 50 mM sodium phosphate, pH 7.4, purged with Ar. Immediately after incubation, samples were placed in a cuvette with a 1-cm path length and scanned from 900-300 nm using both absorption and CD spectroscopy. Background scans of buffer alone were subtracted from

each scan. Electronic absorption studies were performed on an Agilent 8453 UV/Visible spectrophotometer. Circular dichroism analysis was performed on a J-815 (Jasco Corporation). The CD data presented are the average of five scans.

2.3.4. Density Functional Theory (DFT). The ORCA 2.7 software package designed by Neese and coworkers was used for all DFT computations.[28] Spin restricted (RKS) geometry optimizations were converged to the $S = 0$ spin state and employed the Becke-Perdew (BP86) functional, and the aug-TZVP (Dunning diffuse functions added to Ahlrichs triple-ξ valence polarized) basis in conjunction with the TZV/J auxiliary basis for all atoms.[29-32] These calculations employed the resolution of identity (RI) approximation developed by Neese.[33] Solvation effects associated with water (dielectric constant, ε = 80) were incorporated using the conductor like screening model (COSMO), as implemented in ORCA.[34] Subsequent single-point and time-dependent DFT (TD-DFT) energy calculations on the geometry-optimized structures employed the B3LYP functional, the aug-TZVP basis, and the COSMO solvation model.[35-37]

2.3.5. Magnetic Circular Dichroism (MCD) Spectroscopy. Samples containing 6 mM Ni-NCC were prepared in 50 mM sodium borate at pH 10, purged with argon. Solid sucrose was added as a glassing agent and the mixture was heated to form a saturated solution. The dilution resulted in a final Ni-NCC concentration of 2 mM. The sample was placed in an MCD cell and flash frozen. Spectra were collected on a J-815 (Jasco Corporation) interfaced with an Oxford Spectromag 4000. Spectra were collected at +7 and -7 Tesla and the difference was found via subtraction in order to remove any CD signal. Spectra were collected at 15 K, 8 K, 4.5 K, and 2 K and analyzed to identify any changes in the spectra that indicate paramagnetic character. The feasibility of correlating these low temperature data with the structure of Ni-NCC at room temperature is demonstrated by the lack of apparent changes in the corresponding CD spectra

collected at 298 and 4.5 K.

2.3.6. Electrochemical studies. Electrochemical analysis was performed by M. Krause. A 3-mL, 3-mM Ni-NCC sample was prepared in 50 mM sodium borate at pH 10. Cyclic voltammetry (CV) data were collected with a CHI812C Electrochemical Analyzer potentiostat (CH Instruments) with a three-electrode setup (platinum working electrode, Bioanalytical Systems Inc.; Pt auxiliary electrode; Ag/AgCl reference electrode) in a glass CV cell. Potential was applied from zero to 1.2 V with a scan rate of 0.2 V per second, and current was measured. Bulk electrolysis was performed on a 3-mL, 3-mM Ni-NCC sample prepared in the same manner. Using the same setup as the CV measurements, potential was applied at 0.95 V while stirring to fully oxidize the sample, and current was monitored until no further change was observed. ESI-MS operating in negative ion mode was performed on the sample following bulk electrolysis to confirm the peptide was unaltered.

2.3.7. Xanthine/xanthine oxidase SOD activity assay. An assay using xanthine/xanthine oxidase was performed as described by Crapo et al. with minor modifications.[43] The assay was performed in 50 mM potassium phosphate with 100 μM EDTA at pH 7.8. In this assay, 600 μM cytochrome c from bovine heart (Sigma), 300 μM xanthine (Sigma), and enough xanthine oxidase (from buttermilk; Sigma) to cause a change in absorbance at 550 nm of 0.02 AU to 0.04 AU per minute were added to a final volume of 300 μL, and the change in absorbance at 550 nm was monitored on a Cary 100 UV-visible spectrophotometer (Varian). The assay was performed with several concentrations (0, 10, 15, 20, 25, 30, 35, 40, 50 μM and beyond as necessary) of Ni-NCC to measure an IC_{50} value.

2.4. Results and Discussion

Attempts to generate diffraction-quality crystals of Ni-NCC have been unsuccessful, and therefore characterization of the complex by standard X-ray diffraction (XRD) methods has not been possible. However, electronic absorption, circular dichroism (CD), and variable-temperature magnetic CD (MCD) data were collected for Ni-NCC to provide insight into the Ni^{II} geometry in the complex.

Although electronic absorption, CD and MCD analyses all probe electronic structure, differences in the selection rules make the techniques complementary and together they help generate a more complete structure description.[38] For electronic absorption, transitions must be both spin- and electric dipole-allowed. This makes pure $d \rightarrow d$ transitions electronic absorption forbidden, given that all d orbitals have the same symmetry with respect to inversion. However, the transitions can gain intensity from vibronic coupling, spin-orbit coupling, or mixing of states. In CD, the allowed transition must be both electric- and magnetic dipole-allowed. Thus, additional information about the transition can be gained using CD along with electronic absorption. In addition, the positive and negative ellipticity bands in CD can help resolve broad features observed in electronic absorption spectroscopy. MCD C-terms require two perpendicular transition moments for allowed transitions, and this is usually only met in low-symmetry metal complexes like Ni-NCC with spin-orbit coupling of excited states. Because this coupling is most effective among ligand field excited states, this selectively enhances $d \rightarrow d$ transitions relative to ligand charge transfer transitions and is therefore useful for inorganic characterization.

NCC binds nickel, apparently with extremely high affinity at physiological pH. To show the extent of incorporation of metal into the complex and assess changes in protonation of the

free versus bound peptide, electrospray ionization mass spectrometry (ESI-MS) operating in negative ion mode was used. The data show full incorporation of the metal in a 1:1 ratio and suggest that no irreversible modifications to the peptide occur upon incorporation or release of the metal via acidification. These data further indicate a tetra-deprotonated species binds the

Table 2.1. Gaussian deconvoluted energies from electronic absorption and CD spectra of Ni-NCC generated in 50 mM potassium phosphate buffer.

Band	Electronic Absorption		CD	
	Energy (cm^{-1})	ε ($M^{-1}cm^{-1}$)	Energy (cm^{-1})	$\Delta\varepsilon$ ($M^{-1}cm^{-1}$)
1	14 500	20	14 200	-0.1
2	17 300	60	16 270	-0.21
3	19 650	160	18 900	0.22
4	21 850	205	22 170	0.64
5	24 300	275	23 900	-0.44
6	26 850	575	26 520	0.71
7	28 850	1080	28 475	1.1

metal ion (Ni-NCC = 392.98 *m/z*).

An iterative deconvolution of the absorption and CD spectra reveal seven electronic transitions between 14 000 and 29 000 cm^{-1} (Table 2.1 and Figure 2.2). With the exception of band 1, the energies of these transitions are within ~1000 to 2000 cm^{-1} of those reported for Ni-SOD (Table 2.2), which is indicative of structural similarities between the Ni^{II} centers in these two systems.[2] Bands 1 – 4 of Ni-NCC, which are relatively intense in the CD spectrum but carry only moderate absorption intensities, are assigned as the four *d-d* transitions expected for a

Table 2.2. Comparison of band assignments and transition energies for Ni-NCC and Ni-SOD.[2]

Band	Transition Assignment	Ni-NCC (cm^{-1})	Ni-SOD (cm^{-1})
1	Ni^{II} *d-d*	14 200	17 110
2	Ni^{II} *d-d*	16 270	18 430
3	Ni^{II} *d-d*	18 900	20 500
4	Ni^{II} *d-d*	22 170	22 240
5	S^- - Ni^{II} CT	23 900	24 970
6	S^- - Ni^{II} CT	26 520	27 650
7	S^- - Ni^{II} CT	28 475	29 220
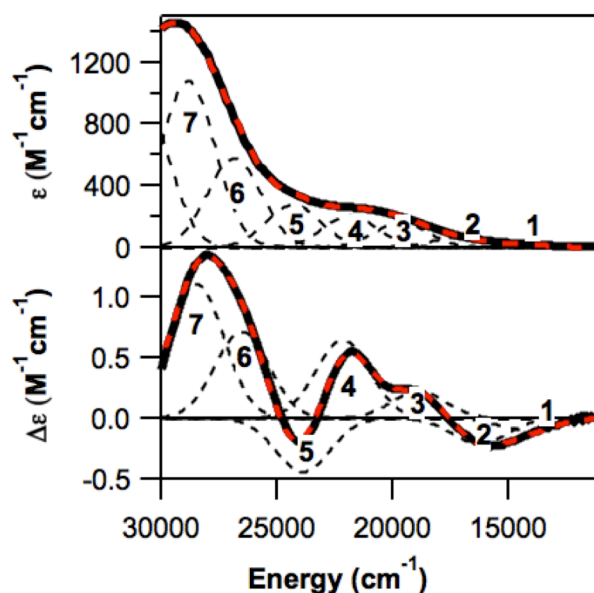
Figure 2.2. Deconvoluted absorption (top) and CD (bottom) spectra of Ni-NCC generated in 50 mM potassium phosphate buffer. Experimental spectra (black), individual deconvoluted Gaussian bands (dash), and the sum of Gaussian deconvoluted bands (red dash) are shown.

square planar Ni^{II} center. By analogy to Ni-SOD, we assign the higher-energy bands 5 – 7 as

thiolate-to-nickel(II) charge transfer (CT) transitions.

Further support for the presence of a square planar Ni^{II} center in Ni-NCC comes from the

low intensity temperature-dependent MCD signals observed for Ni-NCC over the temperature

range 2 – 15 K (Figure 2.3.). Three terms contribute to MCD intensity, but only the *C*-term is

temperature dependent. *C*-term contributions arise from a degenerate ground state, which

originates from spin degeneracy. Therefore, only a paramagnetic species will have *C*-term MCD

behavior. Thus, the low intensity of the temperature-dependent MCD signals of Ni^{II}-NCC is

indicative of a diamagnetic ($S = 0$) species, which is best rationalized in terms of a square planar

Ni^{II} center where all of the *d* orbitals except for the LUMO $d_{x^2-y^2}$ would be doubly-occupied. In

addition, room temperature (~298 K) and low temperature (4.5 K) CD spectra are similar (Figure

2.4). The only changes between the two spectra are the expected blue shifts and sharpening of
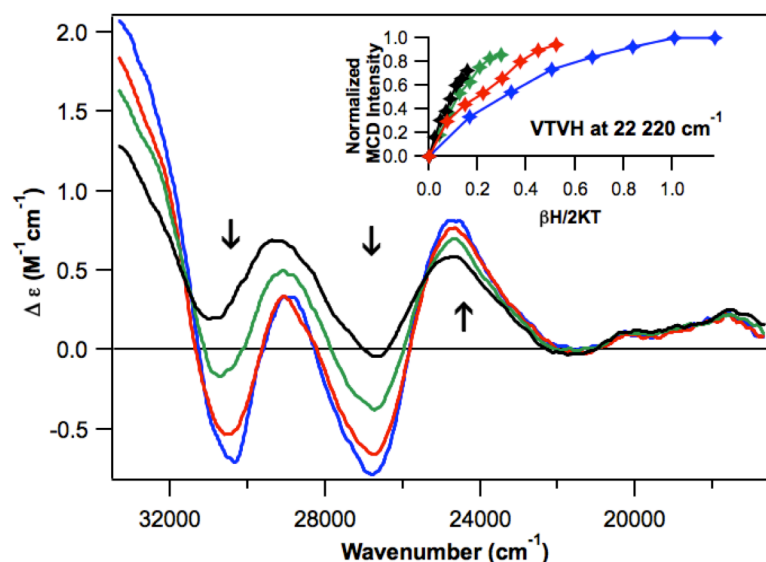
Figure 2.3. Variable-temperature, 7 T MCD difference spectra of Ni-NCC generated in a 1:2 solution of 50 mM sodium borate: sucrose. Spectra were collected at 2 K (blue), 4.5 K (red), 8 K (green), and 15 K (black). The inset shows the variable temperature, variable field (VTVH) plot for the band at 22 220 cm^{-1}, which shows that the minor paramagnetic component is $S > \frac{1}{2}$.

the bands in the spectrum collected at 4.5 K. A minor paramagnetic component ($S > \frac{1}{2}$) is

observed that represents less than 1% of the sample (Figure 2.3, inset), which is consistent with a

tetrahedral Ni^{II} species. This percentage was determined by comparing

the MCD intensity (in $\Delta\varepsilon$, M^{-1}cm^{-1}) of the most intense feature in our spectrum to a purely
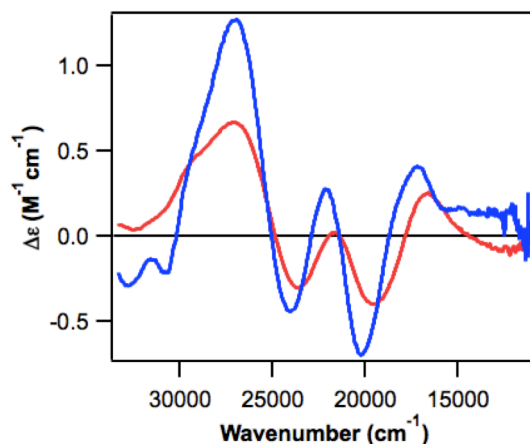
Figure 2.4. CD spectra of Ni-NCC collected at 298 K (red) and 4.5 K (blue). Sample is in 1:2 solution of 50 mM sodium borate: sucrose.

38

paramagnetic Ni^{II} species, Ni^{II}-rubredoxin, at comparable field (5T) and temperature (4.5 K).[39] In comparison, in the tetrahedral Ni^{II}-substituted rubredoxin MCD spectrum, the most intense feature at 23 000 cm^{-1} has an intensity of > 100 $M^{-1}cm^{-1}$. Therefore, under the assumption that the paramagnetic species observed from Ni-NCC has a similar $\Delta\varepsilon$ value, this species represents approximately less than 1% of the overall sample.

Based on the data presented above, nickel is coordinated in a square planar 2N:2S geometry in Ni-NCC. In Ni-SOD, the thiolate ligands are *cis* and the nitrogen ligands include one amine and one amide.[2] Our current studies support a possible arrangement that parallels the coordination by Ni-SOD in which the two sulfur ligands are arranged *cis* and one nitrogen is derived from a backbone amide while the second is from the N-terminal amine.

DFT computations were performed in order to determine the most energetically favorable arrangement of NCC about the metal center, and therefore establish the specific atoms coordinated to the nickel. In addition, TD-DFT was employed to assist in the analysis of the spectroscopic data of Ni-NCC and to allow for the evaluation and comparison to the various 2N:2S arrangements of Ni-NCC. However, prior to analysis of the Ni-NCC system, DFT and TD-DFT analysis was performed on a set of 2N:2S square planar Ni^{II} model complexes with published crystal structures and electronic absorption spectra. This analysis was performed in order to ensure that our method correctly predicts the geometric and electronic structures of characterized complexes.

The Ni^{II} complexes of N,N′-ethylenebis(2-mercaptoacetamide) (H_4ema)[40] and N,N′-dimethyl-N,N′-bis(2-mercaptoethyl)-1,3-propanediamine (N_2S_2)[41] were used to generate the models ([Ni^{II}(ema)]$^{2-}$; Ni^{II}-ema) and Ni^{II}-N_2S_2 respectively. The models were chosen for their *bis*amide (Ni^{II}-ema) and *bis*amine (Ni^{II}-N_2S_2) nitrogen coordination environments (Figure 2.5).
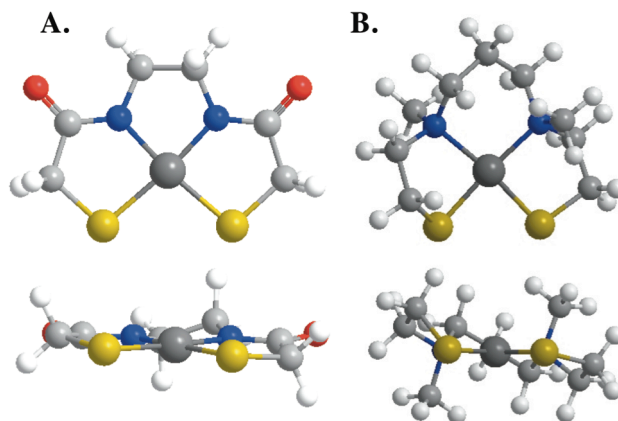
Figure 2.5. DFT-optimized structures of A, *bis*amide Ni^{II}-ema and B, *bis*amine Ni^{II}-N_2S_2. Both complexes feature a Ni^{II} coordinated in a 2N:2S square plane.

Table 2.3 shows the results of the Ni^{II}-ema and Ni^{II}-N_2S_2 computations. The DFT-predicted bond distances are overestimated when compared with the experimental XRD data, especially for the Ni-N bonds in the *bis*-amide complex. In addition, most of the transition energies are shifted to lower energy in the TD-DFT computations when compared to experimental electronic absorption spectra.[40, 41]. The anionic thiolate bound to the nickel is computationally challenging for DFT to analyze and systematically DFT calculates Ni-S bonds that are too long. These longer bonds artificially stabilize the acceptor LUMO orbital, Ni $d_{x^2-y^2}$ for these square planar Ni^{II} complexes. Therefore, the longer predicted bond distances lead to erroneously low *d-d* transition energies. Indeed, it has been reported that DFT overestimates bond distances for similar Ni-SOD peptide mimics.[42] Therefore, our computational method can be used to analyze Ni-NCC, for which there is no crystal structure.

Table 2.3. Comparing DFT results to experimental values for Ni^{II}-ema and Ni^{II}-N_2S_2.

	Ni^{II}-ema (bisamide)				Ni^{II}-N$_2$S$_2$ (bisamine)			
Parameter	**Experimental**		**DFT**		**Experimental**		**DFT**	
Ni-N (Å)	1.857		1.874		1.999 2.006		2.025 2.069	
Ni-S (Å)	2.179		2.223		2.174 2.176		2.194 2.179	
λmax (nm)	552	437	650	450	600	480	620	480
ε (M^{-1}cm^{-1})	80	300	10	450	10	100	75	25

Table 2.4 shows the relative single-point energies of four potential arrangements of the NCC ligand about the Ni^{II} center. These were developed based on the predicted square planar, 2N:2S geometry about the metal center. The *cis*-proximal geometry, where the Ni^{II} is coordinated by the N-terminal amine from Asn1, the deprotonated amidate nitrogen from Cys2, and the two deprotonated cysteinate sulfur atoms of Cy2 and Cys3, is the lowest energy form and is nearly 10 kcal/mol lower in energy than the *trans*-mixed complex.

As we predicted, the lowest energy conformation of Ni-NCC features a Ni^{II} with ligands
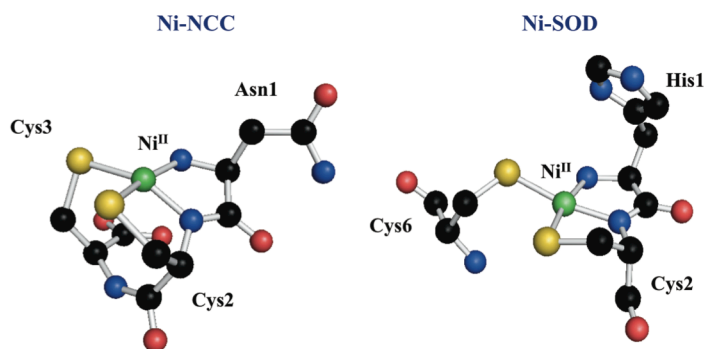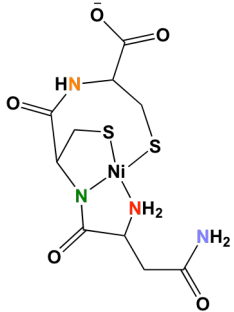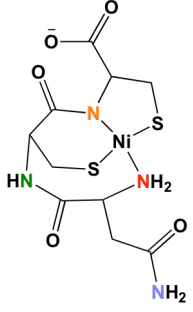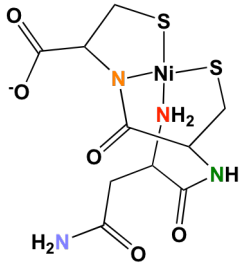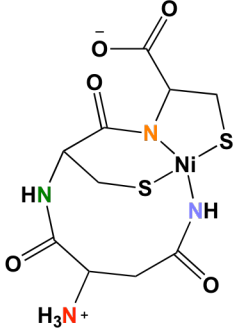
Figure 2.6. Proposed metal coordination in Ni^{II}-NCC (left) and metal coordination in Ni^{II}-SOD.[3]

identical to the first coordination sphere of the metal in Ni^{II}-SOD. Figure 2.6 shows the geometries about the metal centers in Ni-NCC and Ni^{II}-SOD and Table 2.4 shows the energies and geometries of the four models explored.

Table 2.4. Energies of converged structures of Ni-NCC in various conformations. The lowest energy conformation corresponds to Ni-NCC with *cis*-thiolates and the backbone amide and N-terminal amine nitrogens involved in coordination. Relative energies versus the lowest energy model (*cis*-proximal) are listed in kcal/mol. Nitrogen atoms are color coded to be consistent between models.

The Gaussian deconvoluted *d-d* transition energies from the experimental electronic absorption and CD spectra of Ni-NCC, along with the TD-DFT computed *d-d* transition energies for the various arrangements of the NCC ligand about Ni^{II} are given in Table 2.5. The

experimental electronic absorption spectrum of Ni-NCC together with the predicted spectra of the various conformations of Ni-NCC are shown in Figure 2.7. As discussed above, DFT systematically predicts the Ni-S bond distances to be too long. This elongation makes the causes a systematic decrease in energy of all of the predicted d-d transition energies when compared to the experimental data. With this in mind, comparison of the experimental to the predicted d-d transition energies for the various geometric arrangements of NCC around Ni[II] in Ni-NCC shows that the *cis*-proximal arrangement is likely the most reasonable geometry. Three of the four predicted transitions in the *cis*-proximal model are within 1000 cm^{-1} of the experimental values. For the *cis*-distal model, although all of the transitions are red-shifted, they are shifted more significantly than in the cis-proximal model. For the trans-mixed and bis-amide models, there is not systematic shifting, as some of the bands are shifted by less than 2000 cm^{-1} and others by nearly 4000 cm^{-1}. On the basis of the d-d transition energies, these data show that *cis*-proximal Ni-NCC is the likely arrangement of the ligand in the complex.

Table 2.5. Experimental Gaussian-deconvoluted d-d transition energies (in cm^{-1}) for Ni-NCC and TD-DFT predicted d-d transition energies (in cm^{-1}) for various ligand arrangements of Ni-NCC.

Experimental	*bis*-amide	*cis*-distal	*cis*-proximal	*trans*-mixed
14 200	14 470	11 300	14 500	15 200
16 270	15 100	12 800	15 600	17 800
18 900	15 800	14 000	17 000	18 200
22 170	18 400	16 100	19 300	21 000
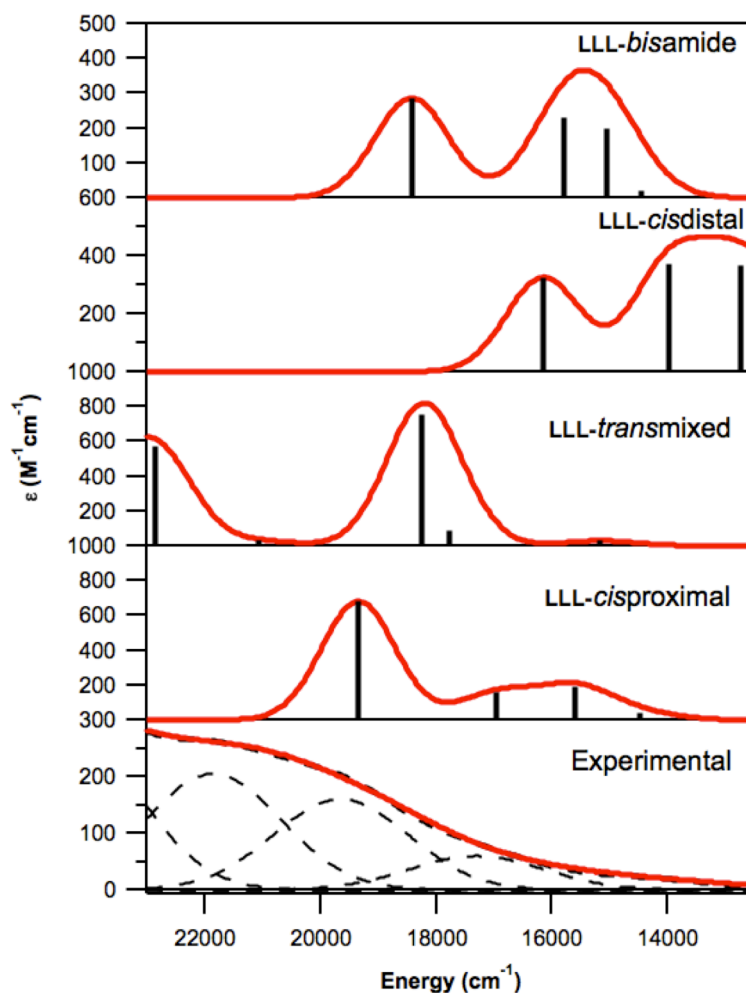
Figure 2.7. Gaussian deconvoluted electronic absorption spectrum of Ni-NCC compared to TD-DFT-predicted electronic absorption spectra of *bis*-amide, *cis*-distal, *trans*-mixed and *cis*-proximal Ni-NCC.

Because the studies above demonstrate that Ni-NCC serves as a reasonable structural mimic of Ni-SOD, the midpoint potential of Ni-NCC was measured using cyclic voltammetry (CV). CV data show electron transfer is partially reversible, with a midpoint potential of 0.72(2) V versus Ag/AgCl (Figure 2.7), which is similar to the 0.70(2) V measured for a peptide mimic based on the sequence of the parent SOD enzyme with mixed amine/amide coordination and *cis* ligation ([Ni(SOD^{M1}]).[22] Ni-SOD has a midpoint potential of 0.290 V (NHE, 0.093 versus Ag/AgCl).[19] The partial-reversibility of the CV data indicate structural changes upon

oxidation/reduction, which is rationalized in terms of the different geometries preferred by Ni^{II} and Ni^{III} centers.
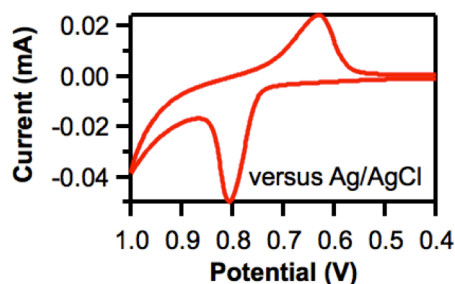
Figure 2.8. CV of Ni-NCC in 50 mM sodium borate, pH 9.3, with a scan rate of 0.2 V per second. E_m = 0.72(2) versus Ag/AgCl

To confirm that electron transfer does not alter the peptide and the measured potential specifically reflects a change at the nickel ion, ESI-MS was collected after performing bulk electrolysis. The mass is the same before and after undergoing oxidation, implying the peptide is unaltered. Therefore, the redox potential measured corresponds to the $Ni^{II/III}$ redox couple. Because the midpoint potential of the Ni-NCC complex falls between the reduction and oxidation potentials for superoxide, the ability of Ni-NCC to disproportionate the reactive superoxide species was examined.

A standard SOD activity assay using xanthine oxidase was performed.[43,44] Results of the assay are reported as IC_{50} values because the assay only measures the consumption of superoxide. The data show that Ni-NCC does exhibit SOD activity, but it is slower at consuming superoxide than Ni-SOD (IC_{50} = 4 × 10^{-5} M).[8] The IC_{50} for Ni-NCC (4.1 ± 0.8 × 10^{-5} M) is comparable to those values reported for other peptide mimics.[42] However, not surprisingly, the

value is significantly lower for Ni-SOD itself ($IC_{50} = 4.0 \times 10^{-8}$ M) which approaches the limits of diffusion and has the whole protein matrix to facilitate reactivity at the active-site nickel.[8]

Because the reduction potential of Ni-NCC is similar to that of [Ni(SOD^{M1}], but the activity of Ni-NCC is lower than this amine/amide maquette (2.1×10^{-7} M), the rate may be decreased by the absence of a fifth ligand in the Ni-NCC complex. For Ni-SOD, it has been suggested that the axial imidazole ligand tunes the redox properties of the Ni^{III} species to be appropriate for superoxide disproportionation.[2, 21] Therefore, the absence of a fifth ligand bound to the nickel center in Ni-NCC may account for the difference in reduction potential between Ni-NCC and Ni-SOD.

2.4. Conclusions.

`   Ni-NCC exhibits similar features to Ni-SOD, and its midpoint potential and ability to break down superoxide support its use as a mimic of the enzyme. The sequence of this novel peptide mimic is unrelated to that of Ni-SOD and provides a complementary system for understanding how the identity and geometry of the supporting ligands influence not only the reduction potential but functional electron transport.

2.5. References.

1.   Edwards, R. A.; Baker, H. M.; Whittaker, M. M.; Whittaker, J. W.; Jameson, G. B.; Baker, E. N., *J. Biol. Inorg. Chem.* **1998,** *3* (2), 161-171.

2.   Fiedler, A. T.; Bryngelson, P. A.; Maroney, M. J.; Brunold, T. C., *J. Am. Chem. Soc.* **2005,** *127* (15), 5449-5462.

3.   Bryngelson, P. A.; Arobo, S. E.; Pinkham, J. L.; Cabelli, D. E.; Maroney, M. J., *J. Am. Chem. Soc.* **2003,** *126* (2), 460-461.

4.   Valentine, J. S., Superoxide Dismutases and Reductases. In *Biological Inorganic Chemistry: Structure and Reactivity*, Bertini, I.; Gray, H. B.; Stiefel, E. I.; Valentine, J. S., Eds. University Science Books: Sausalito, California, 2007; pp 331 - 353.

5.   Pedersen, H. L.; Willassen, N. P.; Leiros, I., *Acta Crystallographica Section F-Structural Biology and Crystallization Communications* **2009,** *65*, 84-92.

6.   Valentine, J. S.; Wertz, D. L.; Lyons, T. J.; Liou, L. L.; Goto, J. J.; Gralla, E. B., *Curr. Opin. Chem. Biol.* **1998,** *2* (2), 253-262.

7.   Ogihara, N. L.; Parge, H. E.; Hart, P. J.; Weiss, M. S.; Goto, J. J.; Crane, B. R.; Tsang, J.; Slater, K.; Roe, J. A.; Valentine, J. S.; Eisenberg, D.; Tainer, J. A., *Biochemistry* **1996,** *35* (7), 2316-2321.

8.   Barondeau, D. P.; Kassmann, C. J.; Bruns, C. K.; Tainer, J. A.; Getzoff, E. D., *Biochemistry* **2004,** *43* (25), 8038-8047.

9.   Youn, H. D.; Kim, E. J.; Roe, J. H.; Hah, Y. C.; Kang, S. O., *Biochem. J.* **1996,** *318*, 889-896.

10.   Borgstahl, G. E. O.; Pokross, M.; Chehab, R.; Sekher, A.; Snell, E. H., *J. Mol. Biol.* **2000,** *296* (4), 951-959.

11.   Kerfeld, C. A.; Yoshida, S.; Tran, K. T.; Yeates, T. O.; Cascio, D.; Bottin, H.; Berthomieu, C.; Sugiura, M.; Boussac, A., *J. Biol. Inorg. Chem.* **2003,** *8* (7), 707-714.

12.   Strange, R. W.; Antonyuk, S.; Hough, M. A.; Doucette, P. A.; Rodriguez, J. A.; Hart, P. J.; Hayward, L. J.; Valentine, J. S.; Hasnain, S. S., *J. Mol. Biol.* **2003,** *328* (4), 877-891.

13.   Grapperhaus, C. A.; Darensbourg, M. Y., *Acc. Chem. Res.* **1998,** *31* (8), 451-459.

14. Mirza, S. A.; Pressler, M. A.; Kumar, M.; Day, R. O.; Maroney, M. J., *Inorg. Chem.* **1993,** *32* (6), 977-987.

15. Wuerges, J.; Lee, J. W.; Yim, Y. I.; Yim, H. S.; Kang, S. O.; Carugo, K. D., *Proc. Natl. Acad. Sci. U. S. A.* **2004,** *101* (23), 8569-8574.

16. Schmidt, M.; Zahn, S.; Carella, M.; Ohlenschläger, O.; Görlach, M.; Kothe, E.; Weston, J., *ChemBioChem* **2008,** *9* (13), 2135-2146.

17. Tietze, D.; Breitzke, H.; Imhof, D.; Kothe, E.; Weston, J.; Buntkowsky, G., *Chem.-Eur. J.* **2009,** *15* (2), 517-523.

18. Gale, E. M.; Narendrapurapu, B. S.; Simmonett, A. C.; Schaefer, H. F.; Harrop, T. C., *Inorg. Chem.* **2010,** *49* (15), 7080-7096.

19. Herbst, R. W.; Guce, A.; Bryngelson, P. A.; Higgins, K. A.; Ryan, K. C.; Cabelli, D. E.; Garman, S. C.; Maroney, M. J., *Biochemistry* **2009,** *48* (15), 3354-3369.

20. Shearer, J.; Neupane, K. P.; Callan, P. E., *Inorg. Chem.* **2009,** *48* (22), 10560-10571.

21. Neupane, K. P.; Gearty, K.; Francis, A.; Shearer, J., *J. Am. Chem. Soc.* **2007,** *129* (47), 14605-14618.

22. Shearer, J.; Long, L. M., *Inorg. Chem.* **2006,** *45* (6), 2358-2360.

23. Tietze, D.; Voigt, S.; Mollenhauer, D.; Tischler, M.; Imhof, D.; Gutmann, T.; Gonzalez, L.; Ohlenschlager, O.; Breitzke, H.; Gorlach, M.; Buntkowsky, G., *Angew. Chem., Int. Ed.* **2011,** *50* (13), 2946-2950.

24. Bryngelson, P. A.; Maroney, M. J., Nickel Superoxide Dismutase. In *Nickel and Its Surprising Impact in Nature*, Sigel, A.; Sigel, H.; Sigel, R. K. O., Eds. John Wiley & Sons Ltd.: Chichester West Sussex, England, 2007; Vol. 2, pp 417 - 444.

25. Ma, H.; Chattopadhyay, S.; Petersen, J. L.; Jensen, M. P., *Inorg. Chem.* **2008,** *47* (18), 7966-7968.

26. Shearer, J.; Zhao, N., *Inorg. Chem.* **2006,** *45* (24), 9637-9639.

27. Stibrany, R. T.; Fox, S.; Bharadwaj, P. K.; Schugar, H. J.; Potenza, J. A., *Inorg. Chem.* **2005,** *44* (23), 8234-8242.

28. Neese, F. *ORCA - an ab initio, Density Functional and Semiempirical Program Package*, 2.7; University of Bonn, 2009.

29. Becke, A. D., *J. Chem. Phys.* **1986,** *84* (8), 4524-4529.

30. Perdew, J. P., *Phys. Rev. B.* **1986,** *33* (12), 8822-8824.

31. Schafer, A.; Horn, H.; Ahlrichs, R., *J. Chem. Phys.* **1992,** *97* (4), 2571-2577.

32. Schafer, A.; Huber, C.; Ahlrichs, R., *J. Chem. Phys.* **1994,** *100* (8), 5829-5835.

33. Neese, F., *J. Comput. Chem.* **2003,** *24* (14), 1740-1747.

34. Sinnecker, S.; Rajendran, A.; Klamt, A.; Diedenhofen, M.; Neese, F., *J. Phys. Chem. A* **2006,** *110* (6), 2235-2245.

35. Becke, A. D., *J. Chem. Phys.* **1993,** *98* (7), 5648-5652.

36. Becke, A. D., *J. Chem. Phys.* **1993,** *98* (2), 1372-1377.

37. Dunning, T. H., *J. Chem. Phys.* **1989,** *90* (2), 1007-1023.

38. Solomon, E. I.; Hanson, M. A., Bioinorganic Spectroscopy. In *Inorganic Structure and Spectroscopy*, Solomon, E. I.; Lever, A. P. B., Eds. Wiley: New York, Vol. II, pp 1 - 129.

39. Kowal, A. T.; Zambrano, I. C.; Moura, I.; Moura, J. J. G.; LeGall, J.; Johnson, M. K., *Inorg. Chem.* **1988,** *27* (7), 1162-1166.

40. Kruger, H. J.; Peng, G.; Holm, R. H., *Inorg. Chem.* **1991,** *30* (4), 734-742.

41.   Colpas, G. J.; Kumar, M.; Day, R. O.; Maroney, M. J., *Inorg. Chem.* **1990,** *29* (23), 4779-4788.

42.   Neupane, K. P.; Shearer, J., *Inorg. Chem.* **2006,** *45* (26), 10552-10566.

43.   Crapo, J. D.; McCord, J. M.; Fridovich, I., [41] Preparation and assay of superoxide dismutases. In *Methods in Enzymology*, Sidney, F.; Lester, P., Eds. Academic Press: 1978; Vol. Volume 53, pp 382-393.

44.   Tabbì, G.; Driessen, W. L.; Reedijk, J.; Bonomo, R. P.; Veldman, N.; Spek, A. L., *Inorg. Chem.* **1997,** *36* (6), 1168-1175.

Chapter 3: Characterizing the structural rearrangement of Ni-NCC

Reproduced, in part, with permission from:

3.1 Acknowledgement

Because of the collaborative nature of this project, M. Krause made significant contributions to the work presented here. M. Krause performed the mass spectrometric experiments and did most of the electronic absorption and CD data collection, including all of the analysis with the D-containing peptides. In addition, her deuterium exchange work defined the number of sites that undergo chiral inversion in Ni-NCC and Ni-GCC. Furthermore, the rearrangement of Ni-NCC over the course of 24 hours in phosphate buffer to generate an exposed nickel center was supported by her infrared spectroscopy (IR) studies.

3.2 Introduction.

A molecule's three-dimensional shape and its physiological or chemical function are closely linked by the so-called structure-function relationship.[1] It is well known that molecules with the same chemical makeup, but different connectivity, three-dimensional orientation, or chirality, have different biological activities. Perhaps the most infamous example of this is the thalidomide tragedy of the 1950's and 60's. One enantiomer of the drug had sedative effects and was therefore a morning sickness preventative for pregnant women, while the other is a teratogen and caused children of the women who took the drug to be born with severe birth defects.[2]

In addition to many synthetic molecules, biological polymers are also chiral. Although it was originally thought that only the L-form of amino acids and D-form of sugars are employed in biology, the advancement of analytical methods has proven that both chiral forms of the building blocks of the polymers are found in Nature.[3] Initially discovered in bacteria and plants, D-amino acids have also been found in mammals including humans.[4]

Racemases are enzymes that convert L-amino acids to D-residues post-translationally, typically within the first three residues of the amino or carboxy terminus and the change imparts distinctive function to the variant.[4] For example, enzyme-catalyzed racemization is employed by the funnel web spider and the common platypus for venom toxicity.[5, 6] In addition, accumulation of D-aspartic acid in the human lens proteins alpha A-crystallin and alpha B-crystallin and beta-amyloid protein in the brain are associated with aging in humans.[7-9] Furthermore, researchers have discovered that chiral mutagenesis of insulin has helped to stabilize the therapeutic protein.[10]

Although free amino acids are able to undergo racemization, solution conditions required for such a process to occur are typically extreme with temperatures above 100 $^{\circ}$C and pH values above 8 or less than 5.[11] Metal-facilitated epimerization of metal-peptide complexes has been reported since the 1960s, with metals including Co^{II}, Ni^{II} and Cu^{II}.[12-16] Like racemases, the reactions of these metal-peptide complexes led to modification of the terminal residues. These metal-mediated reactions typically result in amino acid racemization, are first order in hydroxide ion concentration, and require elevated temperatures. These reactions are proposed to be initiated by deprotonation of the Cα to give a carbanion-containing intermediate, which is more favorable upon coordination of the peptide to the metal ion.[12, 16, 17] The metal centers in these complexes are typically square planar with four nitrogen donors. In addition, incubation of the complexes in

D$_2$O results in deuteron/proton exchange, presumably at the Cα-H site(s) that undergo(es) inversion.[16, 18]

The nickel complex of the metal abstraction peptide (MAP) tag asparagine-cysteine-cysteine (Ni-NCC) is a high-affinity metal-binding peptide that releases metal at reduced pH. In addition, Ni-NCC is both a structural and functional mimic of the protein Ni-SOD.[19] Electronic absorption and circular dichroism (CD) spectroscopic data show similar transition energies between Ni-NCC and Ni-SOD, indicating nearly identical coordination to the Ni^{II} center.[19] In the absence of crystallographic data, density functional theory (DFT) computations were employed to determine the lowest-energy structure of Ni-NCC and it was confirmed that the Ni^{II} is in a square plane, coordinated by *cis* deprotonated thiolates from Cys2 and Cys3, as well as the N-terminal amine and the deprotonated amide Cys2 nitrogen (Figure 3.1).[19] This coordination scheme is identical to that of Ni-SOD.[20, 21]
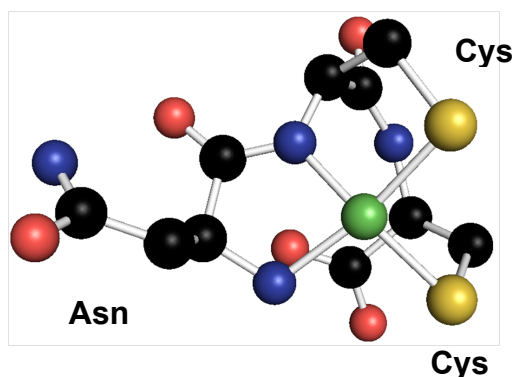

Figure 3.1. Chemical structure of Ni-NCC showing the square planar arrangement of 2N:2S coordination around the nickel ion.

The unique mixed amine/amide nitrogen environment, in addition to thiolate coordination, in Ni-SOD is proposed to be responsible for the unique reactivity in the enzyme, which is responsible for breakdown of the toxic radical anion superoxide.[22, 23] Although SODs are ubiquitous, the active site of Ni-SOD is distinct from the other classes of the enzyme in that it employs thiolate ligands, which are prone to oxidation by dioxygen and its reduced derivatives.[24] Curiously, superoxide is the substrate for Ni-SOD and yet metal-centered, rather than sulfur-based oxidation occurs during turnover. Although structural data is available for both the oxidized and reduced forms of the enzyme[20,25], some questions still exist regarding its mechanism.[26] Therefore, studies of the structure and chemical characteristics of Ni-NCC can lend insights into the reactivity of Ni-SOD.

Further stability analysis of Ni-NCCs hows that the electronic absorption and CD spectra of the complex change over time, in a manner consistent with chiral inversion of the ligand. No chiral inversion or racemization has been reported in either Ni-SOD, or in small molecule mimics or peptide-based maquettes that contain the metal-binding region of the protein sequence. Therefore, this modification of the peptide in Ni-NCC appears distinct from its activity as a Ni-SOD mimic. Although metal-amino acid complexes are known to undergo metal-facilitated, base-catalyzed racemization as a result of metal coordination, inversion is typically accomplished over several hours at highly elevated temperature (>90°C) and basic pH (>9).[12, 15, 17] In the work presented here, we report the first site-specific chiral inversion of amino acids that depends only on metal binding. In addition to determining the sites of chiral inversion, we also determined that the chiral inversion increases the superoxide consumption of the nickel-peptide complex.

3.3 Experimental

3.3.1 Generation of metal-peptide complexes. The peptides NCC, GCC, and NCC with a D-cysteine in the middle position [LDL-NCC] were purchased from Genscript Corporation (Piscatway, NJ, USA). The NCC peptides with a D-cysteine in the third position [LLD-NCC] and with both D-asparagine in the first position and D-cysteine in the third position [DLD-NCC] were purchased from Neo-Peptide (Cambridge, MA, USA). Nickel-peptide complexes were generated in aqueous solution at neutral to basic pH. Incubation of the peptide for approximately 30 minutes with immobilized metal affinity chromatography (IMAC) resin (GE Healthcare) charged with nickel ensures a clean reaction with no undesired side products and no free metal ions in solution, yielding a reddish-brown complex, varying slightly by the identity of the peptide. Aged Ni-NCC samples were allowed to age for >40 days. To accurately control the time frame of Ni-NCC aging for activity assays, the complex also was formed in solution upon addition of one equivalent of $NiSO_4$.

3.3.2. Circular dichroism (CD) and electronic absorption spectroscopies. A 1.5 mM solution of Ni-NCC was prepared in 50 mM potassium phosphate, pH 7.4, and used as is or purged with argon. Immediately after incubation, samples were placed in a cuvette with a 1-cm pathlength and scanned from 800-300 nm using both absorption and CD spectroscopy. Samples were aged and monitored at various time points over the course of several days. Background scans of buffer alone were subtracted from each scan. Absorption studies were performed on an Agilent 8453 UV/Visible spectrophotometer. Circular dichroism analysis was performed on a J-815 (Jasco Corporation) spectrapolorimeter. The CD data presented represent the average of at least five scans.

3.3.3. Magnetic CD (MCD) spectroscopy. A 6 mM Ni-NCC solution was prepared in 50 mM potassium phosphate buffer at pH 7.4 purged with argon. Solid sucrose was added as a glassing agent and the mixture was heated at 100 $^\circ$C to form a saturated solution with a final Ni-NCC concentration of 2 mM. CD spectra of sucrose-saturated samples demonstrated no significant changes in features compared with samples lacking sucrose, indicating that this procedure did not perturb the structures of the Ni-NCC complexes. The samples were placed in an MCD cell and flash frozen in liquid N_2. Spectra were collected on a J-815 (Jasco Corporation) spectropolarimeter interfaced with a magnetocryostat (Oxford Spectromag 4000-8). To remove contributions from CD signals, MCD data reported herein represent difference spectra of accumulations at +7 and -7 T. Because the signal intensities from paramagnetic species display inverse temperature dependences, spectra were collected at several temperatures.

3.3.4. Deconvolution of CD and electronic absorption data. Deconvolution of CD and absorption data was performed using Igor Pro (Wavemetrics). Iterative Gaussian deconvolutions were performed with a constant peak width of 1650 cm^{-1}. Absorption band energies were kept within 10% of the corresponding CD bands due to the broad nature of the absorption spectrum.

3.3.5. Electrospray ionization mass spectrometry (ESI-MS). Mass spectrometric data was performed by M. Krause. Samples were diluted 100x in a 1:1 mixture of methanol/water and analyzed on an LCT Premier (Waters Corporation) operating in negative ion mode, as described previously.[27]

3.3.6. Density Functional Theory (DFT) Computations. Spin-restricted density functional theory (DFT) computations were performed using ORCA 2.8.0[28] and employed the conductor-like screening model (COSMO)[29] with an epsilon value of 80 to approximate water. Geometry optimizations used the BP86 functional[30, 31] and the aug-TZVP basis set (a triple-zeta

basis set with diffuse and polarization functions).[32, 33] Because these computations employed the resolution of identity (RI) approximation,[34] the TZV/J auxiliary basis set was also used. Single point and time-dependent DFT (TD-DFT) computations used the B3LYP[35-37] functional and the aug-TZVP basis set. In order to evaluate if the inclusion of explicit water molecules hydrogen-bonded to charged groups gave rise to geometries markedly different than those obtained using COSMO, a water molecule was added to hydrogen bond with the C-terminal carboxylate in the LLL, DLD, and DDL models of Ni-NCC. Because differences in bond lengths of less than 0.015 Å were observed, we reasonably conclude that the use of COSMO is sufficient to account for major solvation effects in this system.

3.3.7. Ni-SOD xanthine/xanthine oxidase coupled assay. Ni-SOD activity was determined as reported previously,[27] except Ni-NCC was generated *in situ* using one equivalent NiSO$_4$. Ni-NCC was aged for 0 – 120 minutes, and the Ni-SOD activity was determined using the standard xanthine/xanthine oxidase method developed by Crappo and coworkers.[38] All reagents were generated in 50 mM potassium phosphate, 100 μM EDTA reaction buffer at pH 7.8 except for Ni-NCC, which was generated in 50 mM potassium phosphate, pH 7.4. Solutions of 600 μM cytochrome c from bovine heart (Sigma), 300 μM xanthine (Sigma) and enough xanthine oxidase from buttermilk (Sigma) were mixed to cause a change in absorbance at 550 nM of 0.02 – 0.04 AU per minute and were added to a final volume of 300 mL with reaction buffer. The change in absorbance at 550 nm was monitored on a Cary 100 UV-Visible spectrophotometer (Varian). The assay was performed with 100 mM Ni-NCC.

3.4. Results and Analysis

3.4.1. Preparation and CD spectroscopic characterization of Ni-NCC. As previously reported, metal incorporation into the described complex is most efficiently accomplished via metallation.[19] Peptides were incubated with IMAC resin in either 50 mM potassium phosphate buffer at pH 7.4 or in 50 mM sodium borate at pH 10. Absorption and CD spectroscopies were utilized to characterize the Ni-NCC complex. Studies have shown that pH, ionic strength, and concentration of the metal-peptide complex do not change the spectral features of the system. However, the studies show that the initial spectra differ between buffer systems (Figure 3.2) but later converge to a common final state.
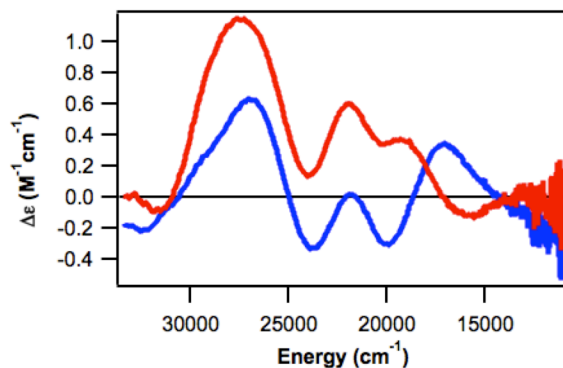

Figure 3.2. CD spectra of 1.5 mM Ni-NCC generated in pH 7.4 potassium phosphate (red) and pH 10.0 sodium borate (blue). These spectra were obtained after thirty minutes of incubation with IMAC resin charges with Ni^{II}.

Over time, however, the spectral features of Ni-NCC in phosphate buffer change to resemble those in borate buffer, suggesting rearrangement to a more stable structure occurs. Although samples were prepared in argon-purged solutions, no further precautions were taken to avoid oxygen dissolution during aging. To ensure complete conversion, a Ni-NCC sample in phosphate buffer was aged in air for 90 days and analyzed again (Figure 3.3). ESI-MS of the Ni-NCC complex in various conditions demonstrated that the peptide mass does not change with the changes in spectral features (m/z = 392.98), indicating a lack of oxidation of thiolate ligands. Varied pH did not affect the overall rate of the aging process (Figure 3.4). This suggests that the changes observed in the CD are due to more subtle changes about the metal center.
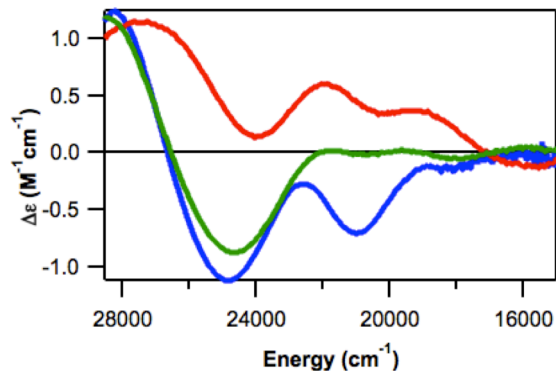

Figure 3.3. Aging progression of 1.5 mM Ni-NCC in pH 7.4 potassium phosphate buffer aged in air. Spectra include complex after thirty minutes of incubation with IMAC resin (red), twenty-four hours of aging (blue), and ninety days of aging (green).

3.4.2. CD spectral deconvolutions of Ni-NCC. In contrast to the changes in the CD spectra of Ni-NCC, absorption spectra of Ni-NCC freshly prepared in phosphate buffer and that same sample aged for 40 days appear nearly identical (Figure 3.5A). Both feature a broad envelope centered at 21 000 cm^{-1} (ε = 210 M^{-1}cm^{-1}) with a higher energy feature at 29 000 cm^{-1} (ε

59
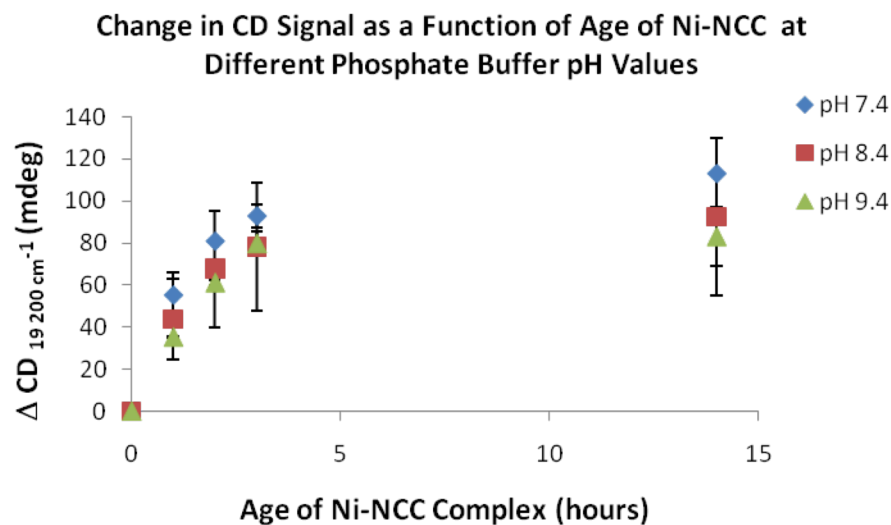
Figure 3.4. Change in CD spectrum at 19 200 cm^{-1} as 3 mM Ni-NCC generated from one equivalent of NiSO$_4$ ages in pH 7.4, 8.4, and 9.4 50 mM potassium phosphate. pH values were determined prior to dissolution of peptide or complex formation. Data represents the average of two experiments and error bars are the standard deviation of those two experiments.

= 1400 M^{-1}cm^{-1}). These data are consistent with both species having a four-coordinate Ni^{II} center in an N$_2$S$_2$ square planar geometry.[19] To quantitatively evaluate the CD spectral changes, spectral deconvolutions of these data were performed to determine the energies and signs of the electronic transitions (Figure 3.5B). Whereas freshly prepared Ni-NCC displays signals with positive sign at 18 900, 22 170, and 26 520 cm^{-1}, the spectrum of the aged sample shows negative bands at similar energies (Table 3.1). These transitions shift to slightly lower energies (shifts of ~200 – 900 cm^{-1}) with age. Bands 1 – 4 of freshly prepared Ni-NCC were previously assigned as *d-d* transitions[1] and their energies should be very sensitive to changes in geometry about the Ni^{II} center. The observation that the energies of these bands shift by < 900 cm^{-1} upon aging demonstrates that fresh and aged Ni-NCC have nearly identical coordination environments. The major spectral perturbations are predominately due to changes in sign and

intensity of CD features. These minor changes in the *d-d* transition energies (Table 3.1) along with the virtually identical absorption spectra (Figure 3.4A) of fresh and aged Ni-NCC demonstrate that the geometry and ligands of the Ni^{II} center are unaltered and that neither dimerization of the complex nor oxidation of the thiolate ligand occurs.

A.

B.
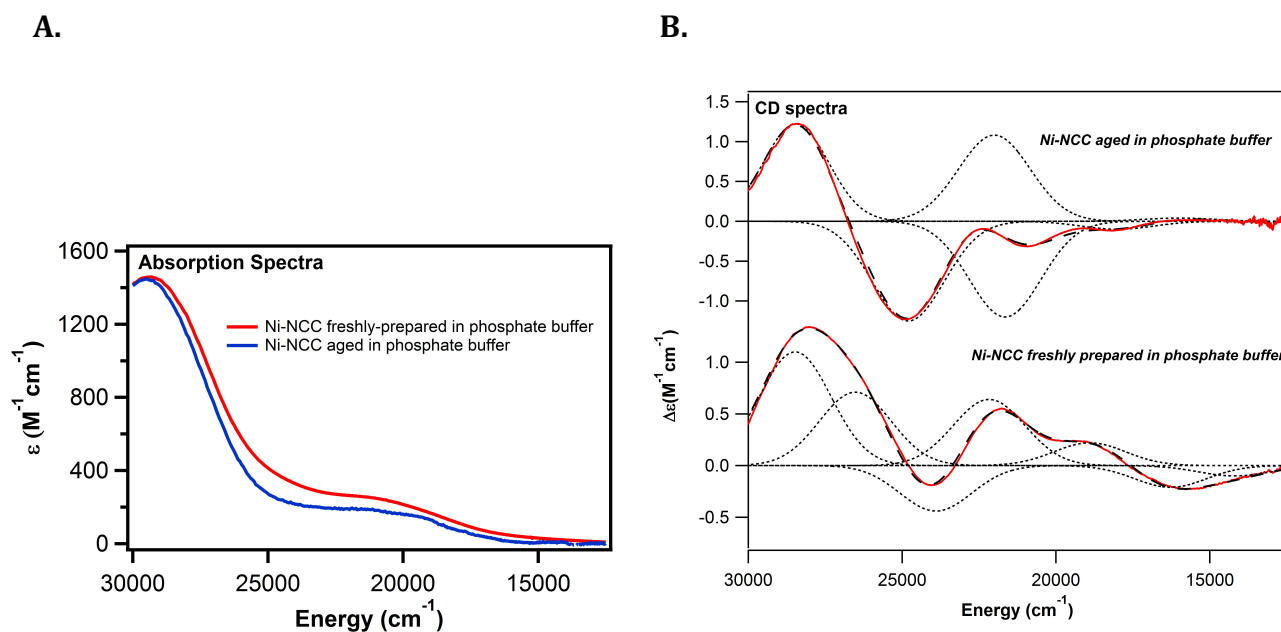
Figure 3.5. (A) Electronic absorption spectra of freshly prepared (red) and aged (blue) Ni-NCC in 50 mM phosphate buffer at pH 7.4. **(B)** CD spectra of the same samples. Individual Gaussian curves (···) and their sums (‐‐‐) obtained from fits of the CD data are displayed.

3.4.3. Magnetic circular dichroism studies of Ni-NCC. To investigate whether a paramagnetic, tetrahedral intermediate is formed, magnetic CD (MCD) experiments were perfomed. Previous MCD experiments have shown that the primary Ni-NCC species in borate buffer at pH 10 is largely diamagnetic, although a minor paramagnetic (*S*=1) species was present.[19] Here, MCD experiments performed on a freshly prepared Ni-NCC sample demonstrated that the species initially present in phosphate buffer is also primarily diamagnetic;

a minor paramagnetic component that accounts for less than 1% of the sample may reflect an

intermediate state that does not accumulate (Figure 3.6). After aging, these temperature-

Table 3.1. Transition energies derived from Gaussian deconvoluted CD spectra of freshly prepared and aged Ni-NCC in phosphate buffer. Bands having opposite sign in the fresh and aged spectra are shown in bold.

Band	Freshly Prepared		Aged	
	$\Delta\varepsilon$ ($M^{-1}cm^{-1}$)	Energy (cm^{-1})	$\Delta\varepsilon$($M^{-1}cm^{-1}$)	Energy (cm^{-1})
1	-0.1	14200	[a]	[a]
2	**-0.21**	**16270**	**0.04**	**16000**
3	**0.22**	**18900**	**-0.1**	**18000**
4	**0.64**	**22170**	**-0.78**	**21600**
5	**-0.44**	**23900**	**0.7**	**22000**
6	**0.71**	**26520**	**-1.3**	**24800**
7	1.1	28475	1.22	28450

[a]The low signal-to-noise ratio between 11 000 and 14 000 cm^{-1} precludes reliable deconvolution within this spectral window.

dependent signals are no longer observed. Therefore, it can be concluded that aged Ni-NCC

contains neither appreciable amounts of $S = 1$ Ni^{II} or $S = 1/2$ Ni^{III} centers. These data collectively

show that both fresh and aged Ni-NCC contain diamagnetic Ni^{II} centers in square planar

geometries with nearly identical coordination spheres; the differences in spectral features and in

reactivity between the freshly prepared and aged samples led to further investigation of the subtle

changes in the Ni-NCC complex.

3.4.4. Characterization of peptides containing D amino acids. The LDL-Ni-NCC, LLD-

Ni-NCC, and DLD-Ni-NCC complexes were generated and each analyzed using absorption and

CD spectroscopies and ESI-MS. All of the complexes exhibit the same mass profile

(*m/z*=392.98) in ESI-MS, suggesting that each forms 1:1 complexes with the metal. To determine

the chirality of the final, stable Ni-NCC arrangement, CD spectra of each D-containing peptide
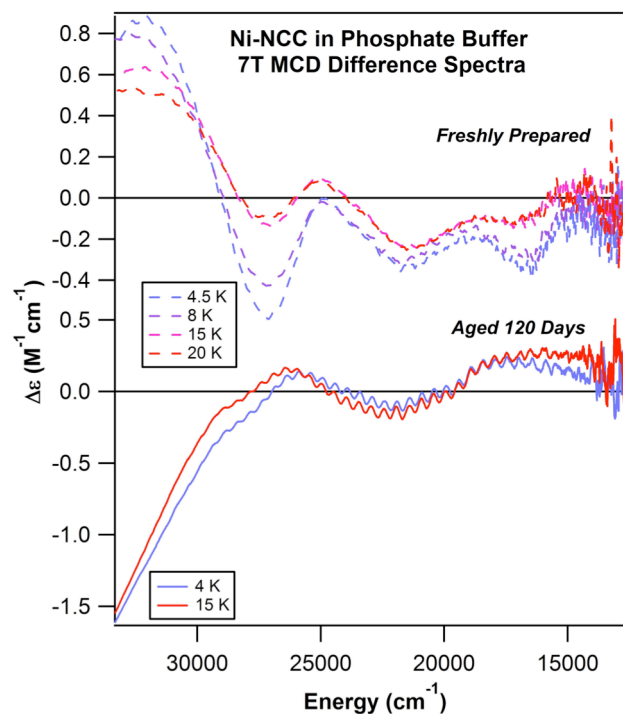
Figure 3.6. Variable-temperature MCD data collected for freshly-prepared (top) and aged (bottom) Ni-NCC in pH 7.4 potassium phosphate buffer with sucrose added as a glassing agent. The temperatures of data collection are designated on the plot. The aged sample had a starting concentration of 6 mM Ni-NCC with a final concentration of 2 mM Ni-NCC after addition of sucrose. The aged sample had a starting concentration of 3 mM Ni-NCC with a final concentration of 1 mM after addition of sucrose.

were compared to the data collected for the aged (>40 days) Ni-NCC sample in phosphate buffer.

The DLD-Ni-NCC spectrum overlaid with the aged Ni-NCC spectrum shows similar features (Figure 3.7). These data indicate chiral inversion occurs at the first and third positions within Ni-NCC to generate the DLD-Ni-NCC complex.
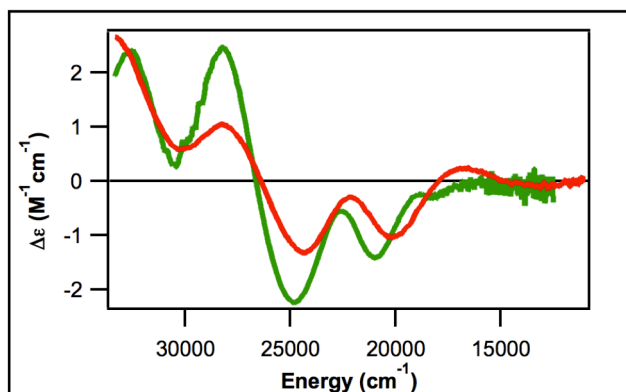
Figure 3.7. CD spectra of LLL-Ni-NCC aged for ninety days (green) and authentic DLD-Ni-NCC (red).

Whereas the spectral features of DLD-Ni-NCC do not shift or lose intensity with time, the CD spectrum of LLD-Ni-NCC evolves over time to look like that of DLD-Ni-NCC (Figure 3.8). In
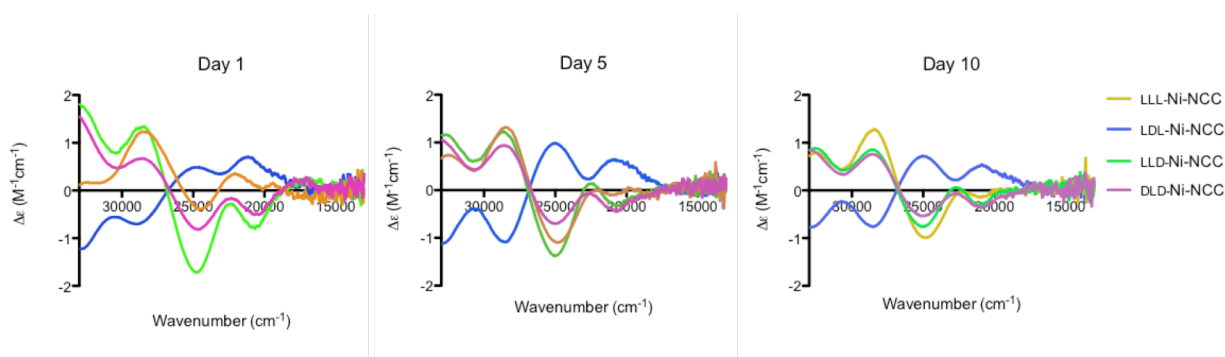

Figure 3.8. CD spectra of LLL-Ni-NCC (orange), LDL-Ni-NCC (blue), LLD-Ni-NCC (green), and DLD-Ni-NCC (pink) in pH 7.4 potassium phosphate buffer aged in air over the course of ten days.

contrast, the CD spectrum of aged LDL-Ni-NCC looks like the mirror image of that of DLD-Ni-NCC.

3.4.5. DFT-Optimized Models and Computed Energies. The similarities between the CD spectra of Ni-NCC and Ni-GCC show that metal binding in the two complexes is the same. Therefore, work with Ni-GCC allows for probing the role/effect of the cysteine residues in the absence of asparagine. Given that Ni-GCC shows incorporation of one deuterium over the course

of twenty-four hours, and has CD spectral changes consistent with inversion of chirality, it was concluded that Ni-GCC only has inversion at one of the Cα cysteine residues. Alternatively, in Ni-NCC, the complex has incorporation of two deuterium atoms over the course of twenty-four hours, consistent with inversion at two Cα positions. Given that Ni-NCC has inversion at one additional chiral site than Ni-GCC, and the only position that varies between the two is Asn1 in NCC versus Gly1 in GCC, it was concluded that Asn1 must undergo chiral inversion in Ni-NCC.

To explore the structural and energetic effects of chiral inversion on the tripeptide complexes, DFT computations were performed on models of different chiral forms of the Ni^{II}-NCC and Ni^{II}-GCC. In the absence of crystallographic data, these computations provide insight into the structure of the complex. Comparison of the single-point energies of XLL-Ni-GCC to XLD-Ni-GCC and XDL-Ni-GCC shows a small energetic stabilization of 2.0 kcal/mol upon inversion of the third residue, Cys3 and energetic destabilization of 14.0 kcal/mol if the inversion occurs instead at the second site, Cys2 (Figure 3.9). These data indicate that it may be the third residue, Cys3, in Ni-NCC that undergoes chiral inversion in addition to Asn1, if the mechanisms

XLL-Ni-GCC   XLD-Ni-GCC   XDL-Ni-GCC

0 kcal/mol   -2.0 kcal/mol   + 14.0 kcal/mol
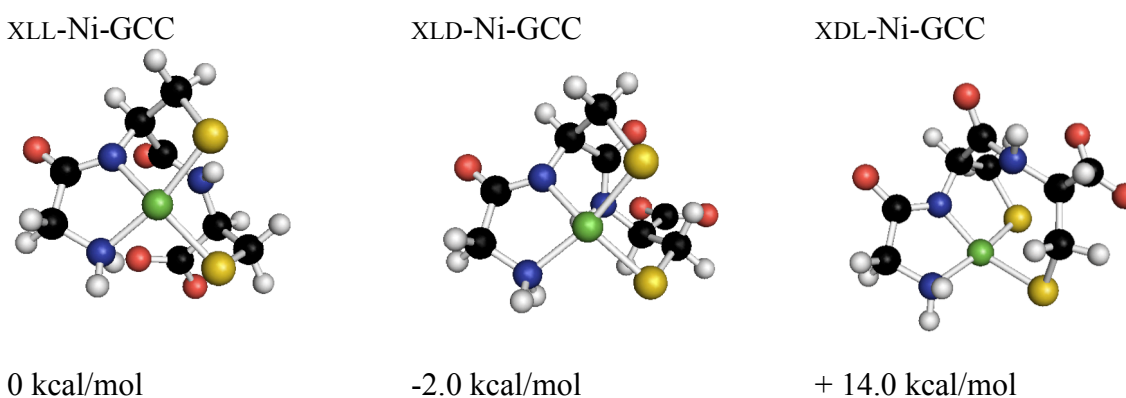
Figure 3.9. DFT-optimized geometries and relative single point energies for XLL-Ni-GCC, XLD-Ni-GCC and XDL-Ni-GCC.

of chiral inversion in the two complexes are analogous.

The DFT-calculated results for the different chiral forms of Ni-NCC are summarized in Table 3.2. In the optimized structure of LLL-Ni-NCC, the nickel(II) ion is bound in a near-square planar geometry (Figure 3.10). The coordination of the terminal amine, internal amide, and sulfur of Cys2 form two five-membered chelate rings that share a common edge. The sulfur of Cys3 coordinates *trans* to the amide nitrogen, which requires that the peptide wrap around the nickel center, thereby blocking one coordination site perpendicular to the square plane. The other open coordination site is partially blocked by the Asn side chain. These results suggest that the metal center may be sterically occluded in the LLL-peptide complex.

Table 3.2. Bond lengths (Å) and relative energies (kcal/mol) of DFT-optimized models of Ni^{II}-NCC with amino acids of differing chiralities. LLL-, DDL- and DLD-Ni-NCC also have included the bond distances in parentheses for the models that included a water molecule to stabilize the C-terminus. Energies given are for the models without water.

	LLL-Ni-NCC	DLL-Ni-NCC	LDL-Ni-NCC	LLD-Ni-NCC	DDL-Ni-NCC	DLD-Ni-NCC
$Ni-N_{amine}$	1.982 (1.982)	1.972	1.974	1.970	1.979 (1.978)	1.990 (1.992)
$Ni-N_{amide}$	1.859 (1.858)	1.856	1.867	1.866	1.866 (1.885)	1.887 (1.888)
$Ni-S_{cys2}$	2.187 (2.187)	2.184	2.165	2.311	2.164 (2.164)	2.196 (2.195)
$Ni-S_{cys3}$	2.201 (2.201)	2.199	2.199	2.262	2.199 (2.200)	2.238 (2.240)
Relative Energy	**0.0**	**-0.3**	**4.7**	**-11.6**	**5.1**	**-11.1**

The energies of Ni-NCC models with the chirality of different amino acids inverted show that inversion of Asn1 leads to a model (DLL-Ni-NCC) that is isoenergetic to that of LLL-Ni-NCC. In addition, the models in which Cys2 is inverted, LDL- and DDL-Ni-NCC, have an energetic destabilization of ~5 kcal/mol when compared to LLL-Ni-NCC. In contrast, when Cys3 is inverted, as in LLD- and DLD-Ni-NCC, an energetic stabilization of ~11 kcal/mol is predicted. Investigation into the role of solvation on the total energy of the conformers shows that although

DLD-Ni-NCC does have an overall stabilization with respect to LLL-Ni-NCC in solvation energy, the relief of steric strain of the loop containing Cys3 has a more pronounced effect on the total energy. These results for DLD-Ni-NCC agree with the experimental CD data described above (Figure 3.7). The inversion from LLL-Ni-NCC to DLD-Ni-NCC opens one face of the Ni^{II} ion to interact with exogenous ligands, consistent with the observation that aged Ni-NCC binds CN$^-$.
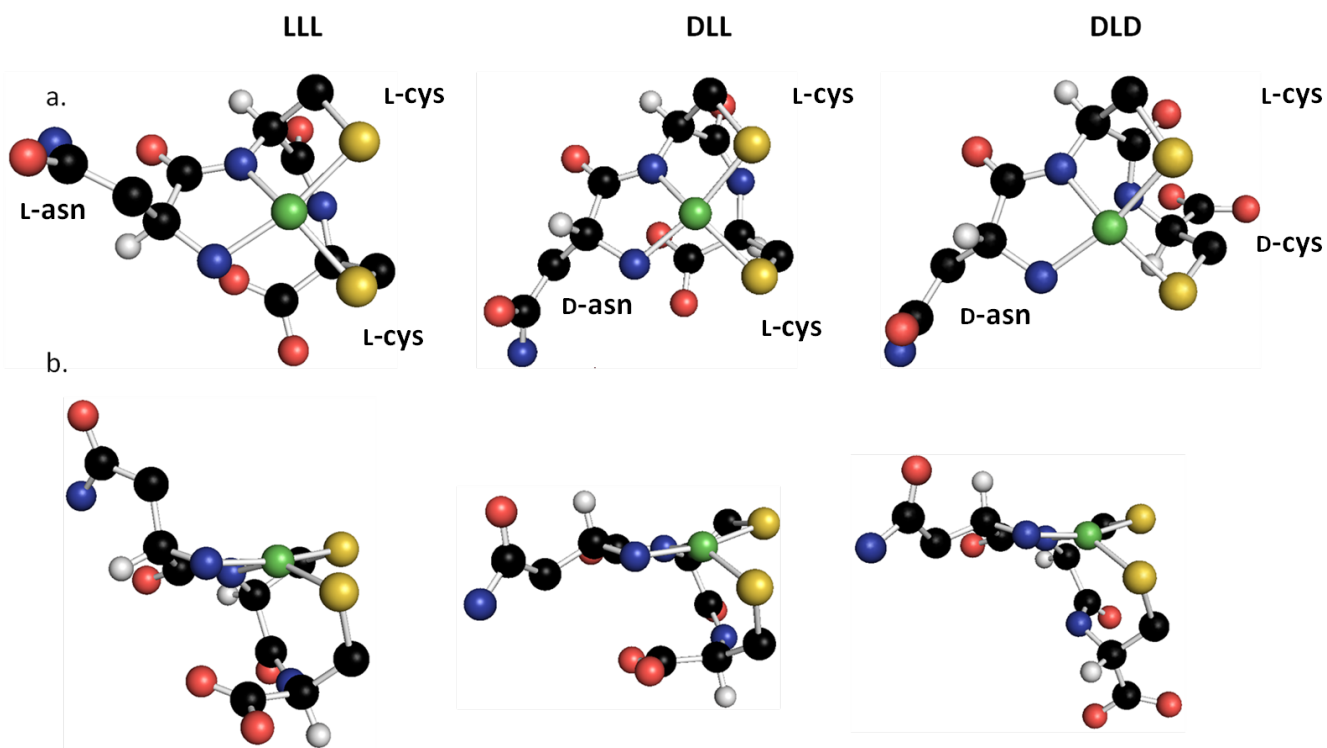

Figure 3.10. Energy-minimized structures of LLL-, DLL-, and DLD-Ni-NCC. The only hydrogen atoms shown are those attached to the Cα of the residues. Views perpendicular to the square plane (**A**) and in the plane (**B**) are shown.

3.4.6. Time Dependent-DFT (TD-DFT) computations. TD-DFT computations were performed to determine if the structural differences between LLL-Ni-NCC and DLD-Ni-NCC can account for the experimentally observed red-shift in the Ni^{II} *d-d* transition energies upon aging of Ni-NCC. Because Ni-S bond lengths are frequently overestimated in DFT geometry-optimized models, it is expected that the predicted electronic transition energies for both Ni-NCC models

will be computed at lower energy than experimentally observed. Nonetheless, this known shortcoming in DFT-computed Ni-S bond lengths[39] will not hinder the analysis performed here, as the focus is on reproducing the relative shift in Ni^{II} d-d transitions between LLL-Ni-NCC and DLD-Ni-NCC. For an $S = 0$, d^8 metal ion in a square planar geometry, four d-d transitions are expected from excitation from each of the four doubly-occupied d orbitals to the unoccupied $d_{x^2-y^2}$ orbital (Figure 3.12). The $d_{x^2-y^2}$ orbital is the most destabilized as it is the only orbital pointed directly along the metal-ligand bonds. The computed energies of these transitions are shown in Table 3.3; corresponding spectra are shown in Figure 3.11. Relative to LLL-Ni-NCC, all calculated d-d transitions for DLD-Ni-NCC are red-shifted, consistent with the experimental observation. This shift in transition energies is directly related to the energy of the $d_{x^2-y^2}$ orbital. In an idealized square planar geometry (*e.g.*, D_{4h} symmetry), the $d_{x^2-y^2}$ orbital is the dominant σ^* orbital and is significantly destabilized relative to the remaining four d orbitals. As the geometry is perturbed from this limit, other d orbitals take on partial σ^* character. This leads to the $d_{x^2-y^2}$ orbital being at a relatively lower energy and a red shift in d-d transitions. The nickel(II) coordination sphere in DLD-Ni-NCC is more distorted from square planar geometry than that of LLL-Ni-NCC, which gives rise to a smaller splitting between the Ni^{II} d orbitals (Figure 3.12) and thus red shifted d-d transitions.

Table 3.3. TD-DFT computed d-d transition energies (cm^{-1}) for Ni-NCC models.

Band	Electronic Transition	LLL	DDL	DLD
1	$d_{z^2} \rightarrow d_{x^2y^2}$	14 500	15 500	12 400
2	$d_{xy} \rightarrow d_{x^2y^2}$	15 600	16 600	14 300
3	$d_{yz} \rightarrow d_{x^2y^2}$	17 000	17 300	15 600
4	$d_{xz} \rightarrow d_{x^2y^2}$	19 300	18 800	18 500

TD-DFT computations performed for DDL-Ni-NCC predict the three lower-energy *d-d*

transitions to shift to higher-energy relative to LLL-Ni-NCC, which is inconsistent with

experimental data. Taken together, both the total energies of the Ni-NCC models and the results

of these TD-DFT computations are consistent with aged Ni-NCC corresponding to DLD-Ni-NCC,

where the chirality of Asn1 and Cys3 have been inverted.
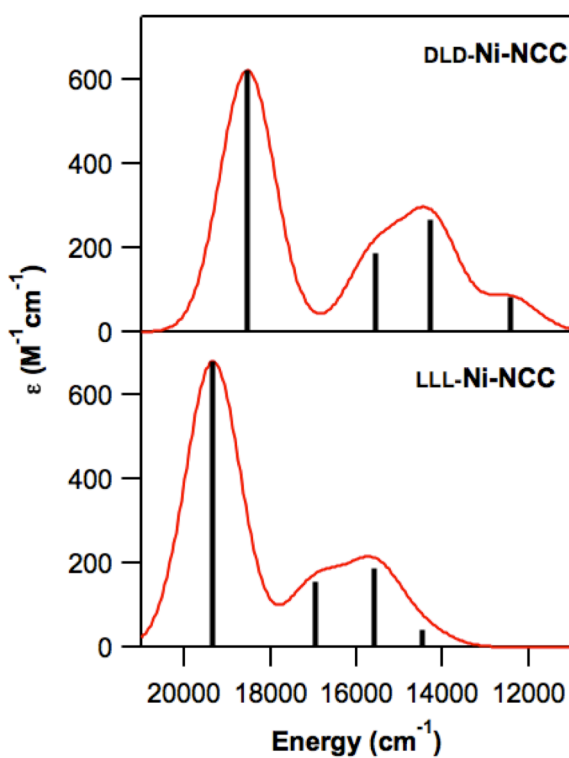
Figure 3.11. DFT predicted electronic absorption spectra of LLL-Ni-NCC (bottom) and DLD-Ni-NCC (top). The four Ni^{II} *d-d* transitions are marked with vertical lines.
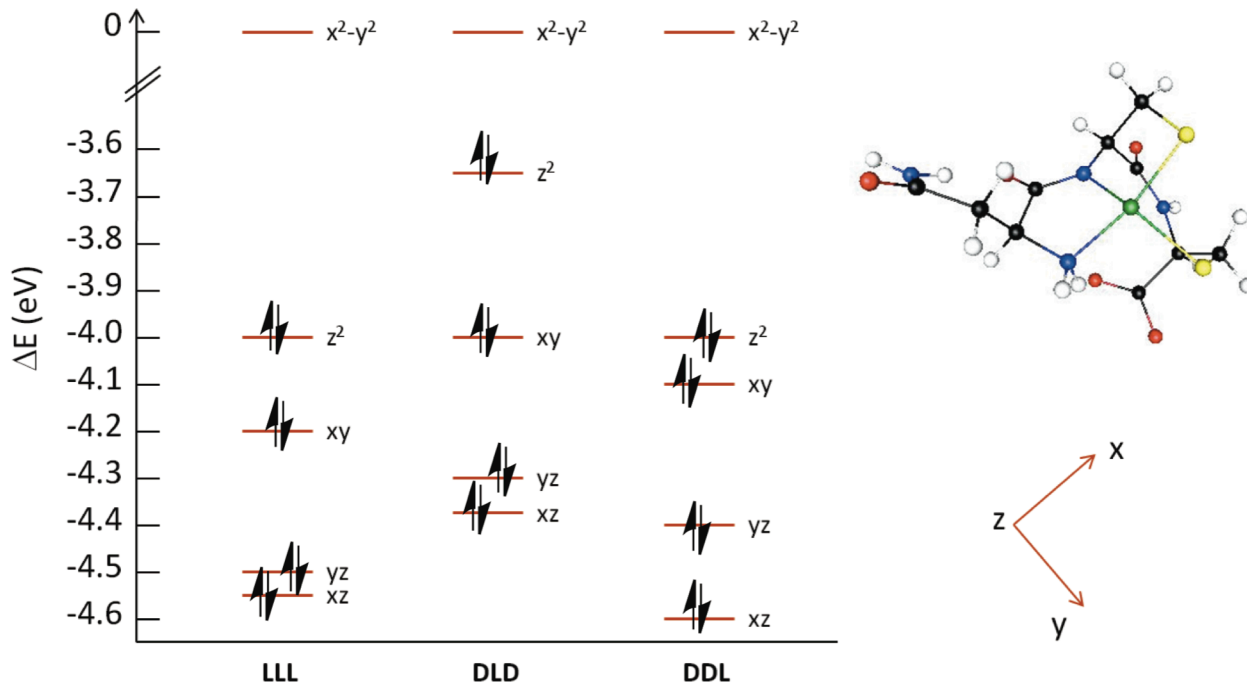
Figure 3.12. Ni^{II} *d*-orbital energy level diagram for the designated Ni-NCC models. A structural model of LLL-Ni-NCC and the coordinate system used for all models (where the z-axis is pointing into the plane of the page) are shown on the right.

3.4.7. Superoxide scavenging activity. The Ni-SOD activity assay was performed in order to probe whether the structural rearrangement that Ni-NCC undergoes while aging has an effect on the ability of the complex to consume the toxic anion superoxide. We previously showed that Ni-NCC behaves as a functional mimic of Ni-SOD, with an IC$_{50}$ value of 41 μM.[19] Activity is reported as an IC$_{50}$ value because the assay only measures the consumption of superoxide. Additionally, the concomitant chiral inversion with aging of the complex hampered detailed kinetic analysis of the superoxide consumption for Ni-NCC.

As computational analysis revealed, the final low-energy conformation DLD-Ni-NCC results in a more exposed Ni ion for solvent accessibility and reactivity with exogenous ligands. Assuming that the superoxide binds directly to the nickel center via an inner sphere mechanism, this rearrangement is supported experimentally by the observed increase in superoxide

consumption over time, as well as the lack of cyanide binding to Ni-NCC initially, prior to chiral inversion.[19] Control experiments with $NiSO_4$ verify SOD activity is only detected when Ni-NCC is present in solution and this activity was measured at several time points while the Ni-NCC complex was aged. The activity change, as determined using the xanthine/xanthine oxidase assay, increased linearly with respect to time over the first several hours of the experiment. The initial activity was subtracted from the value measured for each aged sample, and these data were fit to a linear equation. Two replicates involving a total of 12 data points were analyzed to compare the change in SOD activity with the change in chirality of the aged Ni-NCC complex between 0 and 90 minutes. The data comparison shows a linear correlation between these two parameters with R^2 values of 0.9242 and 0.9543. In addition, the functional data were compared
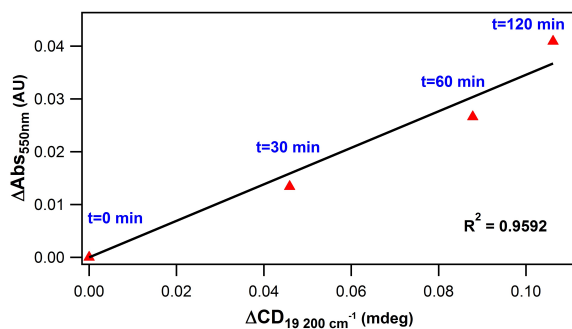

Figure 3.13. Change in SOD activity of Ni-NCC as a function of structural change over time, as measured by CD spectroscopy.

to the intensity changes in the CD spectra at the same time points during the aging process. A linear relationship between SOD activity and chiral inversion was observed (R^2 = 0.9592), revealing a direct correlation between this structural change and SOD activity of the Ni-NCC complex (Figure 3.13).

3.5 Discussion

Metal incorporation into the described Ni-NCC complex is accomplished rapidly (within seconds) via metallation.[19] The studies described here show that, following complex formation, chiral inversion occurs to generate the DLD-Ni-NCC, which correlates to SOD activity. The initial CD spectra acquired immediately following metal abstraction by the peptide differ among buffer systems but later converge to a common final state. Samples prepared in borate buffer reach the rearranged, final state much faster than samples prepared in phosphate buffer. The Ni-NCC samples prepared in borate buffer also immediately coordinate cyanide in the axial position, while the Ni-NCC samples prepared in phosphate buffer must be aged overnight before cyanide coordination can be detected. As mentioned above, these data lend support to a slower structural rearrangement that occurs over the course of hours-days, resulting in a structural state that allows for the interaction of a fifth ligand with the Ni-NCC complex. Similarly, Ni-NCC prepared in borate buffer has a midpoint potential that can be measured immediately using CV, whereas samples prepared in phosphate buffer must be aged overnight before any electrochemical signal is observed. These studies demonstrate that there is a difference between the final and initial arrangements of Ni-NCC that are observed in different buffer systems. The initial state is likely the all L-coordinated square planar arrangement, which the DFT computations suggest would be sterically hindered from binding even small ligands, *i.e.* CN⁻ and superoxide. Furthermore, MCD experiments reveal that both the Ni-NCC species measured immediately after complexation and then after aging are predominantly $S=0$ square planar.

The differences in spectral features and in reactivity between the freshly prepared and aged samples of Ni-NCC prompted further investigation of the subtle changes in the Ni-NCC complex. Using spectroscopic and ESI-MS studies, including those involving deuterium

exchange, it was proposed that a change in the chirality of specific residues within this metal-peptide complex occurs as a result of metal binding. The incorporation of deuterium into non-exchangeable positions further supports chiral rearrangement.

Studies on the D-containing control peptides helped elucidate the positions directly influenced by chiral inversion. A Ni-GCC sample was examined in the same manner to evaluate the influence of chirality at the first alpha carbon position. Although the spectra for these two complexes are not expected to be identical, a similar trend was observed for Ni-GCC in a similar time frame, suggesting that conversion occurs in the second and/or third positions. Recalling that NCC increased in mass by 2 amu during the deuterium exchange experiment, but GCC only increased by 1 amu and additionally taking into consideration that Gly is achiral, the data collectively indicate that only one of the Cys residues undergoes chiral inversion and that in NCC the first residue is also altered.

To determine which cysteine residue undergoes chiral inversion, the D-containing peptide complexes LDL-Ni-NCC, LLD-Ni-NCC, and DLD-Ni-NCC were characterized. All of the complexes exhibit the expected mass profile when examined using ESI-MS, suggesting that the same moieties from each of these peptides participate to accomplish metal binding using the same geometry. In general, inversion of the chirality at the metal center leads to CD spectra that are complete mirror images of one another;[40] however, changes in the CD spectra cannot be easily assigned to chiral inversions at individual positions in the peptide, and as such, the best indicator of the chirality of the final stable state is obtained through comparison to standards.

By overlaying the spectra of the D-containing peptides with the aged Ni-NCC spectra, it is evident that the DLD-Ni-NCC spectrum displays the same features as the aged Ni-NCC spectrum. These data are consistent with chiral inversion occurs at the first and third position

within Ni-NCC to generate the DLD-Ni-NCC complex. Moreover, it is obvious that the data for the aged all-L peptide does not correspond to inversion in the central position (Cys2), as the LDL peptide yields a spectral mirror image of the aged complex. The changes observed in the aged LLL complex rather closely, but do not exactly, parallel those associated with D-Cys in the third position, as demonstrated by comparison to LLD-Ni-NCC. All of the possible permutations of chirality were tested with DFT, showing the DLD form to be the most thermodynamically favorable. Based on the DFT calculations, there is a very large difference in energy between the peptides containing an L or D amino acid in that third position, strongly corroborating that the DLD peptide-metal complex is highly favorable.

The Ni-NCC complex was previously shown to mimic the Ni-SOD reaction in which a single electron is transferred through the metal center.[27] Here we show that the SOD activity of Ni-NCC increases as the complex ages, and the activity is linearly and directly related to the structural rearrangement of the complex. Although the structural rearrangement was unknown at the time of our previous report[1], the IC_{50} of the aged Ni-NCC sample is comparable with that value, indicating the original IC_{50} reflected a mostly chirally converted Ni-NCC species. The direct measurement of the DLD complex also has a comparable IC_{50}, indicating this is the species with SOD activity. Chiral inversion has not been observed in the Ni-SOD protein or small peptide maquettes that have been used to probe the mechanism and structure of this protein. Although metal binding is accomplished with the same geometry and direct coordinating atoms in both cases, the connectivity among these atoms is not analogous. As the data and computations indicate, structural rearrangement of Ni-NCC from LLL to DLD promotes SOD activity by potentially overcoming the steric hinderance that blocks ligand access to the axial position. In addition, shifts in the energy of the Ni $d_{x^2-y^2}$ will also affect the $Ni^{II/III}$ reduction

potential. Chiral inversion results in a substantially more favorable energy for the complex and a structure in which one face of the square planar Ni^{II} ion becomes more available for interaction with solvent, exogenous ligand, or potential substrate.

Finally, after examining the control DLD complex immediately following formation, the IC_{50} value was determined to be 39 µM, which is the same as the aged LLL-Ni-NCC species, indicating conversion to the DLD form confers activity.

3.6 References

1.   Hvidsten, T. R.; Laegreid, A.; Kryshtafovych, A.; Andersson, G.; Fidelis, K.; Komorowski, J., *Plos One* **2009,** *4* (7).

2.   Gaffield, W.; Incardona, J. P.; Kapur, R. P.; Roelink, H., *Cell. Mol. Biol.* **1999,** *45* (5), 579-588.

3.   Corrigan, J. J., *Science* **1969,** *164* (3876), 142-&.

4.   Conti, P.; Tamborini, L.; Pinto, A.; Blondel, A.; Minoprio, P.; Mozzarelli, A.; De Micheli, C., *Chem. Rev.* **2011,** *111* (11), 6919-6946.

5.   Bansal, P. S.; Torres, A. M.; Crossett, B.; Wong, K. K. Y.; Koh, J. M. S.; Geraghty, D. P.; Vandenberg, J. I.; Kuchel, P. W., *J. Biol. Chem.* **2008,** *283* (14), 8969-8975.

6.   Jilek, A.; Kreil, G., *Montash. Chem.* **2008,** *139* (1), 1-5.

7.   Fujii, N.; Kawaguchi, T.; Sasaki, H.; Fujii, N., *Biochemistry* **2011,** *50* (40), 8628-8635.

8.   Fujii, N.; Satoh, K.; Harada, K.; Ishibashi, Y., *J. Biochem.* **1994,** *116* (3), 663-669.

9.   Roher, A. E.; Lowenson, J. D.; Clarke, S.; Wolkow, C.; Wang, R.; Cotter, R. J.; Reardon, I. M.; Zurcherneely, H. A.; Heinrikson, R. L.; Ball, M. J.; Greenberg, B. D., *J. Biol. Chem.* **1993,** *268* (5), 3072-3083.

10. Nakagawa, S. H.; Hua, Q. X.; Hu, S. Q.; Jia, W. H.; Wang, S. H.; Katsoyannis, P. G.; Weiss, M. A., *J. Biol. Chem.* **2006,** *281* (31), 22386-22396.

11. Bada, J. L., *J. Am. Chem. Soc.* **1972,** *94* (4), 1371-1373.

12. Buckingham, D. A.; Marzilli, L. G.; Sargeson, A. M., *J. Am. Chem. Soc.* **1967,** *89* (20), 5133.

13. Fujioka, M.; Nakao, Y.; Nakahara, A., *Bull. Chem. Soc. Jpn.* **1976,** *49* (2), 477-479.

14. Gillard, R. D.; Phipps, D. A., *J. Chem. Soc. Chem. Comm.* **1970,** (13), 800-&.

15. Pasini, A.; Casella, L., *J. Inorg. Nucl. Chem.* **1974,** *36* (9), 2133-2144.

16. Williams, D. H.; Busch, D. H., *J. Am. Chem. Soc.* **1965,** *87* (20), 4644.

17. Stadtherr, L. G.; Angelici, R. J., *Inorg. Chem.* **1975,** *14* (4), 925-930.

18. Krause, M. E.; Glass, A. M.; Jackson, T. A.; Laurence, J. S., *Inorg. Chem.* **2011,** *50* (6), 2479-2487.

19. Krause, M. E.; Glass, A. M.; Jackson, T. A.; Laurence, J. S., *Inorg. Chem.* **2010,** *49* (2), 362-364.

20. Barondeau, D. P.; Kassmann, C. J.; Bruns, C. K.; Tainer, J. A.; Getzoff, E. D., *Biochemistry* **2004,** *43* (25), 8038-8047.

21. Bryngelson, P. A.; Arobo, S. E.; Pinkham, J. L.; Cabelli, D. E.; Maroney, M. J., *J. Am. Chem. Soc.* **2003,** *126* (2), 460-461.

22. Fiedler, A. T.; Bryngelson, P. A.; Maroney, M. J.; Brunold, T. C., *J. Am. Chem. Soc.* **2005,** *127* (15), 5449-5462.

23. Neupane, K. P.; Shearer, J., *Inorg. Chem.* **2006,** *45* (26), 10552-10566.

24. Mirza, S. A.; Pressler, M. A.; Kumar, M.; Day, R. O.; Maroney, M. J., *Inorg. Chem.* **1993,** *32* (6), 977-987.

25. Herbst, R. W.; Guce, A.; Bryngelson, P. A.; Higgins, K. A.; Ryan, K. C.; Cabelli, D. E.; Garman, S. C.; Maroney, M. J., *Biochemistry* **2009,** *48* (15), 3354-3369.

26. Valentine, J. S., Superoxide Dismutases and Reductases. In *Biological Inorganic Chemistry: Structure and Reactivity*, Bertini, I.; Gray, H. B.; Stiefel, E. I.; Valentine, J. S., Eds. University Science Books: Sausalito, California, 2007; pp 331 - 353.

27. Krause, M. E.; Glass, A. M.; Jackson, T. A.; Laurence, J. S., *Inorg. Chem.* **2010,** *49*, 362-364.

28. Neese, F. *ORCA - an ab initio, Density Functional and Semiempirical Program Package*, Version 2.8; University of Bonn: 2009.

29. Sinnecker, S. R., A.; Klamt, A.; Diedenhofen, M; Neese, F., *J. Phys. Chem. A* **2006,** *110*, 2235-2245.

30. Becke, A. D., *J. Chem. Phys.* **1986,** *84*, 4524-4529.

31. Perdew, J. P., *Phys. Rev. B.* **1986,** *33*, 8822-8824.

32. Schaefer, A.; Horn, H.; Ahlrichs, R., *J. Chem. Phys.* **1992,** *97* (4), 2571-7.

33. Schaefer, A.; Huber, C.; Ahlrichs, R., *J. Chem. Phys.* **1994,** *100* (8), 5829-35.

34. Neese, F., *J. Comput. Chem.* **2003,** *2003*, 1740-1747.

35. Becke, A. D., *J. Chem. Phys.* **1993,** *98*, 1372-1377.

36. Becke, A. D., *J. Chem. Phys.* **1993,** *98*, 5648-5652.

37. Lee, C.; Yang, W.; Parr, R. G., *Phys. Rev. B.* **1988,** *37*, 785-789.

38. Crapo, J. D.; McCord, J. M.; Fridovich, I., *Methods Enzymol.* **1978,** *53*, 382-393.

39. Bruschi, M.; De Gioia, L.; Zampella, G.; Reiher, M.; Fantucci, P.; Stein, M., *J. Biol. Inorg. Chem.* **2004,** *9*, 873-884.

40.   Amouri, H.; Gruselle, M., *Chirality and Entantiomers. In Chirality in Transition Metal Chemistry: Molecules, Supramolecular Assemblies, and Materials*. Wiley: 2009.

Chapter 4: Dioxygen dependence on the chiral inversion reaction of Ni-NCC

4.1 Introduction.

Metal-peptide complexes (metallopeptides) can serve as important biotechnological tools, due in part to their ability to facilitate drug delivery, affect DNA cleavage, and enhance site-specific protein modifications.[1-8] In addition, metallopeptides offer an attractive advantage over their full-length metalloprotein analogues for the mimicking of structure and function, as the small-molecule complexes are often easy to handle and produce in the laboratory, yet can still provide chemical insight into the corresponding biological reactions.[9,10] However, many metallopeptides undergo peptide-modifying reactions that lead to a change in structure and/or chemical properties.[4,11-14] Strict control of the reactivity of these complexes is necessary to achieve the desired chemistry and avoid either deleterious side reactions or inactivation of the complex.

Metal-facilitated peptide modifications include ligand oxidation, spontaneous disulfide bond formation, decarboxylation, hydroxylation, and racemization.[11,15-18] It was recognized in the 1960s that peptide binding to transition metals, such as Co^{II}, Cu^{II} and Ni^{II}, can lead to amino acid racemization under conditions of elevated pH and/or temperature.[18-22] The rates of these

racemization reactions show a first-order dependence on OH⁻ concentration,[23] and carbanion intermediates have been detected using acetaldehyde as a trapping agent.[19] The initiating step in peptide racemization was therefore proposed to be deprotonation of the $C\alpha-H$ group to generate a carbanion intermediate that is subsequently quenched by a proton. Presumably, coordination of the amino or carboxylate group of the peptide to the metal center sufficiently lowers the pK_a of the $C\alpha-H$ group to support deprotonation at elevated pH or high temperatures. In fact, it has been proposed that for the carboxy-terminal amino acid residue to undergo inversion, the carboxylate must be bound to the metal center.[20]

We previously published the first example of a metal-peptide complex that undergoes chiral inversion at neutral pH and room temperature.[3] The metal-tripeptide complex nickel(II)-asparagine-cysteine-cysteine, ($[Ni^{II}-NCC]^{2-}$ or Ni^{II}-NCC), undergoes chiral inversion under ambient conditions at pH 7.3 (Figure 4.1, bottom).[3] The CD spectra of freshly-prepared Ni^{II}-NCC and the same sample aged 40 days show a complete change in sign in many features (Figure 4.1, top), indicative of the chiral inversion reaction.[3] At 24 hours of aging, an intermediate spectrum is observed (Figure 4.1, top). On the basis of comparison of the CD spectra of aged Ni^{II}-NCC with that of authentic D-containing Ni^{II}-NCC compounds, it was concluded that LLL-Ni^{II}-NCC converts completely to DLD-Ni^{II}-NCC. Density functional theory (DFT) calculations suggest the chiral inversion is thermodynamically driven, with an 11 kcal/mol stabilization for DLD-Ni^{II}-NCC relative to the LLL isomer.[3] Preliminary studies that investigated the pH dependence of this process did not support a first-order rate dependence on OH⁻ concentration, suggesting a novel mechanism for chiral inversion. Indeed, the nickel(II) coordination in Ni^{II}-NCC is distinct from that of other metallopeptides that undergo chiral inversion.[24] Other metallopeptides that undergo racemization feature metal centers coordinated

in a 4N environment, whereas Ni-NCC employs both nitrogen and sulfur ligands in its square-planar 2N:2S first coordination sphere (Figure 4.1, bottom).

In addition, Ni^{II}-NCC is both a structural and functional mimic of nickel superoxide dismutase, Ni-SOD, which catalyzes the breakdown of the toxic byproduct of aerobic metabolism, superoxide.[25] Although thiolate ligation is known to tune the reduction potential of the nickel centers in metalloenzymes,[26] it is curious that nature employs sulfur ligation in Ni-SOD. Sulfur ligands are known to be prone to oxidation by O_2 and its reduced derivatives, yet during turnover of O_2^- in Ni-SOD, only metal-based oxidation is observed.[27,28] Intriguingly, the extent of chiral inversion in Ni^{II}-NCC is correlated with its superoxide scavenging ability.[3,25]

In this work, we demonstrate that the chiral inversion of LLL-Ni^{II}-NCC to DLD-Ni^{II}-NCC depends critically on dioxygen. Even at elevated pH, the chiral inversion does not occur in the absence of O_2. Acetaldehyde trapping experiments suggest the formation of two carbanion intermediates. These data, along with the detection of superoxide when Ni^{II}-NCC is incubated with O_2, provide evidence that chiral inversion of LLL-Ni^{II}-NCC proceeds by the formation of a carbanion in a Ni^{III}-NCC intermediate. In the absence of O_2, the Ni^{II}-form of NCC is completely inactive towards chiral inversion and stable at least over the course of 10 hours. In addition, complementary investigations of DLD-Ni^{II}-NCC suggest this complex is also reactive when exposed to O_2 and may undergo minor secondary reactions such as racemization. The relevance of these data for the reactivity of metallopeptides and nickel-dependent enzymes is discussed.
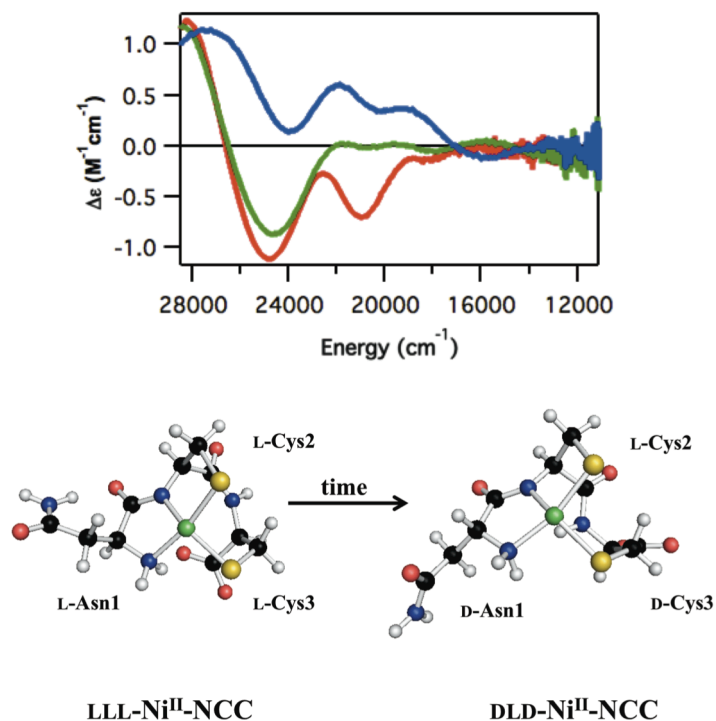
Figure 4.1. CD spectra of O$_2$-exposed LLL-Ni^{II}-NCC freshly-prepared (blue), aged 10-hours (green) and aged forty days (red). Structures of LLL-Ni^{II}-NCC (left) and DLD-Ni^{II}-NCC (right).

4.2. Experimental.

4.2.1 Preparation of O$_2$-exposed samples. . LLL-NCC (91.3% purity) was purchased as a lyophilized powder from GenScript, and stored desiccated at -20 °C when not in use. Authentic D-containing peptides, DLD-NCC (95.5%), LLD-NCC (94.6%), and DLL-NCC (88.1% purity) were purchased from NeoBioSci and were stored the same way. The peptide was reconstituted with 50 mM potassium phosphate buffer, generated from dibasic potassium phosphate (Fisher). Following dissolution, 1.0 or 1.2 molar equivalents of NiSO$_4$•6H$_2$O (Fisher) in deionized water were added, and the solution was inverted to ensure good mixing, just before the sample was inserted into the spectrometer for analysis. Samples were adjusted to the appropriate pH with either HCl or KOH, and all pH values reported reflect the final solutions after addition of NCC

and NiSO$_4$. Samples generated for spectroscopic analysis were generated with 1.2 molar equivalents of Ni^{II} to ensure maximum complex formation, whereas those that were produced for nitroblue tetrazolium (NBT) and acetaldehyde assays were made with 1.0 molar equivalent of Ni^{II} ion.

4.2.2. Preparation of O$_2$-free samples. Peptide was reconstituted in 50 mM potassium phosphate buffer of the designated pH and transferred to a quartz cuvette that was stoppered with a Suba-Seal septum and further sealed with parafilm. NiSO$_4$ prepared in water was placed into a small vial secured with a septum and also sealed with parafilm. Samples were purged with 99.5% Ar that was itself purified by passage through columns of activated BASF catalyst and molecular sieves for 20 – 30 minutes to remove O$_2$. Then 1.2 equivalents of Ar-purged NiSO$_4$ in water were transferred to the NCC solution using a gastight syringe. The septum was sealed with parafilm, the solution slowly agitated for $\sim$ 2 minutes to ensure proper mixing, and then the cuvette was placed in the spectrometer for data collection and left for the duration of the experiment.

4.2.3. Electronic absorption spectroscopy. Electronic absorption spectra were collected with either a Cary 50 or Agilent 5500 diode array ultraviolet-visible spectrophotometer. All spectra were collected in one cm path length quartz cuvettes with samples at room temperature. O$_2$-exposed samples were stirred during data collection using the interfaced Unisoku cryostat to promote efficient mixing. Ar-purged solutions were not stirred, but were inverted gently prior to data collected to promote efficient mixing. Spectra were collected every 0.1 min for the first 60 minutes and then every minute thereafter for a minimum of 167 minutes. To monitor formation of Ni^{II}-NCC for O$_2$-exposed samples, full-spectra were collected for a total of at least 167

minutes with a spectrum collected every second for the first hour and then attenuated by 1% for each data collection point following.

4.2.4. Nitroblue tetrazolium reduction assay. The nitroblue tetrazolium (NBT) assay was performed to detect the presence of the superoxide anion (O_2^-) during the chiral inversion reaction of Ni-NCC. Conversion of NBT (yellow) to its four-electron reduced form, diformazin (blue), results in an increase in absorption at 530 nm. Ni^{II}-NCC was generated by addition of one molar equivalent of 0.1 M $NiSO_4$ in water to 3 mM NCC in pH 7.3 potassium phosphate buffer. The Ni^{II}-NCC mixture was briefly mixed to ensure homogeneity and then the appropriate volume of 12 mM NBT (Alfa Aesar) in pH 7.3 potassium phosphate buffer was added rapidly, to determine the effect of aging Ni^{II}-NCC on the oxidation of NBT to diformazin. Final concentrations of Ni^{II}-NCC and NBT were 0.75 mM and 0.15 mM, respectively. Absorption spectra were collected to monitor the formation of diformazin over the course of one hour.

4.2.5. Carbanion trapping with acetaldehyde. In order to determine if a carbanion is an intermediate en route to chiral inversion in Ni-NCC, the aging complex was treated with acetaldehyde (ACS Reagent Grade, ≥ 99.5%, Sigma-Aldrich) and the reaction was monitored via electrospray ionization mass spectrometry (ESI-MS) on an LCT Premier (Waters Corporation) instrument operated in the positive ion mode. It has been established that aldehydes can react with carbanion intermediates in solution, resulting in the formation of a product with an increased mass equivalent to that of the deprotonated aldehyde.[22,29] For example, an increase of 43 *m/z* (the molecular mass of CH_3CHO is 44 Da) indicates the quenching of a single carbanion unit using acetaldehyde. Therefore, we monitored the reaction of acetaldehyde with aging Ni^{II}-NCC via ESI-MS and looked for the formation of a new major ion peak corresponding to an increased mass, indicating quenching of the carbanion and addition of the aldehyde to the ligand.

Ni^{II}-NCC was treated with excess (>30 equivalents) acetaldehyde and the reaction was allowed to incubate for at least 24 hours at room temperature.

4.2.6. Electron paramagnetic resonance (EPR) spectroscopy. X-band (9 GHz) EPR spectra were collected on a Bruker EMXplus spectrometer, fitted with an Oxford ESR900 continuous-flow liquid helium cryostat and an Oxford ITC503 temperature system to monitor and regulate temperatures. Data were collected at 123 K with liquid nitrogen as the cryogen. LLL-Ni^{II}-NCC samples were generated as described above in pH 7.3 50 mM potassium phosphate buffer with 1.2 equivalents of NiSO$_4$ added at t = 0. Samples were then allowed to age for a designated time. To each sample was added a 10% by volume saturated sucrose solution as a glassing agent to enhance spectral features. Once prepared, samples were flash frozen in liquid nitrogen and stored at 77 K until data collection.

4.2.7. Circular dichroism (CD) spectroscopy. . CD spectra were collected on a Jasco J-815 spectropolarimeter, using samples generated in quartz cuvettes. Spectra were scanned between 300 and 900 nm (33 333 and 11 111 cm^{-1}) unless otherwise noted. Instrumental parameters included 0.5 s response, 0.2 nm data pitch, 500 nm/min scan rate, and 5 nm bandwidth. Spectra were collected every ten minutes for a total of 600 minutes (61 total spectra collected) unless otherwise noted.

4.2.8. O$_2$ addition to O$_2$-free prepared Ni-NCC. Solutions of O$_2$-free Ni-NCC were generated as described previously. The Ni^{II}-NCC sample was incubated O$_2$-free for 300 minutes, and monitored by CD spectroscopy, in order to ensure maximum Ni^{II}-NCC complex formation. O$_2$ was added to the sample via bubbling for one minute. Prior it its addition, the O$_2$ was stored in a balloon, over a column of DriRite. CD spectra were collected every ten minutes for the first 300 minutes and then 600 minutes following O$_2$ addition.

4.3. Results and Analysis.

4.3.1. Formation of LLL-Ni^{II}-NCC under O$_2$-free conditions. Electronic absorption data following the formation of 0.75 mM LLL-Ni^{II}-NCC from free peptide and NiSO$_4$ under O$_2$-free conditions show a rise in absorption intensity in the visible and UV regions over time (Figure 4.2). The red spectrum was collected approximately two minutes after metal was added to NCC in O$_2$-free solutions and represents the earliest accumulated data point for complex
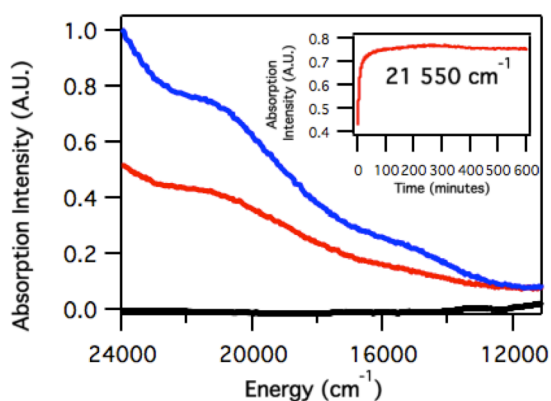
Figure 4.2. Electronic absorption spectra showing the formation of 0.75 mM LLL-Ni^{II}-NCC under O$_2$-free conditions in pH 7.3, 50 mM potassium phosphate buffer. The spectra include LLL-NCC without metal (black), Ni-NCC shortly following addition of NiSO$_4$ to LLL-NCC (red), and LLL-Ni^{II}-NCC incubated for ten hours (blue). Inset: absorption intensity at 21 550 cm^{-1} as a function of time.

formation. The absorption intensity at 21 550 cm^{-1} shows a rapid rise within the first minute of data collection and levels after 150 minutes (Figure 4.2, inset). Attempts to model the kinetics of formation of LLL-Ni^{II}-NCC from NiSO$_4\bullet$6H$_2$O and LLL-NCC to first-order or second-order rate equations were unsuccessful, which is not surprising given that complex formation likely involves more than one intermediate species. We had previously reported a drop in absorption intensity as LLL-Ni^{II}-NCC ages under atmosphere, which is associated with the chiral inversion

reaction.[3] No drop in absorption intensity is observed under these O_2-free conditions. Moreover, the extinction coefficient for O_2-free LLL-Ni^{II}-NCC is $\varepsilon_{21\ 550} = 1\ 000\ M^{-1}\ cm^{-1}$, which is substantially greater than that previously reported for O_2-exposed LLL-Ni^{II}-NCC ($\varepsilon_{21\ 550} = 300$).

4.3.2. Formation of LLL-Ni^{II}-NCC in the presence of O_2. Upon addition of NiSO$_4$ to NCC under an air atmosphere, the electronic absorption intensity rises rapidly to 0.75 AU within ten minutes (Figure 4.3), indicating the formation of LLL-Ni^{II}-NCC in ~96% yield, using the extinction coefficient determined above. After ten minutes of aging, the absorption intensity at this wavelength drops rapidly, eventually leveling to 0.25 AU by ~500 minutes (Figure 4.3). Assuming the chiral inversion of LLL-Ni^{II}-NCC is responsible for the drop in absorption intensity in the O_2-exposed sample, the inversion reaction proceeds rapidly following formation of the LLL-Ni^{II}-NCC specifically in the presence of O_2.
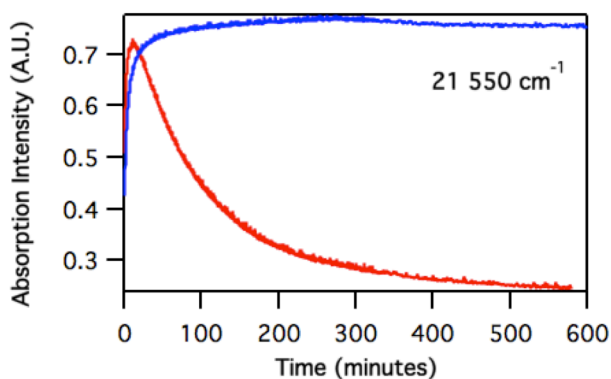
Figure 4.3. Single-energy (21 550 cm^{-1}) time profile of electronic absorption spectra of 0.75 mM LLL-Ni^{II}-NCC prepared O_2-free (blue) and O_2-exposed (red) in pH 7.3 potassium phosphate buffer.
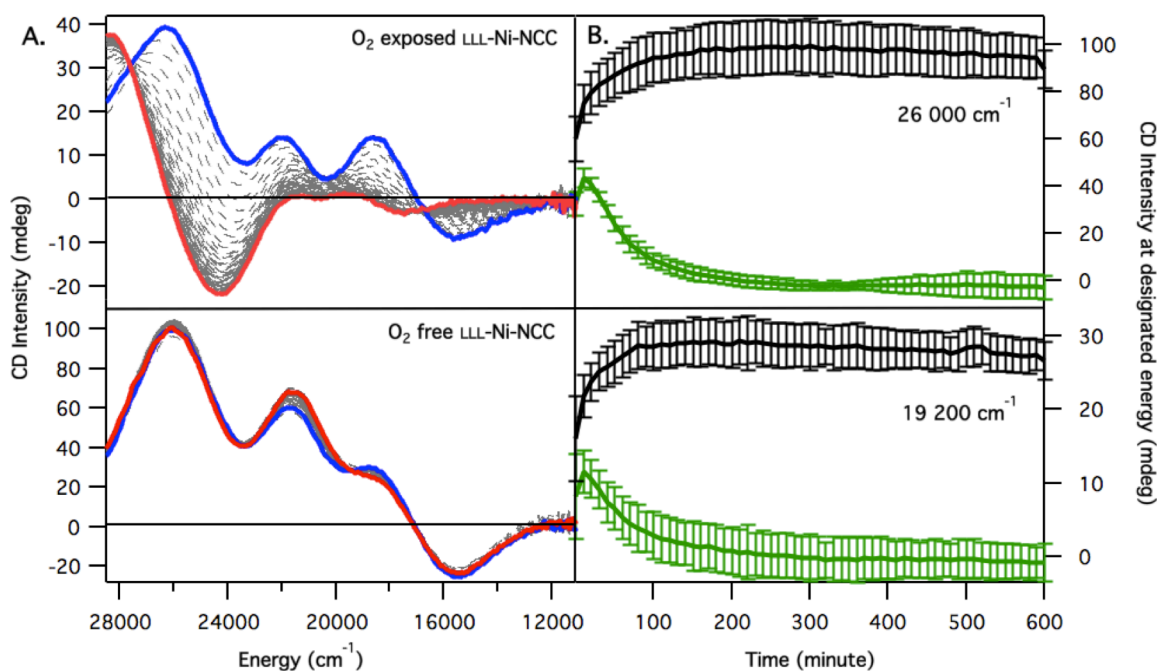
Figure 4.4. **A.** CD spectra of 0.75 mM LLL-Ni^{II}-NCC in pH 7.3 potassium phosphate buffer exposed to air (top) and purged with Ar (bottom). Blue spectra were obtained at the time the absorption spectra were at maximum intensity, indicating maximum LLL-Ni^{II}-NCC complex formation (t = 10 minutes for O$_2$-exposed and t = 150 minutes for O$_2$-free LLL-Ni^{II}-NCC), red spectra were collected at t = 590 minutes, and intermediate spectra obtained every ten minutes between these two times are represented as grey dashed traces. **B.** CD signal at single energies for 0.75 mM LLL-Ni^{II}-NCC incubated in O$_2$-free (black) and O$_2$-exposed (green) pH 7.3 potassium phosphate buffer. Error bars represent +/- one standard deviation from an average of three trials.

4.3.3. The chiral inversion reaction of LLL-Ni^{II}-NCC does not occur in the absence of

O$_2$. CD spectra of LLL-Ni^{II}-NCC aged for 600 minutes under argon and air atmospheres are

shown in Figure 4.4. Spectra taken at maximum formation (t = 10 minutes for O$_2$ exposed

samples, t = 150 minutes for O$_2$ free samples) are very similar but not identical. Both feature four

prominent CD signals at 15 500 (-), 19 200 (+), 23 800 (+) and 26 000 cm^{-1} (+). On the basis of a

previously performed deconvolution of electronic absorption and CD spectra, these CD

transitions are due to four *d-d* bands expected for a Ni^{II} ion in a square planar geometry with

2N:2S ligand environment and three S-Ni charge transfer (CT) transitions.[27] Starting at t = 0

88

seconds, some increase in band intensity is initially observed, especially at 16 300, 18 900, 22 200 and 26 500 cm^{-1}, in both O_2-free and O_2-exposed LLL-Ni^{II}-NCC, indicating complex formation (Figure 4.4B). Each band has a slightly different rate of change in formation (data not shown), likely because LLL-Ni^{II}-NCC formation from LLL-NCC and NiSO$_4$ is not a two-state process and involves one or more intermediates.

Consistent with our previous report, the time-progression CD spectra of O_2-exposed LLL-Ni^{II}-NCC demonstrate distinct sign changes without significant band shifting, indicating chiral inversion of LLL-Ni^{II}-NCC.[3] Major changes occur within the first 10 hours, where the absolute intensities of the bands at 16 000 and 23 000 cm^{-1} decrease, and negative bands form at ~ 17 000 and 24 000 cm^{-1}. This CD spectrum does not look like that previously reported for DLD-Ni^{II}-NCC, but instead resembles that of LLL-Ni^{II}-NCC after 24 hours of aging.[23] Therefore, this ten-hour aged species represents either an intermediate, or a mixture of intermediate species, formed en route to DLD-Ni^{II}-NCC.

In contrast, the CD spectra collected for LLL-Ni^{II}-NCC prepared under an argon atmosphere offer no evidence of chiral inversion. The O_2-free sample does demonstrate a change in CD signal within the 600-minute time frame; however, these changes occur within the first 150 minutes and only lead to an increase in absolute ellipticity (Figure 4.4B and 4.5); *i.e.,* no change in sign of any CD features is observed. For O_2-free LLL-Ni^{II}-NCC, the individual time traces level after 150 minutes (Figure 4.4B), consistent with the time scale for formation of LLL-Ni^{II}-NCC from 1:1 molar ratio of NiSO$_4$ and NCC, as established by the electronic absorption data described above. The intensities of the CD features for O_2-free LLL-Ni^{II}-NCC are approximately twice that of O_2-exposed LLL-Ni^{II}-NCC, suggesting that the CD spectrum of O_2-exposed LLL-Ni^{II}-NCC collected at t = 10 minutes has contributions from multiple species. The

CD spectrum for LLL-Ni^{II}-NCC prepared and aged under an Ar atmosphere therefore represents the authentic CD spectrum of LLL-Ni^{II}-NCC.
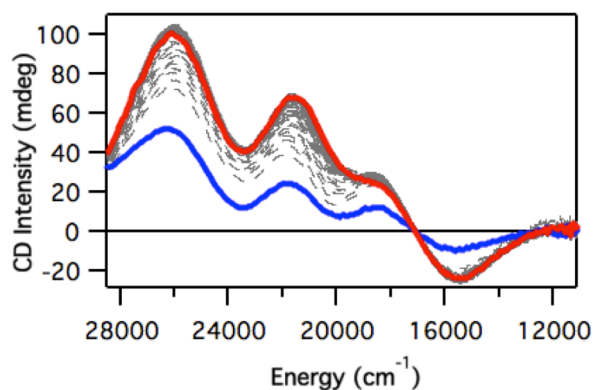
Figure 4.5. Full CD spectra of Ni-NCC prepared O$_2$-free and aged for 600 minutes. Spectra include those for the sample at approximately two minutes after complex formation (blue), after 600 minutes of incubation (red). Spectra collected every ten minutes between the red and blue spectra are represented as grey dashed traces.

4.3.4. Addition of O$_2$ to LLL-Ni^{II}-NCC prepared O$_2$-free induces the chiral inversion reaction. Conclusive evidence that O$_2$ causes the chiral inversion of LLL-Ni^{II}-NCC is provided by the observation of CD changes upon the addition of O$_2$ to O$_2$-free LLL-Ni^{II}-NCC. O$_2$ gas was added by a syringe to a sample of LLL-Ni^{II}-NCC that was prepared and incubated for 300 minutes under an Ar atmosphere to allow for maximum LLL-Ni^{II}-NCC formation. The CD spectrum of LLL-Ni^{II}-NCC prepared under an Ar atmosphere, then exposed to O$_2$ (Figure 4.6), evolves in the same way as the O$_2$-exposed sample (cf. Figures 4.5 and 4.4A, top), demonstrating that chiral inversion of LLL-Ni^{II}-NCC complex is completely dependent on O$_2$.
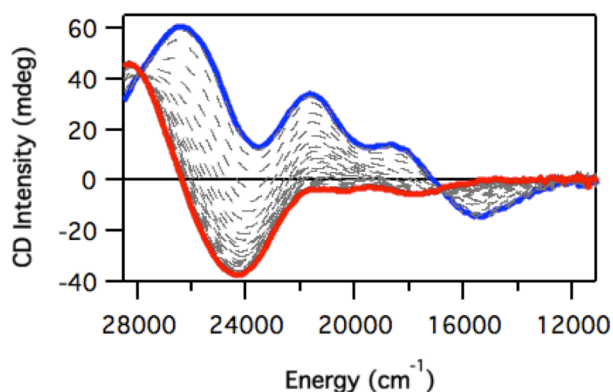
Figure 4.6. CD spectra of 0.75 mM LLL-Ni^{II}-NCC generated O$_2$-free and incubated 300 minutes to achieve maximum formation of LLL-Ni^{II}-NCC, then treated with O$_2$. The blue spectrum was collected at t = 300 minutes to allow for maximum complex formation, and then the sample was injected with O$_2$. The red spectrum was collected after 800 total minutes of incubation (600 minutes of O$_2$ exposure). Intermediate spectra obtained every ten minutes between these two times are represented as black dashed traces.

4.3.5. Superoxide is formed by LLL-Ni^{II}-NCC under an atmosphere of air. The nitro blue tetrazolium (NBT) assay was employed to determine if the chiral inversion reaction of LLL-Ni^{II}-NCC involves reduction of O$_2$ to superoxide by the Ni^{II} center. The assay detects formation of O$_2^-$, which oxidizes NBT to its four-electron oxidized species, diformazin, which absorbs strongly at 530 nm.[28] Solutions containing the Ni-NCC complex and NBT absorbed more strongly at 530 nm than the control reactions, indicating the generation of superoxide under these conditions. In addition, monitoring the absorption at 530 nm over the course of an hour showed an increase in diformazin production, suggesting that superoxide forms as LLL-Ni^{II}-NCC undergoes chiral inversion.

4.3.6. EPR spectroscopy provides evidence for formation of Ni^{III} in aging LLL-Ni-NCC. Perpendicular- and parallel-mode X-band EPR spectra collected for freshly prepared LLL-Ni^{II}-NCC samples at 123 K were completely featureless, consistent with the lack of Ni^{III} ions in these samples. However, data collected for duplicate samples aged approximately 10 minutes showed weak signals in a perpendicular-mode experimental, with g values consistent with Ni^{III} ($g_\perp$ = 2.20 and $g_\parallel$ = 2.05). Corresponding EPR data collected for duplicate samples aged 60 minutes showed the absence of this signal, indicating the consumption of the Ni^{III} species.

4.3.7. LLL-Ni^{II}-NCC forms two carbanion intermediates en route to chiral inversion. LLL-Ni^{II}-NCC was incubated with excess acetaldehyde in order to determine if the chiral inversion reaction generates a carbanion intermediate. Aldehydes are known to quench carbanion intermediates in solution and generate a product with a mass increase equal to that of the deprotonated aldehyde.[19,26,29-31] The reaction can be cleanly monitored using ESI-MS operated in positive ion mode. The spectra of LLL-Ni^{II}-NCC incubated with excess acetaldehyde over the course of a day clearly show both the free peptide (339 *m/z*) and NCC + 2 acetaldehydes (425 *m/z*) (Figure 4.7). These data indicate that over the course of 24 hours, two carbanion intermediates are formed per molecule of LLL-Ni^{II}-NCC. Therefore, each of the single chiral inversion reactions from LLL-Ni-NCC to DLD-Ni-NCC requires a carbanion intermediate.
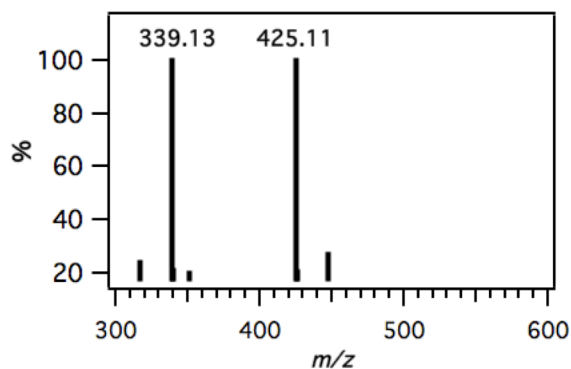
Figure 4.7. ESI-MS spectrum of Ni-NCC incubated with excess acetaldehyde. The major ions include 339.13 *m/z* (NCC) and 425.11 *m/z* (NCC + 2 acetaldehydes).

4.3.8. The chiral inversion reaction of LLL-Ni^{II}-NCC does not show first order rate dependence on hydroxide ion concentration. The chiral inversion of LLL-Ni^{II}-NCC was also followed for several different solution pH values, in order to determine the pH dependence of this reaction. The CD spectra of LLL-Ni^{II}-NCC aged in phosphate buffer at pH 7.3, pH 8.0, and pH 8.3 under an air atmosphere are shown in Figure 4.8A. For all three solutions, there is an initial increase in CD intensity, indicating LLL-Ni^{II}-NCC complex formation, followed by a change in sign of some CD signals, demonstrating the chiral inversion. Although the t = 0 spectra are not identical for the three different samples (Figure 4.8A, blue), they all feature the same CD bands at the same energies, but of different intensities. This could be attributed to slightly different rates of formation and/or chiral inversion. The dependence on pH of the rate of chiral inversion is shown in Figure 4.8B, which compares the change in CD signals with time for samples at pH 7.3 and 8.3. While there is a modest effect on the rate of change of the CD signal

93

with the pH of the solution, a first-order dependence in this pH range is not exhibited. Additional experiments at even more elevated pH (> 9.0) were performed, but the reproducibility of these results was poor. We speculate that when the solution pH is well outside the buffering capacity of phosphate, slight changes in the amount of LLL-NCC or Ni^{II} used in the experiment perturb the solution pH more significantly and therefore alter the aging progression profile of the complex. Nonetheless, these data collectively demonstrate there is a minor pH effect on the rate of chiral inversion.

To assess whether inversion can occur at elevated pH in the absence of O_2, CD spectra were collected for pH 9.0 LLL-Ni^{II}-NCC prepared and aged under an Ar atmosphere. Under these
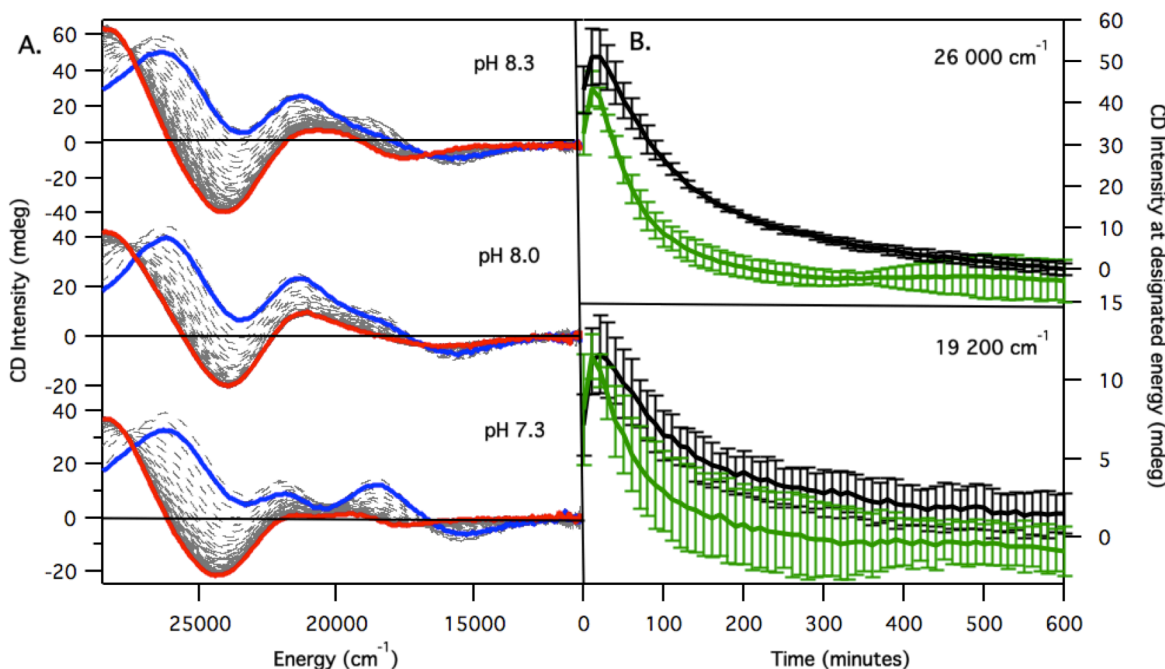
Figure 4.8. **A.** CD spectra of LLL-Ni^{II}-NCC in potassium phosphate buffer at pH 7.3 (bottom), pH 8.0 (middle), and pH 8.3 (top). Blue spectra were collected ~ 15 seconds after mixing, red spectra were acquired after 600 minutes of incubation, and intermediate spectra obtained every ten minutes between the two time points are represented as grey dashed traces. **B.** CD signal (mdeg) at designated single energies for pH 7.3 (green) and pH 8.3 (blue) potassium phosphate solutions. Error bars represent +/- one standard deviation from an average of three trials.

conditions, the only changes observed in the CD spectra are attributed to complex formation (Figure 4.9) there is no evidence for chiral inversion. Thus, regardless of whether the LLL-Ni^{II}-NCC is aged in neutral or basic solution, there is no chiral inversion observed in the absence of O_2.
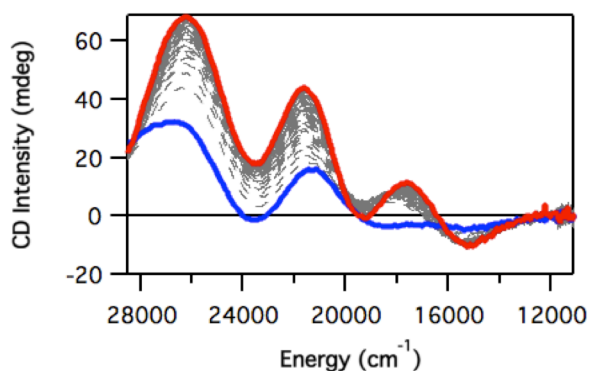
Figure 4.9. CD spectra of Ni-NCC in pH 9.0 potassium phosphate, prepared and aged O_2 free. Spectra were collected after ~ 2 minutes (blue), following 600 minutes incubation (red), and every ten minutes in between (dashed grey traces).

4.3.9. DLD-Ni^{II}-NCC shows time-dependent CD changes. The changes in the CD spectra of DLD-Ni^{II}-NCC aged under an Ar atmosphere are consistent with complex formation (Figure 4.10, bottom). The final spectrum, however, is distinct from that previously reported for DLD-Ni^{II}-NCC.[3] Specifically, in the current spectrum, there is an additional positive feature at 17 000 cm^{-1} not previously observed. Intriguingly, the intensity of this positive feature decreases over time in the O_2-exposed sample (Figure 4.10, top). Thus, CD data collected for DLD-Ni^{II}-NCC in the presence of O_2 are consistent with some extent of racemization, or a secondary reaction. These changes were not detected in the previous study because these modifications happened during the time-course of sample preparation. The ten-hour CD spectrum of O_2-

exposed DLD-Ni^{II}-NCC, however, is essentially identical to that previously reported for aged, O$_2$-exposed LLL-Ni^{II}-NCC. Thus, both LLL-, and DLD-Ni^{II}-NCC proceed to the same end point.
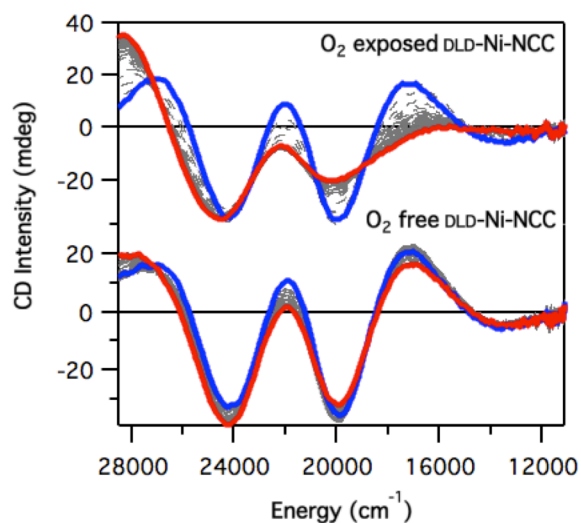

Figure 4.10. CD spectra of DLD-Ni^{II}-NCC generated in pH 7.3 potassium phosphate buffer and prepared and aged in the absence (bottom) and presence (top) of O$_2$. Spectra were collected at t = 0 minutes (blue), t = 600 minutes (red), and every ten minutes in between (dashed grey traces).

Electronic absorption data collected for O$_2$-free and O$_2$-exposed DLD-Ni^{II}-NCC reinforce the CD data. In the absence of O$_2$, the electronic absorption intensity of DLD-Ni^{II}-NCC at 22 550 cm^{-1} is essentially constant at 0.43 AU (ε = 570 M^{-1}cm^{-1}) over the course of 600 minutes (Figure 4.8). In contrast, in the O$_2$-exposed sample, the absorption intensity at 22 550 cm^{-1} decreases rapidly from 0.40 to 0.20 AU, largely within 100 minutes.
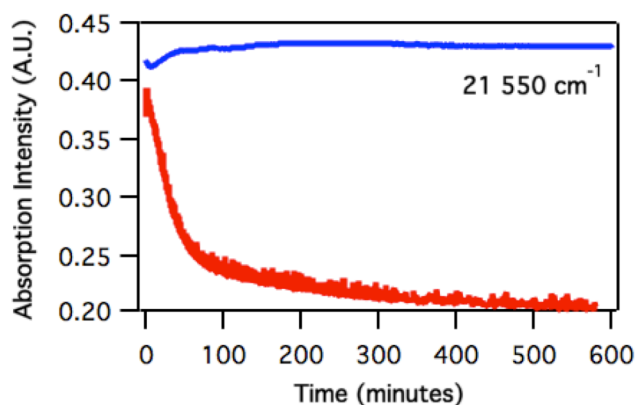
Figure 4.11. Single-energy time profile of electronic absorption spectra of DLD-Ni^{II}-NCC prepared and aged O$_2$-free (blue) and O$_2$-exposed (red) in pH 7.3 potassium phosphate buffer.

4.3.10. DLL-Ni^{II}-NCC shows time-dependent CD changes. When prepared under an Ar atmosphere, DLL-Ni^{II}-NCC shows CD changes essentially identical to those of LLL-Ni^{II}-NCC (cf. Figures 4.4A and 4.9). In both cases, a negatively-signed band at ~15 500 cm^{-1} and positive features at 19 200, 23 800, and 26 000 cm^{-1} gain intensity. These spectral changes are consistent with full formation of DLL-Ni^{II}-NCC and offer no evidence of chiral inversion. However, when DLL-Ni^{II}-NCC is formed under an air atmosphere, changes in CD signal are observed over the course of 600 minutes (Figure 4.12, top), consistent with chiral inversion. Specifically, the spectrum collected for DLL-Ni^{II}-NCC after 600 minutes of aging under air is very similar to that of O$_2$-exposed DLD-Ni^{II}-NCC at 600 minutes (Figure 4.10, top).
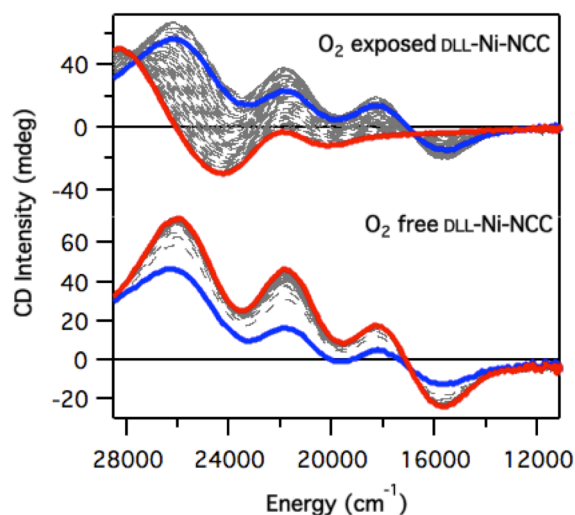
Figure 4.12. CD spectra of DLL-Ni^{II}-NCC generated in pH 7.3 potassium phosphate buffer and prepared and aged in the absence (bottom) and presence (top) of O$_2$. Spectra were collected at t = 0 minutes (blue), t = 600 minutes (red), and every ten minutes in between (dashed grey traces).

4.3.11. LLD-Ni-NCC undergoes spectral changes, even in the absence of O$_2$. In the absence of O$_2$, the initial CD spectra of LLD-Ni^{II}-NCC look strikingly similar to those of DLD-Ni^{II}-NCC with a positive band at ~17 000 cm^{-1} and negative bands at ~20 000 and 24 500 cm^{-1} (cf. Figures 4.10 and 4.7). When CD data are collected for LLD-Ni^{II}-NCC under an atmosphere of air, the CD features at ~17 000, 20 000, and 24 000 cm^{-1} lose intensity, with the lowest energy band completely losing CD intensity. Unlike both LLL- and DLD-Ni^{II}-NCC, LLD-Ni^{II}-NCC shows spectral changes even in the absence of O$_2$ (Figure 4.13, bottom). Given the nature of these spectral changes, this may indicate that the LLD-Ni^{II}-NCC has a propensity for a secondary, non-oxygen-dependent reaction.
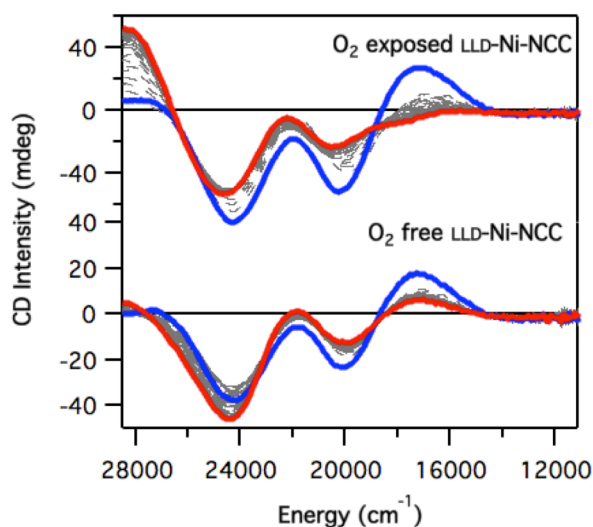
Figure 4.13. CD spectra of LLD-Ni^{II}-NCC generated in pH 7.3 potassium phosphate buffer prepared and aged in the absence (bottom) and presence (top) of O$_2$. Spectra were collected at t = 0 minutes (blue), t = 600 minutes (red), and every ten minutes in between (dashed grey traces).

4.4. Discussion.

Optically active amino acids and peptides are known to undergo racemization in aqueous solution in the absence of metal at temperatures above 100 ^{o}C and at pH values above 8 and below 5.[32] Binding of a transition metal to the residues allows the process to occur under milder conditions.[15-21] Metal-bound peptides are able to undergo racemization over the course of hours to days at temperatures between 35 and 40 ^{o}C and at a pH above 9. In both cases, the racemization or chiral inversion proceeds by deprotonation of an alpha hydrogen. Re-protonation by solvent gives either the D- or L-isomer.[20] Coordination of the amino acid or peptide to a metal center renders the deprotonation event more thermodynamically favorable,[15] leading to racemization or chiral inversion under milder conditions. In most cases where metal-facilitated

chiral inversion occurs instead of racemization, steric factors promote the formation of the D-isomer over the L-form.[19,33]

In addition to promoting racemization or inversion, the coordination of peptides to metals is also known to facilitate peptide degradation and/or oxidation.[19] One example of this is the nickel(II) complex of the tripeptide glycine-glycine-L-histidine, Ni[II]-GGH.[11,34,35] Ni[II]-GGH has been well-studied for its ability to catalyze site-specific oxidation and cleavage of DNA, as well as peptide cross-linking.[14] However, oxidation of Ni[II]-GGH by O_2 generates Ni[III]-GGH, which undergoes spontaneous decarboxylation at the C-terminus of the peptide.[34,36] The decarboxylated product undergoes further reactions including hydroxylation and racemization.[34] Additional Ni[III]-mediated reactivity in peptides includes ligand oxidation and disulfide bond formation/peptide crosslinking.[14]

4.4.1. O_2-dependent chiral inversion of Ni-NCC. In the absence of O_2, LLL-Ni[II]-NCC forms rapidly from $NiSO_4$ and NCC, and this complex is stable for at least ten hours, showing no evidence of inversion or secondary reactions, even at pH 9.0. This is in contrast to other square planar Ni[II]-peptide complexes that readily undergo base-catalyzed, metal-facilitated racemization at pH $\geq$ 9 over the course of several hours to days.[16,21,37] We attribute the lack of chiral inversion in LLL-Ni[II]-NCC under anaerobic conditions to the presence of two anionic cysteinate ligands and one anionic amide ligand (Figure 4.1). Charge donation from these ligands is expected to reduce the Lewis acidity of the Ni[II] center, mitigating the ability of the metal to promote deprotonation of the Cα−H groups. A complementary rationale is that the anionic ligands, along with the deprotonated carboxylate group, give Ni[II]-NCC an overall charge of -2, which would disfavor deprotonation on electrostatic grounds. This same behavior is observed for DLD-Ni[II]-NCC, which is also unchanged for at least ten hours when under an Ar atmosphere.

In the presence of O_2, LLL-Ni^{II}-NCC shows fairly rapid spectroscopic changes that are consistent with inversion (or racemization) of the NCC peptide. On the basis of trapping experiments with acetaldehyde, two carbanions are formed during the O_2-dependent inversion. Studies of the inversion reaction at pH 7.3 − 8.3 reveal a minor increase in the rate of inversion as the pH is increased. These data are consistent with inversion proceeding by Cα−H deprotonation, but this deprotonation does not occur for LLL-Ni^{II}-NCC prepared in the absence of O_2. In addition, another step must impact the rate of inversion more significantly than Cα−H deprotonation. The evidence for superoxide formation, as well as the O_2 dependence of this reaction, suggest that LLL-Ni^{II}-NCC reacts with O_2 to form superoxide and LLL-Ni^{III}-NCC. We propose the higher oxidation state Ni^{III} center promotes Cα−H deprotonation, leading to inversion (or racemization) for LLL-Ni^{III}-NCC upon reprotonation. Subsequent reaction of superoxide, or some alternative reductant, with Ni^{III}-NCC, would regenerate the Ni^{II} complex. Perpendicular-mode X-band EPR spectra collected for frozen aliquots of LLL-Ni^{II}-NCC during the aging process showed a very weak feature, the position and line shape of which are consistent with a Ni^{III} center ($g\perp = 2.20$ and $g\| = 2.05$), albeit in very low concentration.

4.4.2. Pathway to chiral inversion in Ni-NCC. In the presence of oxygen, LLL-Ni^{II}-NCC evolves to give a CD spectrum most similar to that of DLD-Ni^{II}-NCC. The same behavior is observed for DLL- and LLD-Ni^{II}-NCC. Thus, regardless of the initial isomer, all species show a final CD spectrum most similar to that of DLD-Ni^{II}-NCC. This directed inversion was previously rationalized on the basis of DFT-computed energies of models of Ni^{II}-NCC (Scheme 4.1).[3] In this current study, we show that even DLD-Ni^{II}-NCC evolves over time when exposed to O_2, although the change is significantly more minor than that observed for LLL-Ni^{II}-NCC (cf. Figures 4.7 and 4.4), indicating existence of a secondary reaction.

Scheme 4.1. Pathway to chiral inversion in Ni-NCC, with DFT-computed relative energies of each model shown. All energy values are given relative to that of LLL-Ni^{II}-NCC, whose energy is defined as 0 kcal/mol.
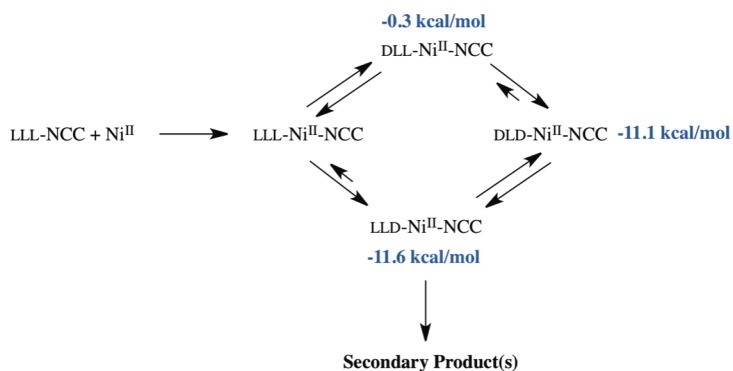
According to the DFT-computed energies (Scheme 4.1), the inversion of Asn1 results in very little change in energy, whereas inversion of Cys3 leads to a stabilization of ~11 kcal/mol. (We note that the accuracy of DFT-computed energies at this level of theory is ~3-5 kcal/mol.) It would be tempting to propose that the spectral changes observed for DLD-Ni^{II}-NCC are due to its racemization to a mixture of DLD-Ni^{II}-NCC and LLD-Ni^{II}-NCC. However, the final CD spectrum cannot be reproduced by addition of the CD spectra of authentic (*i.e.*, O$_2$-free) LLD- and DLD-Ni^{II}-NCC in different proportions. In particular, CD spectra of LLD- and DLD-Ni^{II}-NCC show a prominent positive band at ~17 000 cm^{-1}, whereas this band disappears with time in the O$_2$-exposed samples (Figures 4.7 and 4.9). Intriguingly, LLD-Ni^{II}-NCC shows some spectral changes in the absence of O$_2$, suggesting that this isomer may be reactive even in the Ni^{II} oxidation state. The O$_2$-dependent conversion of DLD-Ni^{II}-NCC to LLD-Ni^{II}-NCC, followed by the formation of some secondary product from the latter complex, could account for the spectral changes observed for O$_2$-exposed DLD-Ni^{II}-NCC. Thus, the likely endpoint in the cycle shown in Scheme

4.1 is DLD-Ni^{II}-NCC in the presence of an intermediate or secondary product that represent a small population of the sample.

The time-progression of the CD and electronic absorption spectra of LLL-Ni^{II}-NCC indicate the accumulation of an intermediate after 10 hours of incubation with metal. The CD spectrum of this intermediate is identical to that of the 24-hour intermediate we described previously,[3] and is nearly featureless below 22 000 cm^{-1} (cf. Figures 4.1B and 4.4B). This intermediate is not a singly-inverted species, as the CD spectra collected for authentic DLL- and/or LLD-Ni^{II}-NCC are quite different than the corresponding spectrum of the 10-hour intermediate. Attempts to reproduce the CD spectrum of the 10-hour intermediate via spectral combinations of different proportions of authentic (*i.e.*, O$_2$-free) LLL-, DLL-, LLD- and DLD-Ni^{II}-NCC were unsuccessful. Specifically, the CD spectra of LLD- and DLD-Ni^{II}-NCC both show a positive band at ~17 000 cm^{-1} whereas those of DLL-Ni^{II}-NCC and LLL-Ni^{II}-NCC have a negative band at ~16 000 cm^{-1}. Therefore, the lower-energy features, although varied in sign, are significantly shifted such that they do not cancel each other out to make the spectrum appropriately featureless below 21 000 cm^{-1}. This suggests that the 10-hour-aged intermediate is not simply a mixture of various chiral forms of Ni^{II}-NCC.

Another possible assignment of the ten-hour aged intermediate is a Ni^{II}-form of NCC where Cys3 has dissociated from the Ni^{II} center to give a "Cys3-off" configuration. The CD spectra of authentic (*i.e.*, O$_2$-free) LLD-, and DLD-Ni^{II}-NCC both show a positive band at ~17 000 cm^{-1} (Figures 4.10, bottom and 4.13, bottom), whereas the CD spectra of LLL-, and DLL-Ni^{II}-NCC show a negative feature near this energy (at ~16 000 cm^{-1}; Figures 4.4A, bottom and 4.12, bottom). Therefore, the band at 17 000 cm^{-1} is directly related to the chiral state of Cys3. Therefore, removal of a thiolate ligand could account for the lack of significant CD spectral

features below 21 000 cm^{-1}. Considering the structure of LLL-Ni^{II}-NCC (Figure 4.1), it is expected that the inversion of Cys3 would not occur without dissociation of this cysteinate ligand. Thus, it appears reasonable that the CD spectrum of the ten-hour aged species has contributions from a species where Cys3 has dissociated from the Ni^{II} center. This "Cys3-off" form of Ni^{II}-NCC could also offer a potential route to the secondary reactions of the complex. Attempts to react the complex with thiol-modifying reagents, however, produced no direct evidence of the "Cys-off" state, suggesting that, if this state does form, it is transient and/or present in very low amounts. For the related enzyme Ni-SOD, removal of one Cys ligand by site-directed mutagenesis led to the lack of any sulfur coordination and the formation of a high-spin ($S = 1$) Ni^{II} protein.[40] We note that ^{1}H-NMR experiments on Ni^{II}-NCC have been hampered by the presence of a minor paramagnetic component, which, on the basis of low-temperature, variable-temperature, variable-field magnetic circular dichroism (VTVH MCD) data was assigned to a high-spin Ni^{II} component that represented less than 1% of the sample under the conditions of the VTVH MCD experiment.[25]

4.4.3. Implications of the controlled reactivity in Ni^{II}-NCC. The data presented herein underscore the specific and unique reactivity of the Ni^{II}-NCC complexes in the absence of O$_2$, as well as their complex chemistry when O$_2$ is available to react with the Ni^{II} center. Superoxide is formed initially during oxygen-dependent chiral inversion, but once inversion occurs, the complex presumably performs anti-oxidant chemistry, scavenging superoxide. Oxidation to the Ni^{III} form initiates a cascade of reactions that convert the bulk of the sample to DLD-Ni^{II}-NCC and some secondary products. These results have important implications both for controlled reactivity of molecules with biotechnology applications, as well as understanding the diverse chemistry of redox-active, nickel-dependent metalloenzymes. The preferred coordination

geometry of a low-spin, thiolate-bound Ni^{II} center is different than that of a Ni^{III} ion (square planar versus distorted octahedral geometry). Thus, the Ni^{III} forms of nickel-peptide complexes must be stabilized in a different fashion than the Ni^{II} centers to prevent undesired secondary or peptide-modifying reactions. This is a significant challenge, as underscored by the general lack of Ni^{III}-peptide complexes, and the complex reactivity of Ni^{III}-peptides that involves decarboxylation and ligand oxidation reactions. [11,13,17,34-36,39-48] In order for Ni^{II} complexes to be properly used for biotechnology applications, either the Ni^{III} form must be sufficiently stabilized so as to prevent secondary reactions, or the reactivity of the Ni^{II} center with O_2 must be controlled. The Ni-NCC system exhibits far greater stability and reaction specificity than other nickel-peptide systems, making it potentially useful in a variety of applications.

In addition to the relevance of this work to metallopeptides, these results also provide insights into the controlled reactivity of redox-active, Ni-dependent enzymes that feature Ni^{III} centers. Specifically, these proteins must modulate the reactivity of the potentially more reactive Ni^{III} states to prevent detrimental side reactions in biology. In Ni-SOD, metal oxidation is coupled to a change in the coordination environment around the metal center. Specifically the square planar 2N:2S geometry of Ni^{II}-SOD converts to square pyramidal 3N:2S geometry in Ni^{III}-SOD through the axial ligation of a histidine residue.[49,50] Histidine coordination has been proposed to serve several functions, including tuning the reduction potential of the Ni center.[27,49] Axial histidine ligation to the Ni^{III} center may also serve to prevent any side-reactions for Ni^{III}-SOD.

4.5. Conclusions.

The research presented here shows that incorporation of Ni[II] into the LLL-NCC peptide occurs very rapidly and does not undergo chiral inversion in the absence of dioxygen. It further demonstrates that site-specific chiral inversion of LLL-Ni[II]-NCC to DLD-Ni[II]-NCC specifically depends on O_2. The chiral inversion reaction produces superoxide and likely proceeds via a Ni[III] intermediate to generate the DLD-Ni[II]-NCC product. Due to the specificity of the chiral inversion reaction and stability of the complex, this system is amenable to use as a catalyst in biotechnology and industrial applications.

4.6. References.

(1)   Bal, W.; Chmurny, G. N.; Hilton, B. D.; Sadler, P. J.; Tucker, A. *J. Am. Chem. Soc.* **1996**, *118*, 4727-4728.

(2)   Burrows, C. J.; Perez, R. J.; Muller, J. G.; Rokita, S. E. *Pure Appl. Chem.* **1998**, *70*, 275-278.

(3)   Krause, M. E.; Glass, A. M.; Jackson, T. A.; Laurence, J. S. *Inorg. Chem.* **2011**, *50*, 2479-2487.

(4)   Krężel, A.; Kopera, E.; Protas, A. M.; Poznański, J.; Wysłouch-Cieszyńska, A.; Bal, W. *J. Am. Chem. Soc.* **2010**, *132*, 3355-3366.

(5)   Liang, Q.; Eason, P. D.; Long, E. C. *J. Am. Chem. Soc.* **1995**, *117*, 9625-9631.

(6)   Lioe, H.; Duan, M.; O'Hair, R. A. J. *Rapid Commun. Mass Spectrom.* **2007**, *21*, 2727-2733.

(7)   Shullenberger, D. F.; Eason, P. D.; Long, E. C. *J. Am. Chem. Soc.* **1993**, *115*, 11038-11039.

(8)   Splith, K.; Neundorf, I.; Hu, W. N.; N'Dongo, H. W. P.; Vasylyeva, V.; Merz, K.; Schatzschneider, U. *Dalton Trans.* **2010**, *39*, 2536-2545.

(9)   Shearer, J.; Long, L. M. *Inorg. Chem.* **2006**, *45*, 2358-2360.

(10)   Rabanal, F.; DeGrado, W. F.; Dutton, P. L. *J. Am. Chem. Soc.* **1996**, *118*, 473-474.

(11)   Bal, W.; Djuran, M. I.; Margerum, D. W.; Gray, E. T.; Mazid, M. A.; Tom, R. T.; Nieboer, E.; Sadler, P. J. *J. Chem. Soc. Chem. Comm.* **1994**, 1889-1890.

(12)   Gale, E. M.; Narendrapurapu, B. S.; Simmonett, A. C.; Schaefer, H. F.; Harrop, T. C. *Inorg. Chem.* **2010**, *49*, 7080-7096.

(13)   Haas, K.; Dialer, H.; Piotrowski, H.; Schapp, J.; Beck, W. *Angew. Chem., Int. Ed.* **2002**, *41*, 1879.

(14)   Ross, S. A.; Burrows, C. J. *Inorg. Chem.* **1998**, *37*, 5358-5363.

(15)   Williams, D. H.; Busch, D. H. *J. Am. Chem. Soc.* **1965**, *87*, 4644.

(16)   Buckingham, D. A.; Marzilli, L. G.; Sargeson, A. M. *J. Am. Chem. Soc.* **1967**, *89*, 5133.

(17)   Fujioka, M.; Nakao, Y.; Nakahara, A. *Bull. Chem. Soc. Jpn.* **1976**, *49*, 477-479.

(18)   Gillard, R. D.; Phipps, D. A. *J. Chem. Soc. Chem. Comm.* **1970**, 800-&.

(19)   Pasini, A.; Casella, L. *J. Inorg. Nucl. Chem.* **1974**, *36*, 2133-2144.

(20)   Stadtherr, L. G.; Angelici, R. J. *Inorg. Chem.* **1975**, *14*, 925-930.

(21)   Smith, G. G.; Khatib, A.; Reddy, G. S. *J. Am. Chem. Soc.* **1983**, *105*, 293-295.

(22)   Krause, M. E.; Glass, A. M.; Jackson, T. A.; Laurence, J. S. *Inorg. Chem.* **2010**, *49*, 362-364.

(23)   Kruger, H. J.; Peng, G.; Holm, R. H. *Inorg. Chem.* **1991**, *30*, 734-742.

(24)   Grapperhaus, C. A.; Darensbourg, M. Y. *Acc. Chem. Res.* **1998**, *31*, 451-459.

(25)   Mirza, S. A.; Pressler, M. A.; Kumar, M.; Day, R. O.; Maroney, M. J. *Inorg. Chem.* **1993**, *32*, 977-987.

(26)   Berndt, D. C. *J. Org. Chem.* **1970**, *35*, 1129-1131.

(27)   Fiedler, A. T.; Bryngelson, P. A.; Maroney, M. J.; Brunold, T. C. *J. Am. Chem. Soc.* **2005**, *127*, 5449-5462.

(28)   Auclair, C.; Voisin, E. *CRC Handbook of Methods for Oxygen Radical Research*; CRC Press, 1985.

(29)   Belokon, Y. N.; Bulychev, A. G.; Vitt, S. V.; Struchkov, Y. T.; Batsanov, A. S.; Timofeeva, T. V.; Tsyryapkin, V. A.; Ryzhov, M. G.; Lysova, L. A.; Bakhmutov, V. I.; Belikov, V. M. *J. Am. Chem. Soc.* **1985**, *107*, 4252-4259.

(30)   Casella, L.; Pasini, A.; Ugo, R.; Visca, M. *J. Chem. Soc. Dalton* **1980**, 1655-1663.

(31)   Teo, S. B.; Teoh, S. G. *Inorg. Chim. Acta Lett.* **1980**, *44*, L269-L270.

(32)   Bada, J. L. *J. Am. Chem. Soc.* **1972**, *94*, 1371-1373.

(33)   Job, R.; Bruice, T. C. *Journal of the Chemical Society-Chemical Communications* **1973**, 332-333.

(34)   Green, B. J.; Tesfai, T. M.; Margerum, D. W. *Dalton Trans.* **2004**, 3508-3514.

(35)   Green, B. J.; Tesfai, T. M.; Xie, Y.; Margerum, D. W. *Inorg. Chem.* **2004**, *43*, 1463-1471.

(36)   Tesfai, T. M.; Green, B. J.; Margerum, D. W. *Inorg. Chem.* **2004**, *43*, 6726-6733.

(37)   Keyes, W. E.; Caputo, R. E.; Willett, R. D.; Legg, J. I. *J. Am. Chem. Soc.* **1976**, *98*, 6939-6945.

(38)   Johnson, O. E.; Ryan, K. C.; Maroney, M. J.; Brunold, T. C. *J. Biol. Inorg. Chem.* **2010**, *15*, 777-793.

(39)   Subak, E. J.; Loyola, V. M.; Margerum, D. W. *Inorg. Chem.* **1985**, *24*, 4350-4356.

(40)   Bossu, F. P.; Margerum, D. W. *J. Am. Chem. Soc.* **1976**, *98*, 4003-4004.

(41)   Bossu, F. P.; Paniago, E. B.; Margerum, D. W.; Kirksey, S. T.; Kurtz, J. L. *Inorg. Chem.* **1978**, *17*, 1034-1042.

(42)   Farmer, P. J.; Solouki, T.; Mills, D. K.; Soma, T.; Russell, D. H.; Reibenspies, J. H.; Darensbourg, M. Y. *J. Am. Chem. Soc.* **1992**, *114*, 4601-4605.

(43)   Gale, E. M.; Cowart, D. M.; Scott, R. A.; Harrop, T. C. *Inorg. Chem.* **2011**, *50*, 10460-10471.

(44)   Kirksey, S. T.; Neubecker, T. A.; Margerum, D. W. *J. Am. Chem. Soc.* **1979**, *101*, 1631-1633.

(45)   Lappin, A. G.; Murray, C. K.; Margerum, D. W. *Inorg. Chem.* **1978**, *17*, 1630-1634.

(46)   Murray, C. K.; Margerum, D. W. *Inorg. Chem.* **1983**, *22*, 463-469.

(47)   Owens, G. D.; Phillips, D. A.; Czarnecki, J. J.; Raycheba, J. M. T.; Margerum, D. W. *Inorg. Chem.* **1984**, *23*, 1345-1353.

(48)   Paniago, E. B.; Weatherb.Dc; Margerum, D. W. *J. Chem. Soc. Chem. Comm.* **1971**, 1427.

(49)   Barondeau, D. P.; Kassmann, C. J.; Bruns, C. K.; Tainer, J. A.; Getzoff, E. D. *Biochemistry* **2004**, *43*, 8038-8047.

(50)   Wuerges, J.; Lee, J. W.; Yim, Y. I.; Yim, H. S.; Kang, S. O.; Carugo, K. D. *Proc. Natl. Acad. Sci. U. S. A.* **2004**, *101*, 8569-8574.

Chapter 5: XAS structural characterization of Ni^{II}-NCC

5.1. Introduction.

The metal abstraction peptide tag (MAP-tag) asparagine-cysteine-cysteine (NCC) binds Ni^{II} tightly at neutral pH.[1] Metal-peptide complexes are of biotechnological interest, as they are capable of effecting site-specific DNA and protein cleavage as well as serving as drug delivery vehicles.[2-9] However, a detailed understanding of the electronic and geometric structures, as well as controlled reactivity, are desirable for these complexes to be used in biological systems where solution conditions are not as easily manipulated as in the laboratory.

The dianionic nickel(II) tripeptide complex of NCC, ([Ni-NCC]$^{2-}$; Ni-NCC) is both a structural and functional mimic of the radical scavenging enzyme nickel superoxide dismutase (Ni-SOD).[10] In the absence of crystallographic data, electronic absorption, CD, MCD, and VTVH MCD spectroscopies were used in combination with density functional theory (DFT), and time-dependent DFT (TD-DFT) computations to generate an experimentally geometric structure of the complex (Figure 5.1).[10] In addition to its biomimetic activity, Ni-NCC also undergoes O$_2$-
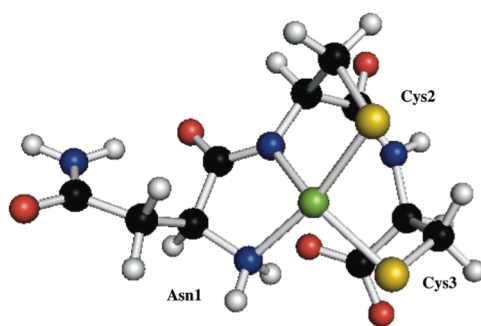
Figure 5.1. Structure of LLL-Ni^{II}-NCC.

dependent, site-specific chiral inversion to convert from LLL-Ni^{II}-NCC to DLD-Ni^{II}-NCC.[1,11] Due

to the reactivity and rearrangement of the complex the growth of crystals suitable for X-ray diffraction (XRD) analysis has not yet been possible.

We have recently discovered that the conversion of LLL-Ni^{II}-NCC to DLD-Ni^{II}-NCC only occurs in the presence of O_2 over the course of days to weeks.[11] Before the final state is achieved, an intermediate accumulates after ten hours of incubation with metal in the LLL-Ni^{II}-NCC, air exposed complex. This intermediate does not form in the O_2-free LLL-Ni^{II}-NCC sample. Although it has yet to be identified, the ten-hour intermediate is likely a mixture of two or more species in solution. In addition, although we originally concluded that the DLD-Ni^{II}-NCC complex was the final state of the chiral inversion reaction of Ni-NCC, further analysis has shown that DLD-Ni^{II}-NCC also undergoes some O_2-dependent reactivity. Like LLL-Ni^{II}-NCC, DLD-Ni^{II}-NCC is unreactive in the absence of O_2.

X-ray absorption spectroscopy (XAS) offers the advantage over XRD in that XAS does not require crystallization of the molecule to be analyzed; yet both techniques give bond distance information.[12] Therefore, amorphous solids and even solutions can be analyzed with XAS. In addition, both electronic and geometric structural information can be obtained from XAS, as different regions of the XAS spectrum contain different information about the complex studied. XAS involves irradiating a sample with X-rays of the appropriate energy to eject a core electron from the absorbing atom (absorber). The edge energy is specific for both the absorbing atom and the energy level from which the core electron is ejected, designated by its principal quantum number, n. For example, K-edge XAS removes a 1s electron from the absorbing atom. In inorganic complexes, the absorber is typically the metal center. The ejected photoelectron encounters the electron densities of the surrounding atoms, which are called scatterers, and then

the photoelectron is back-scattered to the absorber. Because the edge energy is equivalent to the ionization potential of the absorbing atom, the technique is very atom specific.

There are three main regions of an XAS spectrum. The pre-edge is the relatively low absorption intensity section before the edge. Because transitions of electrons bound to the absorbing atom (therefore called bound electronic transitions) are observed at these energies, the same selection rules as those in electronic absorption spectroscopy apply. Namely, the transition must be both electric dipole- and spin-allowed. Consequently, the pre-edge region is sensitive to the geometry and ligand field about the metal center and can feature transitions from a core orbital to higher-energy unoccupied orbitals of the appropriate symmetry. The edge is evidenced by a sharp rise in absorption intensity and its energy is dependent on the identity of the absorber as well as its oxidation state and ligand environment. Analysis of the near-edge region is called X-ray absorption near-edge structure (XANES). Lastly, the extended X-ray absorption fine structure (EXAFS) region of the XAS spectrum features wave oscillations due to interactions of the ejected photoelectron with its own backscattered waves. Analysis of the EXAFS oscillations gives distance information (frequency), coordination number (amplitude) and type of atom (phase shift).[12]

Our electronic structure calculations, along with circular dichroism (CD) and electronic absorption spectroscopies, predict that the structure of Ni-NCC is square planar Ni^{II} with *cis* deprotonated thiolates and a mixed nitrogen environment with one amine and one deprotonated amide. As mentioned above, this structure is identical to that of the first coordination sphere in Ni-SOD and, indeed, the electronic absorption transitions are very similar between the two, with less than 2 000 cm^{-1} shifts in all of the transition energies between 16 000 and 30 000 cm^{-1}.

In this work, we analyzed solution samples of O_2-free and O_2-exposed LLL-Ni^{II}-NCC and DLD-Ni^{II}-NCC using XAS in order to gain structural insight. Results verify that the structure of LLL-Ni^{II}-NCC is square planar, Ni^{II} with a 2N:2S coordination environment, like Ni-SOD. In addition, fits of the EXAFS data, as well as comparison of the pre-edge energies, show that all four complexes have similar structures, with subtle differences in the distribution of bond distances.

5.2. Experimental.

5.2.1. Preparation of O_2-exposed samples. LLL-NCC (GenScript) and DLD-NCC (NeoBioSci) were purchased as lyophilized powders, and stored desiccated at -20 ^{o}C when not in use. 3 mM NCC was reconstituted with pH 7.4 50 mM potassium phosphate buffer, generated from dibasic potassium phosphate (Fisher) and pH adjusted with solutions of KOH and/or HCl. Following dissolution, 1.0 molar equivalent of NiSO$_4$•6H$_2$O (Fisher) in deionized water was added, and the solution was inverted to ensure good mixing. The 3 mM Ni^{II}-NCC samples were allowed to incubate at room temperature in a sealed microcentrifuge tube under an atmosphere of air for ten hours. The ten-hour intermediate was transferred via a gastight syringe and needle into a Delrin or Lexan (McMaster Carr) XAS sample holder surrounded by Kapton tape and flash frozen in liquid nitrogen.

5.2.2. Preparation of O_2-free samples. LLL-NCC or DLD-NCC was reconstituted in pH 7.4 50 mM potassium phosphate buffer and transferred to a cuvette with ground glass opening that was stoppered with a Suba-Seal septum and further sealed with parafilm. NiSO$_4$•6H$_2$O prepared in water was placed into a small vial secured with a septum and also sealed with parafilm. The two samples were purged with 99.5% Ar that was itself purified by passage through columns of activated BASF catalyst and molecular sieves for 20 – 30 minutes to remove

O_2. 1.0 equivalent of Ar-purged $NiSO_4$ $6H_2O$ in water was then transferred to the NCC solution using a gastight syringe. The septum was sealed with parafilm, the solution slowly agitated for ~ 2 minutes to ensure proper mixing. Meanwhile, the Delrin or Lexan XAS sample holder surrounded by Kapton tape was purged with N_2 gas for ten minutes before the O_2-free LLL- or DLD-Ni^{II}-NCC complex sample was quickly transferred via a gastight syringe and needle to the sample holder and flash frozen in liquid nitrogen.

5.2.3. X-ray absorption data collection. XAS data were recorded by D. Leto and G. Wijeratne on beamline X3A at the National Synchrotron Light Source (NSLS), Brookhaven National Lab (storage ring conditions, 2.8 GeV, 100 - 300 mA). Ni K-edge X-ray absorption spectra were recorded on frozen solutions maintained at 25 K with a helium Displex closed-cycle cryostat over the energy range $8.1 - 9.1$ keV (Si(111) monochromater). The data were obtained as fluorescence excitation spectra using a solid-state 13-element germanium detector (Canberra). Contamination of higher harmonics radiation was minimized by the use of a harmonic rejection mirror. Background fluorescence signal was reduced by use of a 3 μm Co filter. A nickel foil spectrum was recorded for internal energy calibration and the first inflection point of the K-edge energy was assigned as 8331.6 eV. The spectra represent the average of 18 (O_2-free LLL-Ni^{II}-NCC), 20 (O_2-exposed LLL-Ni^{II}-NCC), 19 (O_2-free DLD-Ni^{II}-NCC), or 14 (O_2-exposed DLD-Ni^{II}-NCC) scans for 3 mM frozen solutions of the Ni-NCC samples.

5.2.4. XAS data analysis. XAS data reduction and averaging were treated entirely using the program EXAFSPAK.[13] Pre-edge background intensity was removed by fitting a Gaussian function to the pre-edge background and subtracting this function from the whole spectrum. The spectrum was then fit with a three-segment spline with fourth-order polynomial components to remove low-frequency background. EXAFS refinement was carried out on $k^3\chi(k)$ data, using

phase and amplitude functions obtained from *FEFF*, version 6.[14] The EXAFS fitting was also performed using EXAFSPAK. The *k*-space used for data analysis of the complexes was $k = 2 -$ 13.9 Å^{-1}, with resolution 0.133 Å. For each fit, the parameters *r* (average distance between Ni and scattering atom) and σ^2 (Debeye-Waller factor) were optimized, while *n*, the number of atoms in the shell, was kept fixed. *n* was varied by integer steps systematically. The goodness of fit (GOF) was evaluated by the parameter *F*, where $F = \Sigma (\chi_{calcd} - \chi_{expt})^2 / N$, and N is the number of data points. The threshold energy, E_0, in eV ($k = 0$ point) was kept at a common, variable value for every shell of a given fit.

5.3. Results and Analysis.

Because LLL-Ni^{II}-NCC undergoes metal-facilitated chiral inversion to DLD-Ni^{II}-NCC in the presence of O_2, authentic LLL-Ni^{II}-NCC can only be characterized in the absence of O_2. Therefore, in order to determine the structure of LLL-Ni^{II}-NCC, the XAS sample was prepared O_2-free. In addition, because DLD-Ni^{II}-NCC also undergoes some reactivity in the presence of O_2, a sample of O_2-free DLD-Ni^{II}-NCC was also prepared.

Table 5.1. XAS edge energies, pre-edge energies, and pre-edge intensities for Ni-NCC samples.

	O_2-free LLL-Ni^{II}-NCC	O_2-exposed LLL-Ni^{II}-NCC	O_2-free DLD-Ni^{II}-NCC	O_2-exposed DLD-Ni^{II}-NCC
edge (eV)	8341.4	8341.4	8341.5	8341.6
pre-edge (eV)	8333	8333.3	8333.1	8333.5
pre-edge intensity	0.18	0.25	0.23	0.27

In order to determine the structure of the O$_2$-exposed intermediates, XAS samples of ten-hour aged, O$_2$-exposed LLL-Ni^{II}-NCC and DLD-Ni^{II}-NCC were also prepared. The CD spectrum of DLD-Ni^{II}-NCC aged ten hours looks identical to that of aged LLL-Ni^{II}-NCC and therefore represents the final product(s) of the chiral inversion reaction in Ni-NCC. The full XAS spectra for all four samples are shown in Figure 5.2 and the edge and pre-edge energies are given in Table 5.1. As expected, all XAS spectra feature a relatively low absorption pre-edge intensity up until ~8330 eV, at the edge where a rapid increase in absorption intensity is observed. The EXAFS region has the distinct sharp decrease in intensity following the edge proceeded by the dampened oscillations. The overlaid spectra show that there are only subtle differences between the four samples (Figure 5.2).

The k^3-weighted and Fourier Transform (FT) of the EXAFS data for the four samples are
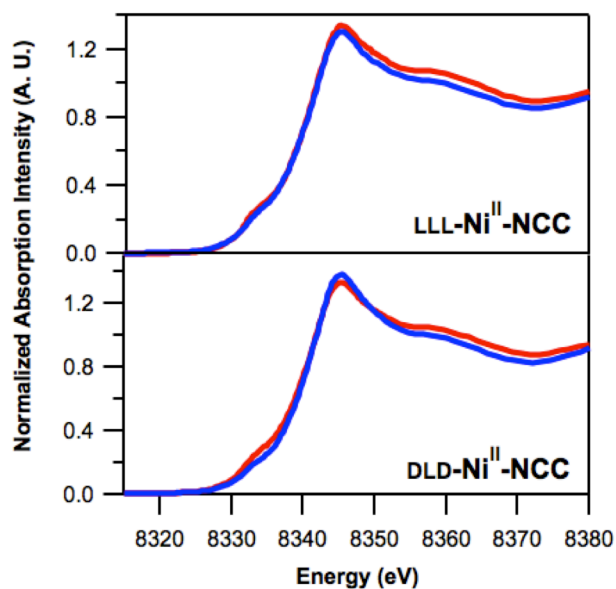
Figure 5.2. Ni K-edge XAS spectra of LLL-Ni^{II}-NCC (top) and DLD-Ni^{II}-NCC (bottom) prepared O$_2$-free (blue) and exposed to air (red). Spectra are normalized to their respective absorption edge.

presented in Figure 5.3. The FT spectra show two distinct peaks between $R' = 1.0$ and 2.1 Å that are consistent with two distinct distributions of radial distances from two shells of scatters. The raw FT and EXAFS data for these Ni^{II}-NCC samples look similar to those of dithionite reduced Ni-SOD,[15,16] and are very similar to one another, indicating that the nickel environment in each of the complexes must be similar.

Although the major peaks of the FT spectrum are at the same R' values, the broadening of the features between $1.0 - 2.1$ Å in the O_2-exposed intermediate of LLL-Ni^{II}-NCC (red, Figure 5.3, bottom) is indicative of a larger distribution of distances in the O_2-exposed sample. This is consistent with our previous proposal that this intermediate is composed of two or more species in solution.[11]

Table 5.2 shows the different fits for the four samples, O_2-free LLL-Ni^{II}-NCC, O_2-exposed LLL-Ni^{II}-NCC, O_2-free DLD-Ni^{II}-NCC, and O_2-exposed DLD-Ni^{II}-NCC. In addition, Figure 5.4
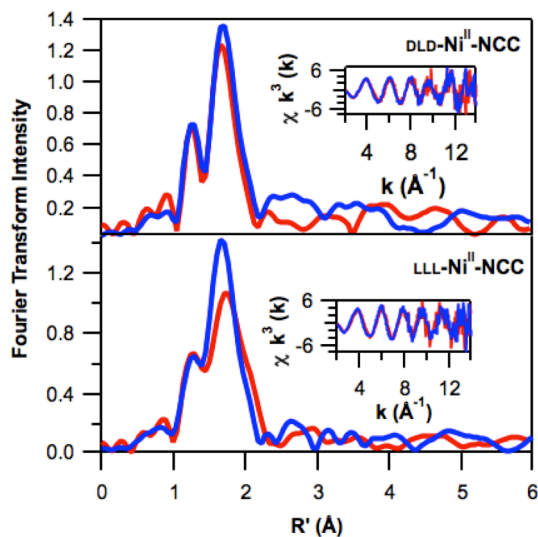
Figure 5.3. Fourier transform and k^3-weighted EXAFS data (insets) for LLL-Ni^{II}-NCC (bottom) and DLD-Ni^{II}-NCC (bottom) prepared O_2-free (blue) and O_2-exposed (red).

shows overlaid fits and raw data of the FT and EXAFS data for all four samples. For fitting the data, the number of scatterers was systematically varied, as well as the number of shells. Input parameters were based on the FEFF-generated bond distances that were determined from the density functional theory (DFT) optimized geometry of LLL-Ni^{II}-NCC. In general, a minimized GOF value, and reasonable σ^2 values are indicative of a good fit. The Debye-Waller factor, σ^2, is effectively a measure of disorder in the shell and therefore should not be negative, or very small or very large for shells that should be included in the fit of the data.

Table 5.2. EXAFS fits for O_2-free and ten-hour aged, O_2-exposed LLL-Ni^{II}-NCC and DLD-Ni^{II}-NCC. Data include the number of scatterers in the shell, n, radial distance, r (Å), the Debye-Waller factor, σ^2, and goodness of fit, GOF.

fit	Ni - N n	r (Å)	σ^2 x 10^3 (Å^2)	N - S n	r (Å)	σ^2 x 10^3 (Å^2)	Ni - - C n	r (Å)	σ^2 x 10^3 (Å^2)	GOF
				O_2-free LLL-Ni^{II}-NCC						
1a	4	2.37	-0.6							0.756
1b	**2**	**1.92**	**13.3**	**2**	**2.16**	**2.5**				**0.530**
1c	1	1.85	2.8	2	2.18	2.6				0.518
	1	1.99	-1.2							
1d	2	2.05	1.0	2	2.20	5.8	4	2.70	15.8	0.518
1e	1	1.88	5.0	2	2.19	3.3	4	2.60	17.4	0.512
	1	2.02	-0.9							
				O_2-exposed LLL-Ni^{II}-NCC						
2a	4	2.11	2.8							0.633
2b	**2**	**1.93**	**10.0**	**2**	**2.21**	**3.4**				**0.561**
2c	1	1.86	1.5	2	2.17	-0.4				0.553
	1	2.18	-5.5							
2d	2	1.86	9.8	2	2.18	4.8	4	2.37	4.1	0.554
2e	1	1.82	-2.0	2	2.20	1.5	4	2.72	17.9	0.532
	1	1.95	-3.8							
				O_2-free DLD-Ni^{II}-NCC						
3a	4	2.08	1.4							0.562
3b	**2**	**1.83**	**7.3**	**2**	**2.15**	**2.1**				**0.549**
3c	1	1.86	2.5	2	2.17	-0.5				0.551
	1	2.19	-4.6							
3d	2	2.07	-0.2	2	2.19	8.6	4	2.77	18.8	0.562
3e	1	1.81	0.5	2	2.17	2.8	4	2.51	24.0	0.538
	1	1.97	1.0							
				O_2-exposed DLD-Ni^{II}-NCC						
4a	4	2.07	2.3							0.649
4b	**2**	**1.81**	**7.7**	**2**	**2.14**	**2.9**				**0.635**
4c	1	1.82	0.7	2	2.17	4.3				0.621
	1	1.99	-0.9							
4d	2	2.05	0.0	2	2.20	11.1	4	2.83	12.0	0.632
4e	1	1.84	2.4	2	2.19	5.4	4	2.78	13.0	0.618
	1	2.02	-1.9							

For all four samples, fitting the data to one shell with four nitrogen atoms resulted in a large GOF value that decreased with addition of a shell with S atoms, indicating a better fit with inclusion of one shell of 2 N atoms and one shell of 2 S atoms (Table 5.2, fits a and b). Given that the nitrogen environment around the Ni in Ni-NCC is composed of one amine and one amide with distinct bond lengths, the N scatterers were split into two shells (Table 5.2, fits c and e) to fit two distinct Ni-N distances. However, this resulted in a negative σ^2 value for the longer Ni-N shell for almost all the fits. Because the σ^2 value is a measure of disorder and therefore should not be negative, these fits were excluded.

On the basis of the DFT computations, the difference in Ni-N bond distance (0.12 Å) is near the resolution of the EXAFS fits (0.133 Å). The σ^2 value for fit 1a in Table 5.2 is relatively large, indicative of a significant distribution of bond distances within that shell. Therefore, we attempted to split the nitrogen scatterers into two distinct shells (Table 5.2, fit 1c) to see if that improved the fit. Indeed, the GOF value decreased, but it also resulted in a negative σ^2 value. Therefore, the data were most reasonably fit with one shell of nitrogen scatterers. In addition, it has been shown that Ni-N distances have more disorder when the other ligands in the square planar nickel complex are S scatterers.[16,21]
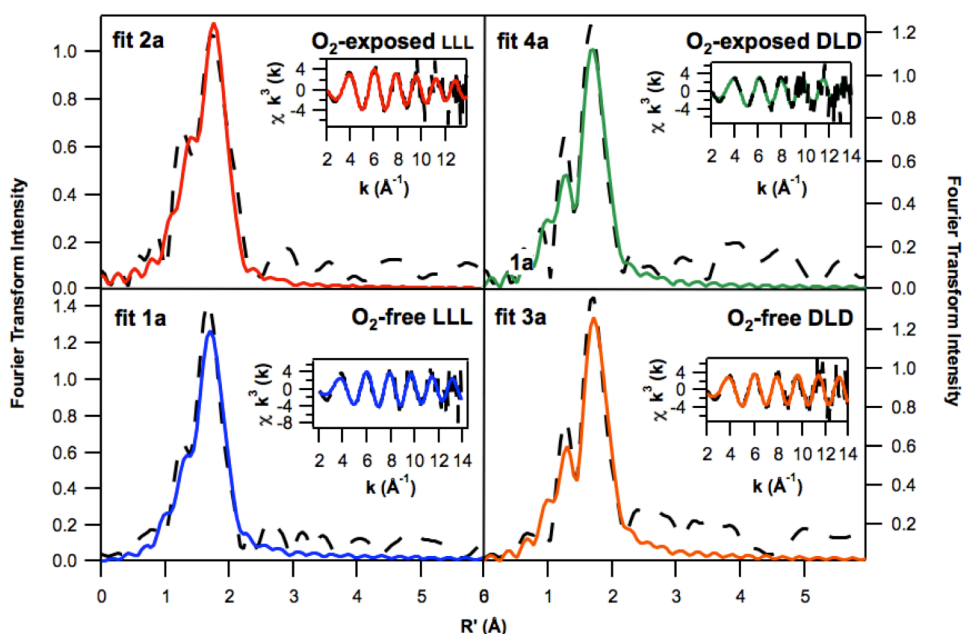
Figure 5.4. Comparing the fits for LLL-Ni^{II}-NCC (left) and DLD-Ni^{II}-NCC (right) prepared O_2-free (bottom) and aged ten hours in an atmosphere of air (top). FT of experimental data (black, dashed traces) and fits (colored, solid traces) are shown as well as the k^3-weighted EXAFS (insets) data (black, dashed traces) and fits (colored, solid traces). Fit numbers are included, as is represented in Table 5.2. All fits are with two shells of scatterers, one with two S atoms and the other with two N atoms.

We also evaluated if the GOF value could be reduced further by including a shell of carbon atoms. In our DFT-optimized structure of LLL-Ni^{II}-NCC there are three carbons less than 3.0 Å from the nickel, with the closest being 2.78 Å away.[1] Herbst, Maroney and coworkers found that including one or more carbon shells, with C scatterers from the two chelate rings that stabilize the Ni^{II} square plane, improved their fits.[16] As shown in Figure 5.4, inclusion of a C shell does not significantly improve the fits of the EXAFS data for either O_2-free or O_2-exposed LLL-Ni^{II}-NCC or DLD-Ni^{II}-NCC. This is also demonstrated by the lack of significant improvement in the GOF value upon addition of the C shell. Therefore, on the basis of the σ^2 values, radial interatomic distances, and GOF values, the EXAFS data for both O_2-free and O_2-exposed LLL-Ni^{II}-NCC are best fit by two shells of scatterers. It is important to note that in all

121

cases, fits were generated with lower GOF values, but had negative σ^2 values. Since negative disorder factors are not physically possible, these fits were not considered

5.4. Discussion.

For Ni, the pre-edge region of an XAS spectrum is particularly sensitive to the coordination number, oxidation state, geometry, and ligand field about the metal center.[21] Two transitions in this region, $1s \rightarrow 4p$ (~1 − 3 eV below the edge) and $1s \rightarrow 3d$ (~8 − 9 eV below the edge), are characteristic of the different ligand environments.[21] In six-coordinate octahedral Ni, the $1s \rightarrow 3d$ feature is present in low intensity, due to its parity forbidden nature. For five-coordinate Ni, both trigonal bipyramidal and square pyramidal geometries have the $1s \rightarrow 3d$ band but only in the square pyramidal environment is the $1s \rightarrow 4p$ transition observed.

The edge shape is especially distinctive for four-coordinate nickel complexes like Ni-NCC. Planar nickel has a weak $1s \rightarrow 3d$ transition 8 − 9 eV below the edge and a well-resolved $1s \rightarrow 4p$ transition 1 − 3 eV below the edge, whereas tetrahedral Ni only has the weak $1s \rightarrow 3d$ feature. In addition, the area under the $1s \rightarrow 3d$ band is empirically correlated to the coordination number about the metal center.[21] XAS data have been collected for Ni-SOD and various mutants, as well as small peptide maquettes designed from the sequence of the enzyme itself and the data is consistent with square planar Ni^{II}.[15,19-22] Therefore, the edge and pre-edge energies, as well as the average bond distances from EXAFS analysis are available and can be compared to those of LLL-Ni^{II}-NCC (Table 5.3).

The pre-edge features of the Ni^{II}-NCC complexes have a low intensity (0.18 − 0.27 AU) shoulder centered at ~8333 eV, ~ 8 eV lower in energy than the edge. The feature is lower in intensity than what would be expected for the $1s \rightarrow 4p$ transition, but higher than would be

predicted for the $1s\rightarrow3d$ transition. Comparison of our pre-edge spectra to those of the Ni-SOD maquettes showed that the maquettes have the two expected pre-edge transitions consistent with square planar Ni[II].

For square planar Ni[II] complexes with two or more sulfur ligands, the large Ni-S covalency can cause the pre-edge $1s\rightarrow4p$ transition to shift to lower energy and obscure the $1s\rightarrow3d$ transition.[21] However, sulfur coordination is present in other Ni[II] 2N:2S complexes, not just Ni-NCC, so the differences in the edge and pre-edge energies between Ni-NCC and the other metal complexes cannot be explained on the basis of the sulfur coordination. More likely, the distorted square planar structure of Ni[II]-NCC predicted from DFT computations[10] is responsible for modulating the pre-edge area and position significantly. Importantly, attempts to fit the Ni[II] center to a five-coordinate geometry did not result in improvement of the GOF value. Therefore, the Ni[II]-NCC complex is four coordinate.

Although analysis of the pre-edge shows that the electronic environments about the metal ions in the Ni-NCC complexes are different from those of the Ni-SOD enzyme and other small

Table 5.3. Bond distances obtained from DFT computations of LLL-Ni[II]-NCC and EXAFS fits of O_2-free and O_2-exposed LLL - and DLD-Ni[II]-NCC.

	LLL DFT ((Å)	O_2-free-LLL EXAFS (Å)	O_2-exposed-LLL EXAFS (Å)	O_2-free-DLD EXAFS (Å)	O_2-exposed-DLD EXAFS (Å)
Ni-N$_{amide}$	1.859	1.92	1.93	1.83	1.81
Ni-N$_{amine}$	1.982				
Ni-S$_{Cys3}$	2.201	2.16	2.21	2.15	2.14
Ni-S$_{Cys2}$	2.187				

molecule mimics, the structural data presented here (from EXAFS analysis) are consistent with the previously published DFT-predicted, experimentally-validated structure of LLL-Ni[II]-NCC (Table 5.3).[1,10] Indeed, the EXAFS data for both the O_2-free and O_2-exposed LLL-Ni[II]-NCC and

DLD-Ni^{II}-NCC are best fit to two shells of scatters, one containing two N atoms and the second with two S atoms. Together, these analyses confirm that the structure of LLL-Ni^{II}-NCC features square planar, Ni^{II} with a 2N:2S coordination environment. In addition, these fits are also consistent with those of wild-type Ni^{II}-SOD (Table 5.2) and Ni^{II}-SOD^{M1} and therefore show that they all have similar coordination.[15,17] In contrast, the Ni-SOD mutant where both Cys residues are converted to Ser residues, has significantly different bond distances due to the O coordination instead of S coordination (2.11 Å for the Ni-O versus 2.18 Å for Ni-S) .[17,22]

Table 5.4 below shows the edge energies, pre-edge energies, and EXAFS fits for dithionite reduced Ni-SOD and some of the peptide maquettes of the enzyme, as well as all of the data for the four samples analyzed in this work. The fit for Ni-SOD also has large disorder

Table 5.4. XAS comparison of four Ni^{II}-NCC samples to Ni^{II}-SOD and some of the peptide maquettes.

	Ni - N			N - S			Edge	Pre-edge	
	n	r (Å)	σ^2 x 10^3 (Å^2)	n	r (Å)	σ^2 x 10^3 (Å^2)	energy (eV)	energy (eV)	Reference
O$_2$-free LLL-Ni^{II}-NCC	2	1.92	13.3	2	2.16	2.5	8341.4	8333.0	this work
O$_2$-exposed LLL-Ni^{II}-NCC	2	1.93	10.0	2	2.21	3.4	8341.4	8333.3	this work
O$_2$-free DLD-Ni^{II}-NCC	2	1.83	7.3	2	2.15	2.1	8341.5	8333.1	this work
O$_2$-exposed DLD-Ni^{II}-NCC	2	1.81	7.7	2	2.14	2.9	8341.6	8333.5	this work
Ni^{II}-SOD	2	1.83	10.0	2	2.16	7.0	8340.5		14,20
Ni^{II}SOD^{M1}-Im-Me	2	1.91	2.6	2	2.18	2.2	8340.2	8332.7 8337.9	17
Ni^{II}SOD^{M1}-Im-Tos	2	1.87	2.9	2	2.17	3.4	8340.3	8332.4 8338	17
Ni^{II}SOD^{M1}-Im-DNP	2	1.89	2.8	2	2.18	2.7	8340.2	8332.5 8338.1	17

(σ^2) in the N shell, like the Ni-NCC samples. In addition, the DLD-Ni^{II}-NCC Ni-N bond distances are shorter than those in the LLL-Ni^{II}-NCC samples and the maquettes, but very close to the Ni-N bond distances in the Ni^{II} protein. The edge energy of the Ni^{II}-NCC complexes is shifted by ~1 eV in comparison to Ni-SOD and the maquettes. Although this is not a large difference, edge

shifts of ~2 eV are expected for conversion from Ni^{II} to Ni^{III}. Although previous MCD and EPR studies have shown a small amount of Ni^{III}-NCC, it does not accumulate and only represents < 1% of the bulk sample.[10,11,23]

In addition to confirming the 2N:2S structure of authentic LLL-Ni^{II}-NCC, EXAFS analysis was also performed on O$_2$-exposed LLL-Ni^{II}-NCC in order to provide structural insight for the intermediate. Although we have observed that the intermediate accumulates over the course of ten hours, and have rationalized it as a combination of two or more species in solution, the intermediate is evidenced by a nearly featureless CD spectrum below 21 500 cm^{-1}.[11] This featureless spectrum could be indicative of loss of metal in solution. However, XAS analysis confirms that the radial distances from Ni to the surrounding scatterers (N and S) within the O$_2$-exposed LLL-Ni^{II}-NCC sample are not significantly varied from those of the O$_2$-free LLL-Ni^{II}-NCC sample. Therefore, the ten-hour intermediate does not represent demetallated complex. An additional considered assignment for the ten-hour intermediate is a dimeric species. This is not supported by the EXAFS analysis, as the FT spectrum does not have an additional peak > 3 Å indicative of another nearby heavy atom scatterer within bonding/chemical interaction distance.

When compared to the data from the O$_2$-free sample, the O$_2$-exposed ten-hour aged data are also consistent with square planar, 2N:2S, Ni^{II}. However, the subtlety wider bands between 1.0 – 2.1 Å in the FT of the EXAFS data of the O$_2$-exposed sample (Figure 5.3, red solid trace) when compared to the O$_2$-free sample is indicative of a wider distribution of distances within the O$_2$-exposed sample.

5.5. Conclusions.

These data confirm that the structure of LLL-Ni^{II}-NCC is square planar Ni^{II} coordinated in

a 2N:2S environment, like the Ni(II) center of Ni^{II}-SOD. In addition, the ten-hour O$_2$-exposed LLL-Ni^{II}-NCC intermediate is not significantly different from that of O$_2$-free, authentic LLL-Ni^{II}-NCC. Furthermore, the structures of O$_2$-exposed and O$_2$-free DLD-Ni^{II}-NCC are not significantly different from O$_2$-free LLL-Ni^{II}-NCC either. The distribution of radial distances in the O$_2$-exposed samples is larger than those of the O$_2$-free samples. This could be rationalized by multiple species in solution, but is not definitive. Because the XAS data will be sensitive to all Ni in the samples, a sample with two or more species would be expected to have an increased σ^2 value in that shell, as well as a relatively broad distribution of distances on the FT spectrum, and both of these are true for ten-hour aged, O$_2$-exposed samples.

5.6. References.

(1)   Krause, M. E.; Glass, A. M.; Jackson, T. A.; Laurence, J. S. *Inorg. Chem.* **2011**, *50*, 2479.

(2)   Bal, W.; Chmurny, G. N.; Hilton, B. D.; Sadler, P. J.; Tucker, A. *J. Am. Chem. Soc.* **1996**, *118*, 4727.

(3)   Burrows, C. J.; Perez, R. J.; Muller, J. G.; Rokita, S. E. *Pure Appl. Chem.* **1998**, *70*, 275.

(4)   Krężel, A.; Kopera, E.; Protas, A. M.; Poznański, J.; Wysłouch-Cieszyńska, A.; Bal, W. *J. Am. Chem. Soc.* **2010**, *132*, 3355.

(5)   Liang, Q.; Eason, P. D.; Long, E. C. *J. Am. Chem. Soc.* **1995**, *117*, 9625.

(6)   Lioe, H.; Duan, M.; O'Hair, R. A. J. *Rapid Commun. Mass Spectrom.* **2007**, *21*, 2727.

(7)   Shullenberger, D. F.; Eason, P. D.; Long, E. C. *J. Am. Chem. Soc.* **1993**, *115*, 11038.

(8)   Splith, K.; Neundorf, I.; Hu, W. N.; N'Dongo, H. W. P.; Vasylyeva, V.; Merz, K.; Schatzschneider, U. *Dalton Trans.* **2010**, *39*, 2536.

(9)   Veerapandian, M.; Marimuthu, M.; Yun, K.-S.; Kim, S. *Thai J. Pharm. Sci.* **2009**, *33*, 1.

(10)   Krause, M. E.; Glass, A. M.; Jackson, T. A.; Laurence, J. S. *Inorg. Chem.* **2010**, *49*, 362.

(11)   Glass, A. M.; Krause, M. E.; Laurence, J. S.; Jackson, T. A. *J. Am. Chem. Soc.* **2012**, *In submission*.

(12)   Scott, R. A. In *Physical Methods in Bioinorganic Chemistry*; Lawrence Que, J., Ed.; University Science Book: Sausalito, CA, 2000, p 465

(13)   George, G. N. In *EXAFSPAK* Stanford Synchrotron Radiation Laboratory; Stanford, CA, 1990.

(14)   Rehr, J. J.; Mustre de Leon, J.; Zabinsky, S. I.; Albers, R. C. *J. Am. Chem. Soc.* **1991**, *113*, 5135.

(15)   Choudhury, S. B.; Lee, J. W.; Davidson, G.; Yim, Y. I.; Bose, K.; Sharma, M. L.; Kang, S. O.; Cabelli, D. E.; Maroney, M. J. *Biochemistry* **1999**, *38*, 3744.

(16)   Herbst, R. W.; Guce, A.; Bryngelson, P. A.; Higgins, K. A.; Ryan, K. C.; Cabelli, D. E.; Garman, S. C.; Maroney, M. J. *Biochemistry* **2009**, *48*, 3354.

(17)   Shearer, J.; Long, L. M. *Inorg. Chem.* **2006**, *45*, 2358.

(18)   Neupane, K. P.; Shearer, J. *Inorg. Chem.* **2006**, *45*, 10552.

(19)   Neupane, K. P.; Gearty, K.; Francis, A.; Shearer, J. *J. Am. Chem. Soc.* **2007**, *129*, 14605.

(20)   Shearer, J.; Neupane, K. P.; Callan, P. E. *Inorg. Chem.* **2009**, *48*, 10560.

(21)   Colpas, G. J.; Maroney, M. J.; Bagyinka, C.; Kumar, M.; Willis, W. S.; Suib, S. L.; Baidya, N.; Mascharak, P. K. *Inorg. Chem.* **1991**, *30*, 920.

(22)   Ryan, K. C.; Johnson, O. E.; Cabelli, D. E.; Brunold, T. C.; Maroney, M. J. *J. Biol. Inorg. Chem.* **2010**, *15*, 795.

(23)   Krause, M. E., University of Kansas, 2011.

Appendix

Table A.2.1. DFT-optimized Cartesian coordinates (Å) for Ni^{II}-ema

```
Ni    0.000000    0.000000    0.000000
S     0.230881   -2.294619   -0.033227
S    -2.303945    0.094357    0.033785
N     1.852287    0.094391    0.045763
N    -0.015321    1.854583   -0.045189
C     2.753002   -0.915882   -0.037894
C     2.138177   -2.296564   -0.253644
C    -2.419200    1.998279    0.253114
C    -1.077264    2.693831    0.037871
C     1.324066    2.441252   -0.288751
O    -1.023590    3.990491   -0.042610
C     2.358599    1.466098    0.289716
O     4.044207   -0.785484    0.042554
H     2.380325   -2.653812   -1.272844
H     2.584114   -3.003797    0.468200
H    -2.790788    2.219403    1.271968
H    -3.151206    2.401102   -0.469380
H     1.385940    3.452667    0.160550
H     1.486585    2.555792   -1.384320
H     3.364699    1.587802   -0.159288
H     2.463031    1.634910    1.385351
```

Table A.2.2. DFT-optimized Cartesian coordinates (Å) for Ni^{II}-N_2S_2

```
Ni    0.000000    0.000000    0.000000
N     0.081077    2.022850    0.038847
N    -2.060120   -0.190097    0.019223
S     0.081077   -2.192071    0.038847
S     2.177692   -0.065273    0.019223
C     0.279219    2.503394    1.433474
C     1.271030    2.406743   -0.802154
C    -2.472681   -1.484961    0.723480
C    -2.668797    0.960547    0.747062
C     2.538691    1.721981   -0.324780
C    -1.273959   -2.240590    1.281086
C    -2.461078    2.353942    0.126456
C    -1.121013    2.655118   -0.566021
C    -2.538418   -0.256534   -1.389694
H    -0.597884    2.243843    2.053620
H     1.161401    1.998848    1.867548
H     0.421039    3.610767    1.452635
H     1.368485    3.522448   -0.797651
H     1.037351    2.082946   -1.837085
H    -2.993896   -2.118357   -0.021510
H    -3.214293   -1.235295    1.514480
H    -2.244030    0.927069    1.771408
H    -3.768701    0.797921    0.854748
H     2.950945    2.218815    0.580664
H     3.313821    1.799033   -1.115727
H    -1.555806   -3.297146    1.486156
H    -0.928035   -1.802479    2.241697
H    -2.645541    3.088847    0.938957
H    -3.254171    2.554073   -0.625158
H    -1.146151    2.308642   -1.618438
H    -0.979053    3.763228   -0.603864
H    -2.061928   -1.132099   -1.869901
H    -3.649541   -0.358218   -1.434436
H    -2.238963    0.649439   -1.948311
```

Table A.2.3. DFT-optimized Cartesian coordinates (Å) for cisdistal-Ni^{II}-NCC

```
Ni  -2.564890   1.942068  -0.538255
N   -3.252117   1.093046  -2.184835
C   -2.338939   0.472220  -3.193288
C   -1.824174   1.561374  -4.151276
C   -3.031707  -0.634221  -4.002882
O   -1.980709   1.435006  -5.384746
C   -3.711769  -1.763977  -3.231134
N   -3.222055  -2.112995  -2.022608
O   -4.701132  -2.338760  -3.737363
N   -1.220423   2.682455  -3.673106
C   -0.705074   3.140339  -2.365361
C   -0.022969   2.037001  -1.492664
C   -1.609194   4.211150  -1.657395
O    1.241601   1.956435  -1.571935
S   -3.398783   3.904524  -1.161995
N   -0.799573   1.288361  -0.704253
C   -0.213384   0.532670   0.405037
C   -0.691066  -0.947563   0.407072
C   -0.496614   1.313102   1.695585
O   -0.847604  -1.489690  -0.740406
O   -0.808589  -1.536267   1.519160
S   -2.126507   2.249402   1.555735
H   -3.842328   0.351433  -1.782351
H   -3.887470   1.763200  -2.639001
H   -1.488636   0.063094  -2.623106
H   -2.289431  -1.101647  -4.669832
H   -3.799555  -0.202240  -4.657984
H   -3.670754  -2.902677  -1.560183
H   -2.330339  -1.770333  -1.604115
H   -0.981872   3.312456  -4.440940
H    0.172593   3.740844  -2.653918
H   -1.645446   5.078495  -2.337180
H   -1.067007   4.518589  -0.750988
H    0.881713   0.475364   0.256917
H    0.293056   2.055964   1.873654
H   -0.557701   0.632085   2.554235
```

Table A.2.4. DFT-optimized Cartesian coordinates (Å) for transmixed-Ni^{II}-NCC

```
Ni   -0.111170   -0.032735    0.121141
N     1.220353   -1.436271    0.044863
C     1.160367   -1.739936   -1.432806
C     0.469236   -0.549342   -2.180686
O     1.244278    0.260330   -2.736884
N    -0.859843   -0.631224   -2.727162
C    -2.170414   -0.351444   -2.047256
C    -2.681722   -1.452054   -1.130203
S    -1.671651   -1.623458    0.408911
C    -2.217443    1.054728   -1.386516
O    -3.049417    1.895354   -1.857333
N    -1.359425    1.277773   -0.395022
C    -1.220691    2.627472    0.160139
O    -1.442490    3.852817    2.220978
O    -2.646112    1.948350    2.011396
C     0.252939    3.018309    0.063698
S     1.299128    1.599910    0.652323
C    -1.810354    2.802018    1.599265
C     0.597789   -3.149961   -1.690906
C     0.858177   -3.669034   -3.104891
O     1.708886   -4.555054   -3.325738
N     0.094049   -3.126872   -4.078011
H     0.954190   -2.263695    0.589195
H     2.172913   -1.172852    0.313792
H     2.193511   -1.701782   -1.808535
H    -0.820224    0.028891   -3.512558
H    -2.876705   -0.286372   -2.889600
H    -3.720756   -1.215785   -0.857533
H    -2.683933   -2.410319   -1.671168
H    -1.820169    3.311735   -0.469970
H     0.524811    3.233385   -0.979918
H     0.462001    3.895447    0.688643
H    -0.475571   -3.166710   -1.454591
H     1.103843   -3.847560   -1.009200
H     0.261132   -3.379849   -5.049570
H    -0.516740   -2.330832   -3.853152
```

Table A.2.5. DFT-optimized Cartesian coordinates (Å) for bisamide-Ni(II)-NCC

```
Ni    0.070466   -0.166281    0.066511
N    -1.240385   -1.609487   -0.176494
C    -2.345191   -1.680942    0.600881
O    -2.361044   -2.143049    1.767030
C    -3.658371   -1.120262    0.015081
C    -3.643642    0.425605   -0.047578
N    -5.080831    0.879865   -0.225350
C    -2.920123    0.969010   -1.296221
O    -3.370352    0.579141   -2.399823
N    -1.894197    1.846766   -1.252437
C    -1.101175    2.636557   -0.266640
C    -1.354798    2.429896    1.218734
S    -0.943778    0.740482    1.856297
C     0.406577    2.516175   -0.649579
O     0.898067    3.461855   -1.336309
N     1.051410    1.437020   -0.205649
C     2.462123    1.226801   -0.590410
C     2.467064    0.376914   -1.857474
S     1.331523   -1.071156   -1.549048
C     3.364378    2.500049   -0.617945
O     4.077598    2.698454   -1.651739
O     3.409030    3.178925    0.454656
H    -1.513373   -1.385411   -1.141803
H    -3.847019   -1.515242   -0.995253
H    -4.484702   -1.431251    0.671015
H    -3.272162    0.838573    0.896509
H    -5.414753    0.608725   -1.164676
H    -5.182227    1.900481   -0.139164
H    -5.697346    0.449440    0.476900
H    -1.594364    2.064999   -2.207046
H    -1.351817    3.687595   -0.490270
H    -0.746860    3.187322    1.734489
H    -2.406751    2.652071    1.460925
H     2.893326    0.606012    0.215608
H     3.472304   -0.000063   -2.086890
H     2.104552    0.962121   -2.713865
```

Table A.3.1 DFT-optimized Cartesian coordinates (Å) for cis-proximal LLL-Ni[II]-NCC

```
Ni  -1.071070    1.684785    1.079184
N   -2.179774    1.933155    2.725115
C   -2.990978    0.647966    2.38772
C   -2.037451   -0.515832    2.052513
O   -2.063633   -1.596640    2.591751
N   -1.098842   -0.135398    1.119977
C    0.149269   -0.842057    0.907591
C    1.390272   -0.343057    1.713841
O    2.204926   -1.161718    2.071808
N    1.774590    1.005151    1.682324
C    1.076894    2.216978    2.233219
C    0.498081    2.096412    3.640728
O    0.449939    0.818566    4.040437
O    0.086766    3.015368    4.309981
C   -3.829847    1.024241    1.152721
S   -0.074850    1.101157   -0.780611
S   -1.014502    3.880635    0.956539
C    0.425986   -0.635129   -0.586331
C    0.806996    3.545177    1.405033
C   -4.869070    0.009481    0.709776
O   -5.953282    0.309451    0.271560
N   -4.487997   -1.300137    0.791900
H   -1.865190    1.918190    3.728448
H   -2.774948    2.784906    2.882671
H   -3.634953    0.394404    3.259220
H    0.027808   -1.932787    1.108098
H    2.742222    1.134363    1.980236
H    2.047959    2.613922    2.668127
H   -4.364065    1.981251    1.361379
H   -3.147977    1.232550    0.293698
H   -0.224762   -1.292288   -1.209136
H    1.488575   -0.821722   -0.858263
H    1.396047    3.495067    0.459351
H    1.151489    4.451258    1.961094
H   -5.141302   -2.004713    0.480008
H   -3.585558   -1.562900    1.165128
```

Table A.3.2. DFT-optimized Cartesian coordinates (Å) for cis-proximal LLL-Ni^{II}-NCC with water stabilizing the C-terminus

```
Ni   -0.423337    0.407845    0.280640
N    -1.914349    0.288081    1.581129
C    -2.560752   -1.054332    1.473697
C    -1.434316   -2.043427    1.118034
O    -1.523782   -3.275311    1.425368
N    -0.439805   -1.439803    0.477299
C     0.799568   -2.110728    0.142844
C     2.013951   -1.916729    1.095003
O     2.807410   -2.892626    1.101799
N     2.397445   -0.822910    1.832285
C     1.984440    0.498669    2.404085
C     0.849098    0.464104    3.465253
O     0.070617   -0.523256    3.536739
O     0.819809    1.486035    4.232397
C    -3.694112   -1.000318    0.431845
S     1.004990    0.197704   -1.361895
S     0.303486    2.413431    0.821151
C     1.185975   -1.661720   -1.273605
C     1.931077    1.731686    1.446249
C    -4.667398   -2.177434    0.358168
O    -5.794327   -2.012162   -0.158369
N    -4.259878   -3.360532    0.858957
H    -1.422672    0.323051    2.488410
H    -2.606075    1.043871    1.560184
H    -2.982088   -1.346631    2.449111
H     0.647652   -3.202507    0.156141
H     3.291282   -1.088868    2.249766
H     2.873601    0.720444    3.016561
H    -4.317362   -0.114415    0.629297
H    -3.265451   -0.860322   -0.575397
H     0.501370   -2.133602   -1.992546
H     2.217116   -1.942499   -1.525841
H     2.547826    1.496170    0.570739
H     2.387376    2.571550    1.989321
H    -4.881627   -4.161912    0.768419
H    -3.280836   -3.501485    1.180988
O     2.651202    3.400844    4.612356
H     1.993807    2.658075    4.423081
H     2.948979    3.233568    5.524274
```

Table A.3.3. DFT-optimized Cartesian coordinates (Å) for cis-proximal DLL-Ni$^{\text{II}}$-NCC

```
Ni   −1.146165    1.794115    0.752805
N    −2.383294    1.970494    2.278679
C    −2.846238    0.626027    2.731749
C    −1.794176   −0.424881    2.312576
O    −1.766871   −1.569723    2.839120
N    −1.003404    0.038500    1.338253
C     0.145191   −0.698377    0.847029
C     1.552617   −0.286201    1.356991
O     2.435575   −1.169871    1.211939
N     1.966166    0.939902    1.798900
C     1.421099    2.170855    2.434080
C     0.433998    1.916624    3.616943
O     0.451447    0.778559    4.156673
O    −0.236033    2.929354    4.005569
S    −0.052072    1.276250   −1.064568
S    −0.470437    3.886342    0.752935
C     0.148286   −0.546702   −0.682243
C     1.194622    3.390752    1.481915
C    −3.132341    0.562624    4.231551
C    −4.379733    1.338002    4.632054
N    −4.308826    1.997127    5.812628
O    −5.409275    1.349976    3.928846
H    −1.812101    2.440028    3.008457
H    −3.176220    2.580428    2.059997
H    −3.777309    0.399048    2.187789
H     0.059131   −1.762949    1.121647
H     2.974821    0.872651    1.945022
H     2.310149    2.512900    2.998390
H    −0.700443   −1.107890   −1.098358
H     1.079881   −0.917167   −1.129221
H     1.881559    3.253247    0.636340
H     1.512394    4.285288    2.037095
H    −2.247140    0.898182    4.793267
H    −3.301342   −0.495525    4.494289
H    −5.126316    2.486524    6.169897
H    −3.470298    1.978229    6.385196
```

Table A.3.4. DFT-optimized Cartesian coordinates (Å) for cis-proximal LDL-Ni^{II}-NCC

```
Ni  −1.173719    1.843631    1.300811
N   −2.862447    1.758861    0.281385
C   −3.410774    0.366851    0.344095
C   −2.192060   −0.589816    0.418242
O   −2.240179   −1.774640   −0.034995
N   −1.152755    0.000464    1.007051
C    0.185548   −0.595834    1.010093
C    0.895562   −0.312202   −0.349351
O    1.249203   −1.324675   −0.996167
N    0.950134    0.907236   −1.000054
C    1.431402    2.281612   −0.652198
C    2.616072    2.337445    0.364376
O    3.210288    1.251130    0.630508
O    2.981883    3.507180    0.691440
C   −4.389434    0.088952   −0.819168
S   −0.639549    3.932627    0.867928
C    0.375780    3.423005   −0.630440
C   −5.442180   −0.992154   −0.555201
O   −6.663132   −0.743616   −0.661863
N   −4.956219   −2.201831   −0.219778
C    0.915042   −0.156228    2.277481
S    0.524815    1.635631    2.627835
H   −3.558804    2.438239    0.603980
H   −2.653089    2.008853   −0.692635
H   −3.951220    0.293271    1.301168
H    0.103027   −1.695256    1.004292
H    1.267634    0.683908   −1.945839
H    1.969748    2.545420   −1.583347
H   −4.945415    1.010195   −1.036536
H   −3.820519   −0.182541   −1.723665
H   −0.330711    3.212592   −1.446413
H    0.921012    4.339929   −0.897334
H   −5.597117   −2.963912   −0.010142
H   −3.925998   −2.308308   −0.134858
H    2.002084   −0.242629    2.153727
H    0.586504   −0.784253    3.118765
```

Table A.3.5. DFT-optimized Cartesian coordinates (Å) for cis-proximal LLD-Ni^{II}-NCC

```
Ni    1.238496    2.940606    0.214662
N    -0.483277    2.133878   -0.309547
C    -0.444357    0.680086    0.037081
C     0.972636    0.222217   -0.388590
C    -1.561516   -0.126419   -0.625528
O     1.183063   -0.850142   -0.997758
C    -1.689755   -1.531401   -0.048182
N    -1.989002   -2.509080   -0.935735
O    -1.592996   -1.753835    1.174425
N     1.864928    1.151755    0.001681
C     3.061330    1.596916   -0.731699
C     3.429552    0.966959   -2.064416
C     4.128189    1.958396    0.310455
O     4.120304   -0.059754   -2.221693
S     3.260019    3.333109    1.263535
N     3.035033    1.723513   -3.140510
C     2.232044    2.968451   -3.382528
C     0.717878    2.706722   -3.677501
C     2.401376    4.227206   -2.453385
O     0.131088    1.763411   -3.068644
O     0.204288    3.497175   -4.524417
S     1.109440    4.734096   -1.157017
H    -1.310199    2.597253    0.079929
H    -0.533665    0.594170    1.130766
H    -1.412753   -0.157170   -1.713477
H    -2.525108    0.376084   -0.432847
H    -2.089167   -3.468402   -0.611743
H    -1.979315   -2.339230   -1.936714
H     2.776675    2.597141   -1.08534
H     5.038461    2.361120   -0.152878
H     4.383931    1.114135    0.96390
H     3.317084    1.289668   -4.021284
H     2.646367    3.307596   -4.343062
H     2.380532    5.086982   -3.136198
H     3.394216    4.218943   -1.981036
H    -0.496317    2.220943   -1.344971
```

Table A.3.6. DFT-optimized Cartesian coordinates (Å) for cis-proximal DLL-Ni^{II}-NCC

```
Ni   −1.146165    1.794115    0.752805
N    −2.383294    1.970494    2.278679
C    −2.846238    0.626027    2.731749
C    −1.794176   −0.424881    2.312576
O    −1.766871   −1.569723    2.839120
N    −1.003404    0.038500    1.338253
C     0.145191   −0.698377    0.847029
C     1.552617   −0.286201    1.356991
O     2.435575   −1.169871    1.211939
N     1.966166    0.939902    1.798900
C     1.421099    2.170855    2.434080
C     0.433998    1.916624    3.616943
O     0.451447    0.778559    4.156673
O    −0.236033    2.929354    4.005569
S    −0.052072    1.276250   −1.064568
S    −0.470437    3.886342    0.752935
C     0.148286   −0.546702   −0.682243
C     1.194622    3.390752    1.481915
C    −3.132341    0.562624    4.231551
C    −4.379733    1.338002    4.632054
N    −4.308826    1.997127    5.812628
O    −5.409275    1.349976    3.928846
H    −1.812101    2.440028    3.008457
H    −3.176220    2.580428    2.059997
H    −3.777309    0.399048    2.187789
H     0.059131   −1.762949    1.121647
H     2.974821    0.872651    1.945022
H     2.310149    2.512900    2.998390
H    −0.700443   −1.107890   −1.098358
H     1.079881   −0.917167   −1.129221
H     1.881559    3.253247    0.636340
H     1.512394    4.285288    2.037095
H    −2.247140    0.898182    4.793267
H    −3.301342   −0.495525    4.494289
H    −5.126316    2.486524    6.169897
H    −3.470298    1.978229    6.385196
```

Table A.3.7. DFT-optimized Cartesian coordinates (Å) for cis-proximal DLL-Ni^{II}-NCC with water stabilizing the C-terminus

Ni	−0.134732	0.130611	0.259649
N	−1.345939	0.207381	1.819140
C	−1.841982	−1.163429	2.143638
C	−0.799979	−2.191315	1.649651
O	−0.791313	−3.374747	2.081778
N	0.001689	−1.660608	0.720397
C	1.130117	−2.375212	0.155525
C	2.555486	−2.004722	0.646884
O	3.428184	−2.878213	0.414872
N	2.989887	−0.807063	1.146901
C	2.465919	0.355699	1.910275
C	1.522960	−0.031802	3.093027
O	1.550774	−1.220120	3.492859
O	0.869983	0.921819	3.649348
S	0.898664	−0.283418	−1.620144
S	0.581176	2.209572	0.345478
C	1.091595	−2.128247	−1.361130
C	2.230364	1.663726	1.085289
C	−2.169767	−1.356068	3.622804
C	−3.451085	−0.649994	4.047496
N	−3.445285	−0.119538	5.292757
O	−4.450166	−0.585372	3.304740
H	−0.769039	0.584235	2.593489
H	−2.124438	0.854686	1.665142
H	−2.763243	−1.322453	1.560429
H	1.040066	−3.453501	0.367647
H	4.003229	−0.882470	1.250704
H	3.369064	0.646791	2.481775
H	0.225172	−2.654145	−1.786317
H	2.006418	−2.475995	−1.857951
H	2.945982	1.628627	0.253376
H	2.512187	2.501292	1.739329
H	−1.313912	−1.049854	4.243691
H	−2.317957	−2.436757	3.789942
H	−4.289099	0.311658	5.663523
H	−2.631561	−0.182853	5.897037
O	0.174578	3.520587	3.218128
H	0.494856	2.610171	3.472287
H	0.100369	3.369832	2.237407

Table A.3.8. DFT-optimized Cartesian coordinates (Å) for cis-proximal DLD-Ni^II-NCC

```
Ni    0.160784    0.005282    0.162667
N    -1.640548   -0.815253   -0.042588
C    -2.436597   -0.050806   -1.059589
C    -3.477688   -0.904322   -1.773842
C    -4.654243   -1.289210   -0.880365
O    -5.014726   -0.586251    0.080841
N    -5.291353   -2.433150   -1.222073
C    -1.455566    0.621296   -2.056900
O    -1.805184    0.922049   -3.227679
N    -0.264902    0.828039   -1.481592
C     0.943213    1.232955   -2.199736
C     1.651761    2.245272   -1.294454
S     1.823659    1.422734    0.386480
C     1.944557    0.030856   -2.393293
O     3.091338    0.244410   -2.813054
N     1.464767   -1.194574   -2.040619
C     2.244671   -2.276145   -1.409396
C     3.456843   -2.733761   -2.294214
O     4.581095   -2.864588   -1.726735
O     3.185658   -3.010919   -3.499000
C     2.611173   -1.937364    0.050660
S     1.176483   -1.671487    1.242387
H    -2.137657   -0.831800    0.853802
H    -1.544629   -1.797688   -0.324965
H    -2.956460    0.750276   -0.512244
H    -3.014050   -1.800927   -2.214559
H    -3.873057   -0.314779   -2.617813
H    -6.125659   -2.718795   -0.715474
H    -4.997677   -2.994766   -2.015345
H     0.706461    1.662042   -3.188872
H     2.651021    2.489000   -1.674849
H     1.050706    3.161124   -1.214415
H     0.533964   -1.116391   -1.613511
H     1.563550   -3.143638   -1.395385
H     3.186136   -2.778021    0.461454
H     3.233658   -1.034660    0.078690
```

Table A.3.9. DFT-optimized Cartesian coordinates (Å) for cis-proximal DLD-Ni^{II}-NCC with water stabilizing the C-terminus

```
Ni   -0.034794   -0.154558   -0.335529
N    -1.881965   -0.898943   -0.379132
C    -2.730736   -0.127358   -1.346721
C    -3.834171   -0.968831   -1.978447
C    -4.957975   -1.310697   -1.004588
O    -5.293080   -0.541112   -0.084358
N    -5.580638   -2.491277   -1.224634
C    -1.811089    0.519199   -2.413804
O    -2.244198    0.838908   -3.551779
N    -0.570232    0.688081   -1.938440
C     0.581180    1.062025   -2.760046
C     1.401278    2.042609   -1.917233
S     1.688727    1.202343   -0.260198
C     1.521440   -0.165254   -3.053627
O     2.629205    0.014288   -3.580997
N     1.043420   -1.381259   -2.662219
C     1.853346   -2.484750   -2.112212
C     2.995049   -2.925634   -3.085839
O     4.169136   -3.013348   -2.639651
O     2.611978   -3.244111   -4.263061
C     2.342462   -2.181669   -0.680197
S     1.014808   -1.886172    0.622753
H    -2.297331   -0.872169    0.557957
H    -1.848101   -1.891740   -0.639143
H    -3.199697    0.688546   -0.774957
H    -3.420019   -1.881574   -2.435333
H    -4.273409   -0.380577   -2.801779
H    -6.383495   -2.753570   -0.657226
H    -5.306735   -3.107316   -1.984459
H     0.268375    1.507348   -3.720580
H     2.373410    2.253074   -2.379035
H     0.843282    2.978417   -1.777342
H     0.162135   -1.279164   -2.144206
H     1.168426   -3.348135   -2.068098
H     2.916634   -3.047368   -0.322856
H     2.998132   -1.302669   -0.688099
O     4.616628   -3.936762   -5.866484
H     3.885246   -3.661924   -5.212817
H     5.430428   -3.875289   -5.335049
```

Table A.3.10. TD-DFT predicted *d-d* transitions in LLL-Ni^{II}-NCC and DLD-Ni^{II}-NCC

Band	State	Energy (cm^{-1})	Transition	%	Donor MO	Acceptor MO
			LLL-Ni^{II}-NCC			
1	1	14 500	*d-d*	77.5	z^2	x^2-y^2
	2	15 600	*d-d*	77.2	yz	x^2-y^2
	3	17 000	*d-d*	85.9	xz	x^2-y^2
2	4	19 300	*d-d*	37.8	xy	x^2-y^2
			DLD-Ni^{II}-NCC			
1	1	12 400	*d-d*	81.2	z^2	x^2-y^2
2	2	14 300	*d-d*	79.4	yz	x^2-y^2
	3	15 600	*d-d*	82.3	xz	x^2-y^2
3	4	18 500	*d-d*	26.7	xy	x^2-y^2